POLYTECHNIQUE MONTRÉAL
affiliée à l'Université de Montréal

Advances in Few-Mode Optical Coherence Tomography

RAPHAËL MALTAIS-TARIANT
Département de génie physique

Thèse présentée en vue de l'obtention du diplôme de *Philosophiæ Doctor*
Génie physique

April 2026

© Raphaël Maltais-Tariant, 2026.

POLYTECHNIQUE MONTRÉAL
affiliée à l'Université de Montréal

Cette thèse intitulée :

Advances in Few-Mode Optical Coherence Tomography

présentée par **Raphaël MALTAIS-TARIANT**
en vue de l'obtention du diplôme de *Philosophiæ Doctor*
a été dûment acceptée par le jury d'examen constitué de :

Jean PROVOST, président
Caroline BOUDOUX, membre et directrice de recherche
Mathieu DEHAES, membre et codirecteur de recherche
Frédéric LEBLOND, membre
Parsin HAJI REZA, membre externe

DEDICATION

To all my friends and grandmother,
Thank you for your support throughout these years.

À tous mes amis et grand-maman,
Merci pour votre soutien au cours de ces années.

ACKNOWLEDGEMENTS

La fin du doctorat est un grand chapitre de ma vie qui se termine. Ce n'est pas un chapitre que j'ai écrit seul. J'aimerais remercier tous ceux qui m'ont accompagné lors de cette aventure.

J'ai énormément appris et grandi au cours de ces dernières années et je suis fier de la personne que je suis devenue.

Ceci ne serait pas arrivé sans les encouragements, les conseils et le soutien des gens qui m'entourent, et je vous en serai toujours reconnaissant.

RÉSUMÉ

La tomographie par cohérence optique (TCO) est une modalité d'imagerie médicale ayant connu un essor considérable au cours des dernières décennies. Elle se distingue par sa capacité d'imagerie non invasive à haute résolution, bien que sa profondeur de champ demeure limitée. Elle est particulièrement adaptée à l'imagerie des tissus épithéliaux et de la rétine, et constitue un outil incontournable pour l'étude de l'angiographie rétinienne. Sa large adoption a engendré de nombreuses innovations technologiques et applicatives. Toutefois, la TCO fait encore face à plusieurs défis.

La TCO ne collecte généralement qu'une fraction de la lumière rétroréfléchie par l'échantillon observé. La nécessité d'utiliser des fibres optiques monomodes implique une perte des modes d'ordre supérieur de la lumière. Cela entraîne non seulement une perte de signal, mais surtout une perte d'informations potentiellement pertinentes. Même les systèmes TCO n'utilisant pas de fibres monomodes présentent cette limitation sous d'autres formes. De plus, bien qu'elle soit un outil essentiel pour l'angiographie, la TCO éprouve encore des difficultés à quantifier la vitesse du flux sanguin. Cette limite restreint ses capacités diagnostiques et sa contribution à l'étude des pathologies. De nombreuses innovations ont été proposées pour pallier ces lacunes, mais le défi demeure.

Les lanternes photoniques sont des composants optiques relativement récents qui offrent une solution potentielle à ces problématiques. Initialement développées pour l'astronomie, elles agissent comme des démultiplexeurs à fibre optique, répartissant les modes d'ordre supérieur de la lumière en plusieurs canaux. Plus récemment, les lanternes photoniques à mode-selectif (LPMS), une forme spécialisée de lanterne photonique, ont permis le démultiplexage sélectif de modes. Cette innovation a permis l'émergence d'un nouveau type de TCO exploitant les modes d'ordre supérieur—une partie de la lumière auparavant perdue—désigné sous le nom de tomographie par cohérence optique à quelques modes (TCO-QM).

Cette thèse présente les innovations développées lors de l'exploration des applications potentielles de la TCO-QM, dont certaines ne requièrent pas l'utilisation d'une LPMS.

La combinaison des signaux issus de plusieurs modes de la TCO-QM permet d'augmenter le rapport signal sur bruit et de réduire le bruit de tavelure, avec un impact limité sur la résolution. Cette approche peut également être couplée à d'autres techniques de réduction du speckle pour améliorer encore la clarté des images.

Il en résulte des images plus nettes avec des détails fins plus aisément observables, facilitant

le diagnostic à l'aide de la TCO.

La contribution la plus significative de cette thèse réside probablement dans le développement d'une nouvelle méthode de mesure du flux sanguin. Basée sur le rapport entre la corrélation croisée et l'autocorrélation des différents canaux de la TCO-QM, cette méthode a démontré une précision de trois à cinq fois supérieure à celle des approches existantes. La méthode permet de mesurer des vitesses beaucoup plus faibles, rendant possible la distinction entre des flux lents et des flux statiques. Elle ne nécessite aucune connaissance préalable des propriétés de l'échantillon, telles que le coefficient de diffusion. Seules deux mesures consécutives sont requises, ce qui confère à la méthode une grande flexibilité d'utilisation. Enfin, elle s'est révélée nettement plus robuste face aux différentes sources de biais.

Cette technique ne se serait pas limitée au TCO-QM. Des résultats préliminaires ont été démontrés avec un TCO standard. Le même principe pourrait également être étendu à d'autres appareils d'imagerie.

Cette avancée répond à un besoin réel en TCO : mesurer avec précision le flux sanguin dans la rétine. Dans cet organe, la majorité des vaisseaux sanguins sont orientés transversalement à l'axe d'imagerie. Offrir une mesure fiable du flux ouvre la voie à une étude plus précise des pathologies associées au développement vasculaire rétinien.

ABSTRACT

Optical coherence tomography (OCT) is a medical imaging modality that has gained significant prominence in recent decades. Renowned for its high-resolution, non-invasive imaging capabilities, OCT is particularly well-suited for visualizing epithelial tissues and the retina, and is an indispensable tool for ophthalmic angiography. Its widespread adoption has driven numerous technological and application-based innovations. Nevertheless, OCT continues to face several challenges.

OCT is generally limited to collecting only a fraction of the light retroreflected from the sample. The reliance on single-mode optical fibers (SMF) in system design results in the loss of higher-order modes, leading not only to reduced signal strength but, more critically, to the loss of valuable information. Even OCT systems that do not employ SMF encounter analogous limitations. Additionally, although OCT is foundational for angiography, it continues to face significant challenges in quantifying blood flow velocity. This limitation constrains both its diagnostic utility and its ability to advance the study of various diseases. Numerous innovations have sought to address these shortcomings, yet a comprehensive solution remains elusive.

Photonic lanterns (PL) are a relatively recent innovation in optical components that offer potential solutions to these challenges. Initially developed for astronomical applications, PL functions as fiber-based demultiplexers, separating higher-order modes of light into multiple fiber channels. More recently, mode-selective photonic lanterns (MSPL), a type of PL, have enabled selective mode demultiplexing, paving the way for OCT imaging in higher-order modes using previously discarded light—a technique known as few-mode optical coherence tomography (FM-OCT).

This thesis presents innovations developed through the exploration of potential applications of fiber-based FM-OCT. Notably, some of these applications do not require the use of an MSPL.

Combining signals from multiple modes in FM-OCT results in increased signal-to-noise ratio (SNR) and reduced speckle noise, with only a minimal compromise in resolution. Specifically, speckle noise is diminished while SNR improves proportionally to the square root of the number of FM-OCT channels. This approach can also be integrated with other speckle-reduction techniques to further enhance image clarity.

The resulting images exhibit reduced speckle, making fine structural details more discernible

and thereby facilitating improved diagnostic capabilities relative to conventional techniques.

The most significant contribution of this thesis is the development of an innovative method for measuring flow velocity. This technique, based on the ratio of cross-correlation to autocorrelation between FM-OCT channels, demonstrated a three- to five-fold increase in accuracy relative to existing correlation-based methods. The system is capable of measuring substantially lower flow velocities, enabling the distinction between slow and static flows. Moreover, it requires no prior knowledge of sample properties and only two consecutive measurements, unlike fitting-based approaches, thereby offering greater flexibility. The method has also proven to be more robust against sources of bias in flow measurements.

Importantly, the technique may not be limited to FM-OCT, as preliminary results have been demonstrated with standard OCT systems. The underlying principle could potentially be extended to other imaging modalities.

This advancement provides a much-needed solution for accurately measuring lateral flow velocity in OCT. While OCT excels at imaging the retina and its vasculature, most retinal blood vessels are oriented laterally relative to the imaging axis, and accurate measurement of their flow has remained a challenge. Reliable assessment of lateral blood flow introduces new diagnostic capabilities for OCT in retinal imaging.

TABLE OF CONTENTS

DEDICATION iii

ACKNOWLEDGEMENTS iv

RÉSUMÉ v

ABSTRACT vii

TABLE OF CONTENTS ix

LIST OF TABLES xii

LIST OF FIGURES xiii

LIST OF SYMBOLS AND ACRONYMS xix

LIST OF APPENDICES xx

CHAPTER 1 INTRODUCTION 1
- 1.1 Context 1
- 1.2 Project statement 3
- 1.3 Project objectives 3
- 1.4 Thesis outline 5

CHAPTER 2 LITERATURE REVIEW 7
- 2.1 Optical coherence tomography 7
  - 2.1.1 Speckle noise 8
  - 2.1.2 OCT signal 9
  - 2.1.3 Resolution 9
  - 2.1.4 Sample scanning 10
  - 2.1.5 Signal processing 11
- 2.2 Optical fibers and higher-order modes 12
- 2.3 Mode-selective photonic lantern 13
- 2.4 Few-mode optical coherence tomography 14
- 2.5 Modeling light 15
- 2.6 Flow measurement 17

CHAPTER 3 ARTICLE 1 - MCOCT: AN EXPERIMENTALLY AND NUMERICALLY VALIDATED, OPEN-SOURCE MONTE CARLO SIMULATOR FOR OPTICAL COHERENCE TOMOGRAPHY . . . 20
3.1 Introduction . . . 21
3.2 Material and methods . . . 23
3.2.1 Monte Carlo photon propagation . . . 23
3.2.2 OCT signal simulation . . . 23
3.2.3 OCT signal reconstruction . . . 27
3.2.4 Tissue-mimicking optical phantoms . . . 29
3.2.5 MCOCT simulations for comparison with MCX simulations . . . 31
3.2.6 MCOCT simulations for comparison with OCT imaging in phantoms 32
3.3 Results . . . 32
3.4 Discussion . . . 33
3.5 Conclusion . . . 39

CHAPTER 4 ARTICLE 2 - SPECKLE CONTRAST REDUCTION THROUGH THE USE OF A MODALLY-SPECIFIC PHOTONIC LANTERN FOR OPTICAL COHERENCE TOMOGRAPHY . . . 42
4.1 Introduction . . . 43
4.2 Material and Methods . . . 43
4.2.1 Instrumentation . . . 43
4.2.2 Imaging metrics . . . 44
4.2.3 *In vitro* and *in vivo* imaging . . . 46
4.3 Results and Discussion . . . 47
4.4 Conclusion . . . 52

CHAPTER 5 PRIOR WORKS ON FEW-MODE OPTICAL COHERENCE TOMOGRAPHY FLOW MEASUREMENTS . . . 54
5.1 Prior methods . . . 54
5.2 The polarization issue . . . 56
5.3 Measurements on blood . . . 58

CHAPTER 6 ARTICLE 3 - ACCURATE FLOW SPEED MEASUREMENT THROUGH CORRELATION RATIOS USING A MODE-SELECTIVE PHOTONIC LANTERN IN OPTICAL COHERENCE TOMOGRAPHY . . . 60
6.1 Introduction . . . 61
6.2 Theory . . . 62

6.2.1 Coherent spread function in optical coherence tomography 62
6.2.2 Signal correlation 64
6.3 Material and methods 67
6.3.1 FM-OCT system and experiments 67
6.3.2 Calibration 69
6.3.3 M-mode scans 69
6.3.4 B-scan 71
6.4 Results 71
6.5 Discussion 78
6.6 Conclusion 83

CHAPTER 7 GENERAL DISCUSSION 85
7.1 Flow measurement alternatives 85
7.1.1 Using second-order correlation 85
7.1.2 Flow direction 86
7.1.3 Correlation ratio without photonic lantern 88
7.2 Inconclusive avenues 95
7.2.1 Super-resolution 95
7.2.2 Axial gradient velocity simulations 96
7.2.3 Scatterer size contrast 96
7.3 Thesis-specific objectives 97
7.3.1 Building the system 97
7.3.2 Modeling multi-modal signals 97
7.3.3 Improving signal quality 99
7.3.4 Flow measurement 100

CHAPTER 8 CONCLUSION 102
8.1 Summary of work and limitations 102
8.2 Outlook 104

REFERENCES 107

APPENDICES 124

LIST OF TABLES

Table 3.1 Quantities of the scattering (titanium dioxide) and absorbing (nigrosine) agents of the phantoms developed with polydimethylsiloxane (PDMS) matrices. 30

Table 3.2 Optical properties of the phantoms characterized by spectrophotometry: μ_a, absorption coefficient; μ'_s, reduced scattering coefficient; n, refractive index; g anisotropy coefficient. 31

Table 3.3 Position of focus z_f [mm] below the phantom surface for each focal lens f. 32

Table 3.4 Computation time and quantity of launched and detected photons for MCOCT simulations presented in Fig. 3.6 and Fig. 3.7. 33

Table 3.5 Variables used to describe Fig. 3.1 and Fig. 3.3 41

Table 4.1 Measurement of $\mathrm{SNR}_{\mathrm{max}}$, retro-reflection power and the full width at half maximum (FWHM) of an OCT A-line of a mirror in intensity in linear scale for the single-mode fiber (SMF) and modally-specific photonic lantern (MSPL) optical configurations. 48

Table 6.1 Root-mean-square error (RMSE) of flow speed measurements (v_{tot} compared to previous published techniques (v_{sp} and v_{fit}) for the flow speeds used in Fig. 6.5. 73

Table 6.2 Root-mean-square error (RMSE) of flow measurements with a tilt angle $\phi = 10°$ (v_{tot}) compared to previously published techniques (v_{sp} and v_{fit}) for the flow speeds used in Fig. 6.6. 75

LIST OF FIGURES

Figure 2.1 Schematic of a fiber-based optical coherence tomography system employing a 90%/10% coupler to split the light between the reference and sample arms, circulators (C1 and C2) to redirect the returning light toward the detector, a polarization controller (PC) to optimize polarization orientation for interference, a 50%/50% coupler to combine signals from both arms, and a balanced detector to measure the resulting interference intensity. 7

Figure 2.2 Amplitude distributions of the first guided photonic lantern modes for a step-index fiber. The illustration corresponds to a transverse cross-section of the fiber core. 13

Figure 2.3 Schematic illustration of light collection and emission in a mode-selective photonic lantern. Different spatial modes, indicated by distinct colors, are selectively separated or combined by the mode-selective photonic lantern. 14

Figure 2.4 Schematic of the few-mode optical coherence tomography system, including the mode-selective photonic lantern, illumination and detection components, and two reference arms, one for each mode. 16

Figure 3.1 Description of the geometry and parameters used to simulate the Gaussian focusing beam. The dashed lines show the trajectory in a crossing propagation. Variables are described in Table 3.5 of the Appendix. . 25

Figure 3.2 Flowchart describing the scattering process of the simulator. The randomly generated number is noted $\xi_i \in [0, 1]$ while p is the probability for biased versus unbiased scattering. 27

Figure 3.3 MCOCT Flowchart 28

Figure 3.4 Optical coherence tomography (OCT) signal reconstruction. Definitions of variables: TP_N, total pathlength; W_N, weight; L_N, likelihood; N, N^{th} collected photon packets; k, wavelength; $S_S(k_m)$, signal amplitude from the sample arm; $S_R(k_m)$, signal amplitude from the reference arm; $I(k_m)$, reconstructed OCT signal. 29

Figure 3.5 Optical fluence rates ϕ [W/cm^2/W$_{\text{incident}}$] comparison between (a) MCOCT and (b) MCX simulated with the same optical properties. (c) Comparison of optical fluence rates along x at $z = 1.5$ mm and $y = 0$ mm generated by MCOCT (red) and MCX (blue). (d) Comparison of optical fluence rates along z at $x = 0$ mm and $y = 0$ mm simulated with MCOCT (red) and MCX (blue). 34

Figure 3.6 Experimentally obtained (red) *vs.* simulated (blue) OCT A-lines using an imaging lens of $f = 30$ mm of (a) Phantom #1, (b) Phantom #2, (c) Phantom #3, and (d) Phantom #4. 35

Figure 3.7 Experimentally obtained (red) *vs.* simulated (blue) OCT A-lines using an imaging lens of $f = 75$ mm of (a) Phantom #1, (b) Phantom #2, (c) Phantom #3, and (d) Phantom #4. 36

Figure 3.8 Experimentally obtained (red) *vs.* simulated using a Gaussian beam (blue) *vs.* geometric focused (orange) *vs.* pencil (green) beam OCT A-lines using an imaging lens of with the focal length $f = 30$ in (a) and $f = 75$ in (b) of phantom 1. 41

Figure 4.1 (a) Schematic of the few-mode optical coherence tomography (FM-OCT) system including the modally-specific photonic lantern, the illumination and detection components, and two reference arms; one for each mode. (b, c) Coherent spread functions of the LP01 and LP11 modes, respectively. 45

Figure 4.2 (a) Axial normalized intensity profiles (linear scale) of a mirror acquired by the single-mode fiber (SMF, green), combined modally-specific photonic lantern (MSPL) channels (purple), MSPL Channel 1 (blue), and MSPL Channel 2 (red). In (b), the associated dispersion curves (before digital compensation). 48

Figure 4.3 *En-face* OCT images of a negative reflective USAF-1951 resolution test chart (a–d) with a zoom-in of the region delimited by the red square (e–h) for the specific modes of collections: single-mode fiber (SMF), combined modally-specific photonic lantern (MSPL) channels, MSPL Channel 1, and MSPL Channel 2. The system's edge responses in dB (i–l) for the vertical (corresponding to signals normalized from the green region, first row) and horizontal (corresponding to signals normalized from the blue region, first row) axes. The fields of view of the first and second rows are 1093 µm by 954 µm and 283 µm by 247 µm, respectively. 49

Figure 4.4 *En-face* OCT images of within a plastic cap engraved with the number 8 acquired with (a) the combined MSPL channels, (b) Channel 1, and (c) Channel 2. Speckle contrast (C_s) and SNR values are provided for each case. (d-f) Corresponding zoom-in images of the speckle pattern for each optical configuration. (g-i) *In vivo* B-scans of a fingernail and corresponding speckle contrast and SNR for each case. All images are displayed in dB scale. 51

Figure 5.1 Second-order autocorrelation curves ($g_{22}^{(2)}$) measured at lateral positions of 0, 80, 120, and 160 µm from the center of a cylindrical tube containing flowing milk. The color gradient from dark to light blue corresponds to increasing distance from the tube center. Dashed vertical lines indicate the positions of the second-peak maxima, which are used to estimate the flow speed. The estimated average flow speed in the tube is 16.7 mm/s. 55

Figure 5.2 Cross-correlation curves ($g_{12}^{(2)}$) for simulated particles moving at 8 mm/s, with diffusion coefficients of 0, 2, 4, 6, and 8 µm^2/s shown in blue, orange, yellow, purple, and green, respectively. 56

Figure 5.3 Theoretically possible correlation ratios ($\eta_{\mathrm{ij/kl}}$) calculated from all auto- and cross-correlation combinations when using two channels. Here, $\eta_{\mathrm{ij/kl}}$ denotes the ratio of the correlation between channels i and j to that between channels k and l. 57

Figure 5.4 En-face images of $|g_{22}^{(1)}|$ for a static object, with both axes corresponding to translations in the x and y directions. The detected polarization was altered between (a) and (b) using a polarization controller, resulting in the observed change in lobe orientation. 57

Figure 5.5 Measured flow velocities of pork blood in a cylindrical tube using a two-mode mode-selective photonic lantern. The black line represents the expected flow, while blue dots and green circles correspond to flow measurements obtained by v_{tot} and v_{sp}, respectively. The experiment demonstrates effective flow quantification even at low SNR values (≈ 3). 59

Figure 6.1 A few-mode optical coherence tomography system acquiring interferograms from all three channels of a mode-selective photonic lantern using two reference arms, one for LP01 and one for LP11 modes. Circulators (C1, C2, and C3), polarization controllers (PC) and a variable free-space delay line allow improved visibility and concurrent acquisitions, respectively. Theoretical coherent spread functions for Channels 1 (Ch1), 2 (Ch2), and 3 (Ch3) are shown in (b), (c), and (d), respectively. 68

Figure 6.2 Setup used to emulate blood flow. A tube containing flowing scatterers was put at the focus of the FM-OCT imaging head and tilted in plane (four values of θ), and out of plane (one value of ϕ). 70

Figure 6.3 Speckle correlation of an en-face image of a piece of plastic. The autocorrelation amplitude of Ch1 is shown in (a), while the cross-correlation amplitude of Ch1 and Ch2, and Ch1 and Ch3 are shown in (b-c), respectively. The second row (d-f) shows the respective theoretical values. 72

Figure 6.4 Experimental cross-correlation and auto-correlation ratios for (a) $\eta_{12/11}$, and (b) $\eta_{13/11}$ obtained for a static object. Ratio variations for (d) $\Delta\eta_{12/11}$, and (e) $\Delta\eta_{13/11}$, and their combination (f) $\Delta\eta_{\text{tot}}$. Subfigure (c) plots cross-sections of $\Delta\eta_{\text{tot}}$ shown in (f). 73

Figure 6.5 Laminar flow as measured by v_{tot} (blue crosses), v_{fit} (orange dots), and v_{sp} (yellow dots) as compared to theoretical values (solid black curve) at $\theta = 0°$ (column 1), $\theta = 30°$ (column 2), $\theta = 60°$ (column 3), and $\theta = 90°$ (column 4), and for flow speeds of 0.0 mm/s (a–d), 0.9 mm/s (e–h), 2.7 mm/s (i–l), 9.0 mm/s (m–p) and 36 mm/s (q–t). 74

Figure 6.6 Laminar flow as measured by v_{tot} (blue crosses), v_{fit} (orange dots), and v_{sp} (yellow dots) as compared to theoretical values (solid black curve) at the center of the tube for speeds of 0.0 mm/s (a), 0.9 mm/s (b), 2.7 mm/s (c), 9.0 mm/s (d), and 36 mm/s (e) with an effective axial tilt of ϕ =10°. 75

Figure 6.7 Laminar flow as measured by v_{tot} (blue dots), v_{fit} (orange dots), and v_{sp} (yellow dots) as compared to theoretical values (solid black curve) without an axial tilt (a) and with an effective axial tilt of ϕ =10° (b). 76

Figure 6.8 Standard deviation on laminar flow measurements done by v_{tot} (blue), v_{fit} (orange), and v_{sp} (yellow) for varying expected flow speed and an integration time of 50 ms (a) and for an expected flow speed of 3 mm/s and varying integration times. 76

Figure 6.9 Laminar flow as measured by the correlation ratio method in the x (light blue dots), y (blue dots) and z (dark blue dots) axes for transverse flow orientations of $\theta = 0°$ (a), $\theta = 30°$ (b), $\theta = 60°$ (c), and $\theta = 90°$ (d), with v_{tot} (blue crosses) and expected flow speed (solid black line). The corresponding measured angle is shown below in (e–h) respectively. The absolute difference from the expected angles is shown in (i) for all measures made in Fig. 6.5. 77

Figure 6.10 Laminar flow measured in a tube by v_{tot} (a-d) compared to v_{sp} (e-h) for flow speed of 0 mm/s (column 1), 0.9 mm/s (column 2), 1.8 mm/s (column 3) and 2.7 mm/s (column 4). The flow in the vertical axis of the tube is displayed in (i-l) with v_{tot} (blue), v_{sp} (orange), and the expected result (black solid line). 78

Figure 6.11 Laminar flow measured in a tube by v_{tot} (a-d) compared to using v_{sp} (e-h) for flow speed at the center of 0 mm/s (a,e,i), 0.9 mm/s (b,f,j), 1.8 mm/s (c,g,k) and 2.7 mm/s (d,h,l). The tube was tilted by an effective angle of $\phi = 10$ °. The flow in the center axis of the tube is displayed in (i-l) with v_{tot} (blue), v_{sp} (orange), and the expected result (black solid line). 79

Figure 7.1 First-order correlations and correlation ratios for a static sample. The first row displays the absolute values of $g_{11}^{(1)}$, $g_{12}^{(1)}$, and $g_{13}^{(1)}$, while the second row presents their corresponding phase values. The third and fourth rows show the phase values of $\eta_{12/11}$ and $\eta_{13/11}$, and $\Delta\eta_{12/11}$ and $\Delta\eta_{13/11}$, respectively. 87

Figure 7.2 Phase values of $\Delta\eta_{12/11}$ measured on flowing milk in a cylindrical tube at a maximum speed of 9 mm/s. The left panel illustrates results for two depth positions and multiple values of τ; the right panel aggregates data across all depths for a single value of τ. 88

Figure 7.3 Cross-correlation between Channel 1 and the synthetically recreated Channel 2, using Eq. 7.6, for a static object. The data and methodology match those of Fig. 6.3. The result deviates from the expected two-lobed structure, instead displaying an elongated Gaussian profile, the origin of which is still under investigation. 90

Figure 7.4 Comparison between correlation ratios calculated using the signal from a mode-selective photonic lantern and those reconstructed from Channel 1 alone. The first row presents the cross-correlation between channels, the second row displays the correlation ratio, the third row illustrates the variation of the correlation ratio, and the last row plots the central profile from the previous row. 92

Figure 7.5 Comparison between correlation ratios calculated from mode-selective photonic lantern signals and those reconstructed from Channel 1 using the second-order correlation function. The first row presents the cross-correlation between channels, the second row displays the correlation ratio, the third row illustrates the variation of the correlation ratio, and the last row shows the central profile of the previous row. 94

LIST OF SYMBOLS AND ACRONYMS

AGV	Axial gradient velocity
CSF	Coherent spread function
FM-OCT	Few-modes optical coherence tomography
LP	Linearly polarized
MSPL	Mode-selective photonic lantern
NA	Numerical aperture
OCT	Optical coherence tomography
OCTA	Optical coherence tomography angiography
PhD	philosophiae doctor
PL	Photonic lantern
LPMS	Lanterne photonique à mode-selectif
PSF	Point spread function
SMF	Single-mode fibers
SNR	Signal-to-noise ratio
TCO	Tomographie par cohérence optique
TCO-QM	Tomographie par cohérence optique à quelques modes

LIST OF APPENDICES

Appendix A CONTRIBUTIONS 124

CHAPTER 1 INTRODUCTION

1.1 Context

Biomedical imaging plays a critical role in both clinical research and the diagnosis and monitoring of diseases. Among the various imaging techniques available, photon-based modalities are particularly valued for their high resolution, non-invasive nature, and relatively low operational costs.

Optical coherence tomography (OCT) is distinguished by its non-invasive approach and high spatial resolution (approximately 10 µm), although its penetration depth is limited to approximately 1–2 mm. This modality is exceptionally well-suited for retinal imaging [1], as it exploits the optical properties of the eye to visualize distinct retinal layers and vasculature without the need for exogenous contrast agents. The advent of three-dimensional OCT imaging has profoundly transformed the field of ophthalmology. Between 2008 and 2015, the technology is estimated to have saved 11.1 billion US dollars in the United States, providing a return on investment of 21-fold [2].

OCT is not confined to retinal applications. Its high resolution is particularly advantageous for imaging epithelial tissues, where visualizing thin layers is essential and limited penetration depth is less problematic. Furthermore, OCT is compatible with fiber-based endoscopic approaches, enabling imaging of the esophagus, intestines, and arteries [3–5]. The small diameter of optical fibers (approximately 200 µm) also facilitates integration with probes designed for brain imaging.

The restricted penetration depth of OCT arises from the limited number of photons that can be collected during imaging. This constraint is partially attributed to the small fraction of photons that are retroreflected toward the optical fiber. Additionally, the employment of single-mode fibers (SMF) further reduces the amount of light that can be captured, as only photons matching the fundamental mode are guided.

Despite its widespread adoption, OCT exhibits inherent limitations. As a coherent imaging modality, it is susceptible to speckle noise, which can obscure fine structural details [6]. This limitation is especially pronounced in retinal imaging, where speckle noise may mask subtle anatomical features in the outer retina, such as the retinal pigment epithelium and Bruch's membrane [7].

Ophthalmology research has greatly benefited from OCT, which facilitates the longitudinal assessment of disease progression by enabling detailed visualization of retinal morphology and

vasculature. For instance, optical coherence tomography angiography (OCTA) can detect abnormalities in choroidal blood flow and identify choroidal neovascularization, particularly in cases of age-related macular degeneration [8,9]. However, while OCTA effectively highlights vascular structures, obtaining accurate and reproducible quantitative measurements remains a significant challenge [10, 11], thereby complicating comparative studies.

In ophthalmic imaging, lateral resolution is fundamentally limited by the optical properties of the eye, which functions as the imaging lens. The beam diameter is further restricted by the pupil size, thereby limiting the achievable numerical aperture (NA). This constraint is especially pronounced in studies involving small animal models, such as mouse pups [12].

Additionally, OCT predominantly generates image contrast from variations in sample reflectivity. While alternative contrast mechanisms—such as polarization-sensitive OCT [1,13] and OCTA for vascular imaging—have been developed to enhance its utility, the overall range of intrinsic contrast remains limited. This constraint restricts OCT's effectiveness in distinguishing between diverse tissue types and pathological conditions relative to other imaging modalities.

Because OCT relies on interferometry, SMF are required to prevent modal mixing, which would otherwise degrade depth resolution and image quality. However, due to the single-mode nature of these fibers, even photons that are retroreflected toward the fiber may not be efficiently coupled unless they match the fundamental mode. Photons corresponding to higher-order modes are not guided by SMF and are therefore lost. Importantly, these higher-order modes carry not only additional signal but also unique information distinct from that present in the fundamental mode.

The photonic lanterns (PL) is a relatively recent innovation in optical fiber technology, originally developed for astronomical applications [14]. The term 'photonic lantern' was inspired by the resemblance of early prototypes to traditional lanterns. Functionally, a PL can be described as an optical fiber coupler cleaved at the tapered region, forming an N-to-1 demultiplexer that distributes a complex wavefront among N fibers. A notable variation, the mode-selective photonic lantern (MSPL), demultiplexes each linearly polarized (LP) mode into a separate fiber, enabling the separation of higher-order modes at its tip into individual SMF. This capability has garnered significant attention for its potential applications. Integrating an MSPL with OCT allows for the collection of additional light that would otherwise be lost.

Previous efforts to utilize higher-order modes in OCT have been reported [14–16]. In these studies, the collection of higher-order modal light served as a novel source of contrast, enabling the differentiation of tissue composition and the identification of pathologies previ-

ously undetectable by conventional OCT. More recently, our group developed a fiber-based OCT system leveraging an MSPL—referred to as few-modes optical coherence tomography (FM-OCT)—which demonstrated promising potential for new applications [17]. The higher-order modes exhibited varying sensitivity depending on the sample's diffuser size, suggesting that this new contrast mechanism could exploit nuclear-to-cytoplasmic volume ratios to distinguish between cancerous and normal tissues. Furthermore, the unique coherent spread function (CSF) provided by FM-OCT may offer additional capabilities advantageous for biomedical research.

As this technology remains in its early stages of development, many of its prospective applications have yet to be explored and warrant systematic investigation. Further research is necessary to identify specific scenarios in which FM-OCT could augment the diagnostic performance of conventional OCT.

1.2 Project statement

The MSPL has garnered significant interest for its potential to enable a wide range of novel applications. Notably, it has been integrated with OCT to develop fiber-based FM-OCT. The MSPL separates the optical modal content into multiple channels, each of which can be used to generate an independent OCT image. The additional collected light can potentially enhance the performance of conventional OCT. Prior studies on FM-OCT have demonstrated its ability to produce distinct speckle patterns, enable new CSF, and potentially provide novel contrast mechanisms through inter-channel comparisons.

However, the extent to which these new capabilities translate into impactful applications remains unclear. Since the technology is still in its early stages of development, much of its potential is yet to be realized. Consequently, additional research is required to determine whether these promising concepts can yield practical and meaningful advances, rather than remain primarily of academic or technological interest.

1.3 Project objectives

This thesis investigates the feasibility of applications for a novel OCT, the FM-OCT. The primary aim is to determine specific applications for the FM-OCT and demonstrate their usefulness.

Specific Objective 1 [SO1]: Designing a multi-modal OCT system.

- Write the program for imaging with multiple channels for simultaneous multi-modal detection.
- Design a way to hold the MSPL as well as minimize the back reflection coming from its tip.
- Design, build, and align a two-mode FM-OCT.
- Upgrade the two-mode FM-OCT into a three-mode one.

Specific Objective 2 [SO2]: Developing tools to model OCT signal.

- Create a simulator capable of emulating multi-modal speckles and behaviors;
- Develop a theoretical model predicting multi-modal speckle behavior in the presence and absence of flow;

Specific Objective 3 [SO3]: Improving image quality using multi-modal content.

- Find a way to ensure axial coregistration of the different OCT signal;
- Predict the signal-to-noise ratio (SNR) and speckle contrast after combining the signal from multiple channels of an FM-OCT;
- Compare those predictions to a simulation;
- Image objects and in-vivo samples with an FM-OCT and observe the improvements to SNR and speckle contrast, as well as analyse any deterioration of the resolution.

Specific Objective 4 [SO4]: Improving blood flow measurement.

- Image a static object, calculate the autocorrelation function of the signal in space, and compare it to predictions, confirming both the MSPL quality and prediction correctness;
- Investigate the best way to exploit the new CSF to measure flow;
- Simulate to confirm the feasibility of the proposed method;
- Design and do a series of experiments comparing the new method to measure flow to existing ones.

1.4 Thesis outline

The thesis is presented in the following order:

- Chapter 1, Introduction: This part introduces the context of the problem statement. It covers the emergence of needs and technologies that led to the project statement. After the project statement, the thesis objective is introduced and decomposed into specific objectives.
- Chapter 2, Literature review: A brief literature review is introduced to help the reader understand the published articles in the thesis. The review covers introductory knowledge of OCT, optical fibers, PL, and methods for modeling light, speckles, and correlation in OCT. A deeper theoretical context is given in each article on the specific subject.
- Chapter 3, Article 1 - Simulating OCT signal through Monte Carlo: The publication presents the first experimental validation of an OCT signal simulated with a Monte Carlo method. It compared absorption maps with the existing simulator to first validate it as a light-propagation simulator, before comparing simulated OCT signal A-lines with experimental ones measured on a sample with known optical properties.
- Chapter 4, Article 2 - Speckle noise reduction and increased SNR: The article presents how combining the signals from two channels of an FM-OCT reduces the speckle noise while improving the SNR. A resolution analysis also shows that it has minimal impact on resolution.
- Chapter 5, Prior works on FM-OCT flow measurements: Unpublished prior results and methods that led to the published flow article are presented. The reasons they were ultimately abandoned and made obsolete are also presented.
- Chapter 6, Article 3 - Flow measurement: A novel method to measure flow using FM-OCT is presented along with a comparison to existing methods and error analysis on both precision and accuracy. The flow partial orientation capabilities of the new method are demonstrated through an error analysis.
- Chapter 7, Discussion: Unpublished results on advancements are presented on variations of the flow measurement method with inconclusively explored avenues, as well as a general discussion on the thesis contributions.

- Chapter 8, Conclusion: Recommendations as well as insights are presented to those interested in pursuing research in the same direction. The chapter summarizes the thesis with its most important achievements.

CHAPTER 2 LITERATURE REVIEW

This section provides an introductory literature review addressing topics not covered in the published articles but essential to understanding the thesis.

2.1 Optical coherence tomography

OCT was originally developed for imaging the retinal structure of the eye [18]. Since its inception, OCT has found new applications both within and beyond the biomedical field. It operates as an interferometric technique, wherein light reflected from the imaged sample (sample arm) interferes with light reflected from a reference mirror. Figure 2.1 illustrates a fiber-based OCT system. A 90%/10% coupler divides the output from a laser source between the reference and sample arms. Light is reflected from a mirror in the reference arm and from various depths within the sample in the sample arm. Circulators (C1 and C2) redirect the light toward a 50%/50% coupler, where interference between the two optical paths occurs. A polarization controller (PC) is employed to optimize the polarization state for maximal interference. A balanced detector then measures the resulting interference signal.

In contrast, a free-space OCT system employs beam splitters to divide the optical beam between the sample and reference arms. Such configurations generally exhibit lower dispersion compared to their fiber-based counterparts. However, their incompatibility with fiber-based catheters restricts their range of applications.

There are two principal types of OCT: time-domain and spectral-domain. Time-domain OCT, now considered obsolete, utilized a moving reference arm mirror to control the depth

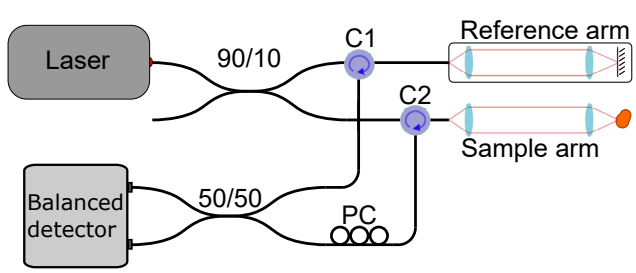

Figure 2.1 Schematic of a fiber-based optical coherence tomography system employing a 90%/10% coupler to split the light between the reference and sample arms, circulators (C1 and C2) to redirect the returning light toward the detector, a polarization controller (PC) to optimize polarization orientation for interference, a 50%/50% coupler to combine signals from both arms, and a balanced detector to measure the resulting interference intensity.

of interference, thereby achieving axial resolution. Spectral-domain OCT employs either a broadband laser in conjunction with a spectrometer or a swept-source laser with time-encoded wavelengths to simultaneously detect multiple wavelengths of light. The Fourier transform of the resultant interference pattern provides information about the depths and amplitudes of the sample's reflectivity, thereby yielding axial resolution [1, 19].

2.1.1 Speckle noise

As a coherent imaging technique, OCT is inherently affected by speckle noise [1]. This noise arises from the interference of light reflected by the several scatterers within a single pixel. Because the positions of these scatterers are arbitrary, the resulting interference—and thus the speckle pattern—is also arbitrary. The size of these patterns is directly related to the system's resolution and can obscure fine structural details or even larger features within the image.

In OCT, speckles are considered fully developed, resulting in a speckle contrast equal to one. The speckle amplitude adheres to a Rayleigh distribution, whereas its intensity is characterized by an exponential distribution [20].

Speckle patterns exhibit spatial correlation because the system's CSF typically extends slightly beyond the pixel size. For a static sample, speckle patterns remain static over time. However, when motion is present, such as during blood flow, the speckle pattern varies dynamically over time.

To address this challenge, multiple solutions have been proposed [21–52]. The most straightforward approach is to perform low-pass filtering of OCT images. However, this method also suppresses small structures. Similarly, averaging consecutive B-scans acquired at different positions can reduce speckle noise and emphasize larger structures, but it degrades resolution [21–34].

Alternatively, the sample can be scanned at different angles, resulting in different speckle patterns that can then be averaged to reduce speckle noise [35–39]. However, the improvement offered by this technique is limited and requires large differences in the measurement angle, which can be technically challenging or infeasible to achieve depending on the context. Certain algorithms attempt to distinguish and selectively remove speckle patterns, but these methods may still blur or remove small structures [40–50].

Neural network-based methods have also been applied with some success [51, 52], but these approaches require extensive datasets tailored to specific samples and, similar to the previous algorithms, may blur or remove intrinsic structures.

Despite the variety of proposed solutions, these approaches provide only partial mitigation, and speckle noise remains a significant challenge in OCT imaging and other coherent imaging techniques.

2.1.2 OCT signal

In spectral-domain OCT, the detected signal intensity arises from the interference between light returning from the sample and reference arms and is given by [1]:

$$I_{det}(k) = I_R(k) + I_S(k) + 2\sqrt{I_R I_S} \sum_{s=1} \alpha_n cos(k\Delta z_s) \exp\left(-\frac{1}{4\ln 2}\left[\frac{\Delta z_s \delta\omega_s}{c}\right]^2\right), \tag{2.1}$$

where I_R and I_S represent the wavelength-dependent intensities reflected from the reference and sample arms, respectively; k is the wavenumber; α_n denotes the sample reflectivity at depth Δz_n; $\delta\omega_s$ is the full width at half maximum (FWHM) of the measured wavelength; and c is the speed of light. The depth Δz_n corresponds to the optical path length difference between the reference and sample arms. The first two terms constitute the DC component of the signal and do not contain relevant structural information.

The third term can be further separated into the AC component, which encodes depth information, and the roll-off factor, represented by the exponential. The roll-off accounts for signal degradation with increasing depth, independent of optical attenuation, and arises from the system's finite spectral resolution.

The AC component contains the relevant structural information, encoding the depth at which light is reflected as a function of the wavenumber. The sample's scattering and absorption properties, as well as system transmission, are not included in this expression.

2.1.3 Resolution

Axial and lateral resolutions in OCT originate from distinct physical principles and are thus independent parameters. The axial resolution is given by [53]:

$$\delta z = \frac{2\ln 2}{\pi}\frac{\lambda_0^2}{n\Delta\lambda}, \tag{2.2}$$

where λ_0 is the central wavelength, $\Delta\lambda$ is the spectral width of the light source, and n is the refractive index of the medium. As a result, axial resolution improves in media with a higher refractive index compared to air.

Lateral resolution, in contrast, is determined by the width of the incident beam on the sample,

analogous to confocal microscopy [53]:

$$\delta x = 0.56\frac{\lambda_0}{\mathrm{NA}}, \tag{2.3}$$

where NA is the numerical aperture of the system. NA itself depends on the focal length of the imaging lens and the beam width at the lens. In retinal imaging, the eye functions as the imaging lens, and, particularly for small mammals, the pupil limits the maximum achievable beam width. Accordingly, lateral resolution in retinal imaging is less easily controlled when imaging small mammals' retinas.

The system's NA also affects the depth of field:

$$\mathrm{FOV}_z \approx \frac{0.9n\lambda}{\mathrm{NA}^2}. \tag{2.4}$$

An increase in NA results in a reduced depth of field. Therefore, a trade-off between lateral resolution and depth of field is required when optimizing system parameters.

2.1.4 Sample scanning

To acquire two- or three-dimensional images, a scanning system is essential. An A-line is produced by a single measurement at a specific point, resulting in a one-dimensional axial line of pixels. A two-dimensional image, known as a B-scan, is obtained by translating the beam across the sample. When scanning is extended into a third dimension, a C-scan is generated [1, 19].

Scanning is typically accomplished using a galvanometrically mounted mirror. Two principal scanning schemes can be distinguished: telecentric and non-telecentric [1]. Telecentric scanning translates the beam laterally across the sample and is the most commonly employed method. Non-telecentric scanning, predominantly utilized for retinal imaging, alters the beam's angle at the pupil, thereby projecting this angular change onto different regions of the retina.

Alternatively, full-field OCT acquires an entire C-scan simultaneously using a camera to image multiple A-lines in parallel, rather than by sequentially scanning the sample. This approach enables faster C-scan acquisition. However, it is incompatible with fiber-based catheters and is more susceptible to bulk tissue motion artifacts [1].

2.1.5 Signal processing

OCT measurements produce an interferogram that requires signal processing to generate an image. The first step is to linearize the spectrum with respect to k. While Equation 2.1 expresses the OCT signal as a function of k, in practice, the measured signal is not sampled perfectly linearly. This nonlinearity arises because swept-source lasers do not sweep linearly in k. A k-clock can be employed to synchronize measurements to a linear k-space. Alternatively, calibration measurements can be performed to resample and linearize the data [54]. Spectrometer-based systems may also require k-linearization to address similar issues.

Because the wavenumber depends on the refractive index, dispersion within both the system and the sample can distort the signal and degrade axial resolution. Several methods exist for dispersion correction. The primary approach is to empirically balance dispersion between the sample and reference arms as closely as possible. Residual system dispersion can then be characterized through calibration and numerically corrected [54]. Sample-induced dispersion may be mitigated using iterative numerical techniques that maximize image sharpness [55].

The DC component of the signal can also be removed, as it primarily introduces artifacts at the top of the image. A low-pass filter can be applied to eliminate this component. Alternatively, in fiber-based systems, balanced detectors are commonly used to suppress the DC component and isolate the AC signal containing the relevant spectral information.

The system's overall transmission, which may vary with wavelength, can introduce a wavelength-dependent modulation of the signal. This effect can alter the axial point spread function (PSF) shape. To improve the PSF, the signal envelope can be measured and normalized to mitigate these influences.

The FFT algorithm used for the Fourier transform requires the spectrum to approach zero at both ends; otherwise, distortions can be introduced into the image. Therefore, a Hanning window is typically applied to the spectrum prior to transformation. Other window functions may also be used, each offering a specific trade-off between the sharpness of the central peak and the magnitude of secondary lobes in the axial PSF.

After the Fourier transform is applied, the resulting complex signal contains both the image and its mirror image, arising from negative-frequency components. Some systems utilize these negative frequencies to extend the maximum imaging depth; otherwise, only the positive frequencies are retained.

The magnitude of the resulting signal constitutes the OCT image, while its squared value yields the OCT intensity image. Both representations are typically displayed on a logarithmic scale.

2.2 Optical fibers and higher-order modes

Light propagates within step-index optical fibers as LP modes, each describing a distinct spatial distribution of the light's amplitude when guided. The total optical field in the fiber is a superposition of all guided, orthogonal modes. Figure 2.2 illustrates the amplitude distributions of the first guided modes for a step-index fiber. Depending on the fiber's core size and NA, a theoretically infinite number of modes may be supported.

Different modes propagate through the fiber at varying velocities due to their distinct effective refractive indices. Mode mixing can occur when the fiber experiences mechanical perturbations, such as pinching or bending, which induce modal coupling.

This modal mixing poses significant challenges for fiber-based interferometric systems. Because each mode has a unique effective refractive index, random switching between modes alters the optical phase, rendering stable interference with a signal from another fiber unfeasible. SMF are typically employed to mitigate this problem.

SMFs are designated as such because only the fundamental mode (LP01) is guided, thereby eliminating modal mixing. For this reason, fiber-based OCT systems utilize SMF. However, an SMF can only collect the portion of light matching the LP01 mode distribution.

Any arbitrary wavefront of light can be mathematically decomposed into a sum of constituent wavefronts, with LP modes forming a suitable basis set for this purpose. Since only the LP01 mode is guided by theSMF, only the portion of the light field that can be described by LP01 is collected, effectively limiting both the detected signal and the information content. As a result, OCT signals are restricted, and information present exclusively in higher-order modes is rejected.

Free-space OCT systems encounter analogous challenges. If certain modes are present in the sample arm but absent in the reference arm, they will not interfere and, thus, will not contribute to the OCT signal. One strategy to address this issue involves introducing light with high modal content into the reference arm and employing a detector array, rather than a single-pixel detector, to capture the spatial structure of the interference wavefront, as implemented in full-field OCT [1]. In such configurations, the presence of higher-order modal content enables enhanced transverse resolution, permitting parallel acquisition of multiple A-lines. However, these systems are restricted to free-space operation and are incompatible with fiber-based catheters or the demultiplexing of signals from distinct modes.

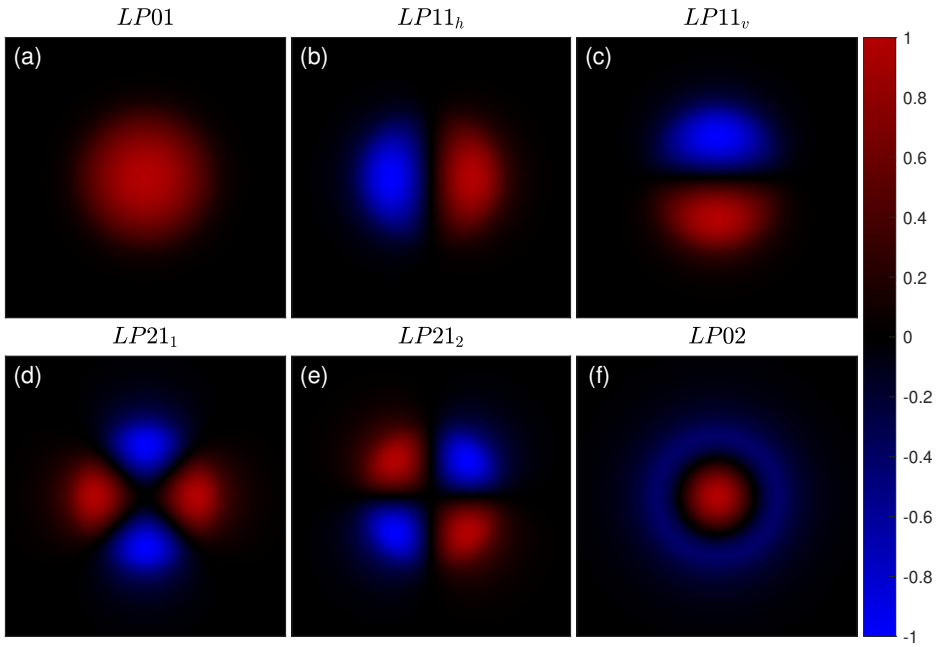

Figure 2.2 Amplitude distributions of the first guided photonic lantern modes for a step-index fiber. The illustration corresponds to a transverse cross-section of the fiber core.

2.3 Mode-selective photonic lantern

MSPL [16,56–58] are a specialized type of PL [14] that functions as modal multi/demultiplexers. The term 'photonic lantern' is somewhat of a misnomer, as these devices bear no relation to actual lanterns. In essence, a PL is a fiber-based coupler that is cleaved at its tapered region. The tapered section, where fibers from multiple branches merge, facilitates the mixing of optical modes from each branch. This is accomplished by tapering the coupler, thereby reducing the radius of the combined fibers and effectively transforming the taper into a larger single fiber that supports additional guided modes. These new modes closely resemble those of step-index fibers, as depicted in Fig. 2.2, due to the geometric similarity between the taper and step-index structures.

The tapered region can support higher-order modes beyond those supported by the individual connected fibers, and the mixing of these modes enables the coupling of light between branches. By cleaving the coupler at its taper, higher-order modes can be introduced or extracted via the taper region. The resulting structure functions as a PL, capable of collecting higher-order modes and distributing optical power among its output branches.

The MSPL is a variation in which the selection of fused fibers and the taper geometry are

precisely engineered so that each higher-order mode is selectively transmitted to a designated branch rather than being randomly distributed among all branches, as depicted in Fig. 2.3. This figure illustrates the selective demultiplexing of light into different branches according to modal content; conversely, the device can operate as a multiplexer in the reverse direction. Each branch of the MSPL can be interfaced with parallel OCT systems, enabling imaging with higher-order modes and facilitating FM-OCT [17]. Each collected mode thus corresponds to a distinct OCT channel, producing parallel images.

2.4 Few-mode optical coherence tomography

Fiber-based OCT is typically performed with an SMF, which restricts signal collection to the fundamental (first-order) mode. When a multi-mode fiber is employed, higher-order modes can also be collected. Because these modes are orthogonal, interference occurs only when light is carried by the same mode in both arms. If a multi-mode fiber is used in OCT, higher-order modes are collected, but they will not interfere with the reference arm signal if the reference arm supports only the first-order mode. Additionally, different modes exhibit distinct effective refractive indices, resulting in varying propagation delays and producing images at different depths. Finally, bending a multi-mode fiber can induce modal coupling, which mixes and scrambles the signal. For these reasons, OCT systems are generally limited to using only the fundamental mode.

In recent years, efforts have been made to exploit higher-order modes for OCT imaging. Interference was achieved between the light emerging from a few-mode fiber in the sample arm and an SMF in the reference arm [15, 59]. The two signals were combined in free space using a lateral offset. Without this offset, the modes, being orthogonal, would not interfere. The lateral displacement enabled partial overlap between different modes, allowing sufficient interference to produce an OCT image.

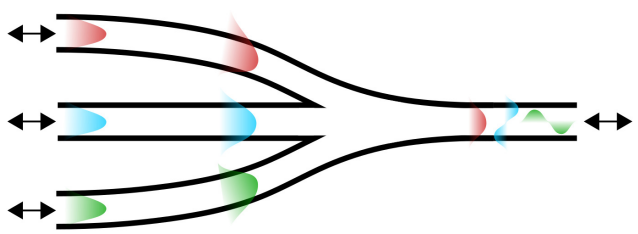

Figure 2.3 Schematic illustration of light collection and emission in a mode-selective photonic lantern. Different spatial modes, indicated by distinct colors, are selectively separated or combined by the mode-selective photonic lantern.

Because of differences in optical path length among the modes, images formed from each mode appeared at distinct depths. Modal mixing was minimized by maintaining the few-mode fiber in a fixed position during imaging.

Bright- and dark-field OCT images generated with this approach could distinguish microparticles of different sizes, even when they were below the system's nominal resolution. The utility of this new contrast mechanism was demonstrated on ex vivo tumorous tissue in glioblastoma and on neuritic plaques in Alzheimer's disease [15]. Another group developed a few-mode fiber OCT system and demonstrated its angularly diverse imaging capability, achieving a novel type of contrast [59].

Our group previously developed a fiber-based FM-OCT system using an MSPL [17]. The MSPL serves as a modal demultiplexer in the sample arm, separating each collected mode into individual SMF. The signal from each SMF is then imaged independently using parallel OCT systems. A schematic of a two-mode FM-OCT setup is shown in Fig. 2.4.

FM-OCT was shown to provide a distinct contrast depending on microparticle size and to yield different PSF characteristics for each mode.

2.5 Modeling light

There are several approaches to modeling light, each with specific advantages and limitations. In the context of this thesis, two distinct methods were investigated: the Monte Carlo technique and the randomly positioned particle mirror method. As Monte Carlo simulations are discussed in detail in the subsequent chapter, the present section focuses on the second approach.

A straightforward method to simulate speckle in imaging is to model the sample as an ensemble of particles that perfectly retroreflect light toward the detector. This approach is a variation of methods previously described in the literature [60, 61] and closely resembles the modeling strategies employed in OCT autocorrelation studies [62–64].

The light field is modeled at the beam waist, where the wavefront is assumed to be perfectly planar. The amplitude distribution in the transverse directions, corresponding to the system PSF or CSF [65], can be specified arbitrarily—for instance, using a Gaussian profile for a Gaussian beam. Scatterers are represented as particles randomly distributed in space, each acting as a perfect retroreflector. The incident wave is approximated as neither absorbed, attenuated, nor scattered during propagation through the medium. The measured signal is then given by the sum of all retroreflected contributions:

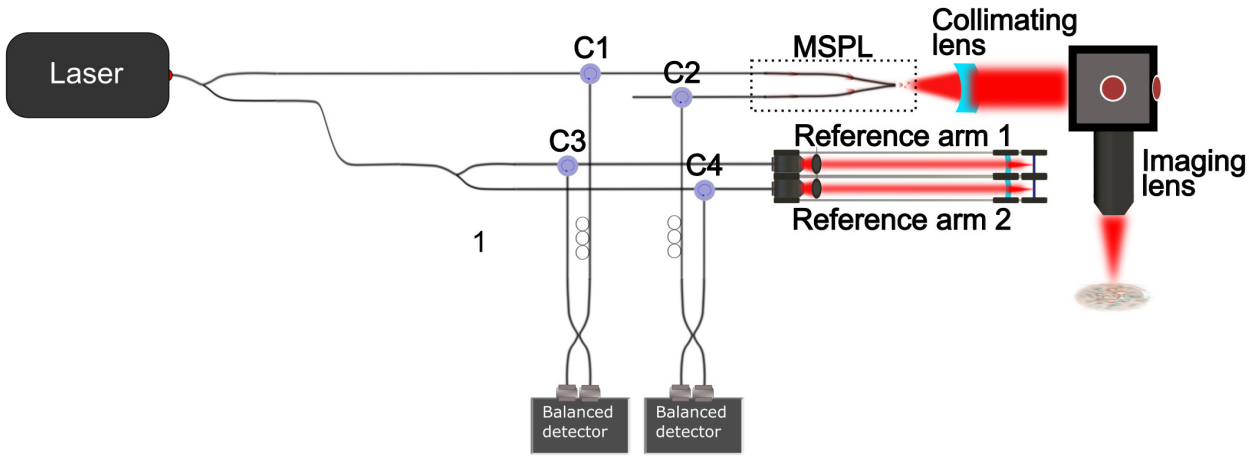

Figure 2.4 Schematic of the few-mode optical coherence tomography system, including the mode-selective photonic lantern, illumination and detection components, and two reference arms, one for each mode.

$$E = \sum_{n=1}^{N} e^{\frac{x_n^2+y_n^2}{w}} e^{-i2k_n z_n}, \tag{2.5}$$

where E is the complex amplitude (magnitude and phase) of the electric field from a single pixel, n indexes the simulated scatterers, N is the total number of scatterers, x_n, y_n, and z_n are the spatial coordinates of each scatterer, w is the width of the Gaussian distribution used to model the field, and k_n is the wavenumber of the simulated light. The first exponential term in the summation defines the signal amplitude, while the second term encodes the phase.

The Gaussian distribution is provided as an example; any distribution appropriate to the modeled scenario may be employed. For instance, $xe^{\frac{x_n^2+y^2}{w}}$ can be used to simulate detection by the LP11 mode. The field distribution function may also depend on the axial (z) coordinate, depending on the application.

Typically, 10 to 20 particles are sufficient to emulate speckle statistics [60]. Because the field distribution is finite (i.e., the simulated beam is not infinitely large), particles should be randomly distributed only within the region where the beam amplitude remains significant.

To simulate flow, the scatterer positions can be updated over time, leading to a time-varying signal:

$$E(t) = \sum_{n=1}^{N} e^{\frac{x_n(t)^2+y(t)^2}{w}} e^{-i2k_n z_n(t)}, \tag{2.6}$$

where t is the time at which E is calculated, and each particle can move with distinct velocities or directions. As particles migrate out of the PSF range, the signal amplitude gradually decreases. To maintain a consistent simulation, additional particles are introduced from the direction of flow, ensuring an average of 10 particles near the center of the PSF.

Similarly, multiple adjacent pixels can be simulated by translating the center of the PSF, analogous to a system scanning its beam over the sample. This approach enables the generation of spatially correlated speckle patterns in the simulation. Shot noise can be incorporated by adding a random complex value to each measurement independently.

While multiple scatterers are required to generate speckle patterns, a single scatterer is sufficient for simulating signal correlation in flow studies [63,64]. In this case, instead of randomly distributing many scatterers, the average signal is computed over all possible scatterer positions. As before, positions where the PSF approaches zero are excluded from the simulation due to the finite extent of the modeled field.

This model has proven useful for validating theoretical predictions related to speckle phenomena. It can be employed to investigate changes in the speckle autocorrelation induced by flow or to assess how speckle contrast is affected when multiple PSF are combined.

2.6 Flow measurement

Although speckle noise is often considered detrimental, it can also be utilized advantageously. OCTA leverages temporal variations in the speckle pattern to identify blood vessels [1]. This process typically involves acquiring several consecutive B-scans and calculating the variance for each pixel across these scans. While the variance values may be indicative of flow speed, they do not provide quantitative measurements.

Some research groups have developed look-up tables associating variance measurements with flow speed; however, these estimations depend on several other parameters which may compromise reliability [66, 67].

Doppler OCT enables precise and accurate measurement of flow velocity in the axial direction [68]. However, most retinal blood vessels are oriented in-plane and orthogonal to the imaging axis. Some systems acquire images of the retina at three different angles to address this limitation [69]. Implementing such systems can be technically challenging or even infeasible, particularly in the small eyes of mice [70]. Moreover, recent studies have shown that this method can overestimate flow speed [10]. It also imposes a limit on the maximum measurable flow speed [62].

Neural networks have also been applied to this problem, but they have achieved only limited

success and tend to overestimate flow speeds [71].

Speckle decorrelation provides an alternative approach for quantitative measurements [62–64]. This method is applied in a similar manner to speckle variance. Several consecutive scans are acquired, and the temporal image correlation is calculated.

Speckle decorrelation can be used in conjunction with speckle variance, where variance is used to locate blood vessels, and correlation provides a quantitative estimate of flow speed [67,72].

Although primarily used for angiography, correlation-based approaches have broader applications. For example, they can be employed to correct image distortions caused by non-uniform rotational scanning speeds [4].

Flow velocity is determined by measuring decorrelation at a specific delay or at multiple delays, with the latter approach involving fitting the correlation curve to estimate particle speed. When using a single delay for flow measurement, parameters such as diffusion, signal-to-noise ratio, and bulk motion must be accurately known; otherwise, they can introduce bias. Fitting the correlation curve across multiple delays is more robust to these sources of error, but it is also more challenging to implement, as it requires imaging the same point at very short intervals. Even when these factors are adequately addressed, inaccuracies can arise due to Axial gradient velocity (AGV) and shadow artifacts [10,73]. AGV refers to the non-uniform axial component of flow within a single pixel, with sub-resolution variations resulting in an overestimation of flow speed. Additionally, estimating sub-diffusive blood speed remains problematic [74].

A key advantage of correlation methods is their ability to be modeled with relative ease and accuracy, facilitating quantitative flow measurements without reliance on potentially inaccurate look-up tables.

Two main variants are commonly employed: first-order correlation ($g^{(1)}$), which correlates the complex field (E) of the OCT signal, and second-order correlation ($g^{(2)}$), which correlates the signal intensity (I). For fully developed speckle patterns [62], a fully correlated signal yields $g^{(1)} = 1$ and $g^{(2)} = 2$, whereas a fully decorrelated signal yields $g^{(1)} = 0$ and $g^{(2)} = 1$.

The measured correlation approaches its theoretical expectation only as the sample size becomes very large; smaller sample sizes introduce random fluctuations in the calculated values. As the sample size increases, the measured correlation converges toward the expected value. Although not widely discussed in the OCT literature, these fluctuations are most pronounced at low correlation values and are absent for fully correlated signals, as observed in the autocorrelation curves of moving samples.

Smaller correlation windows—defined by the number of pixels and the temporal span over

which correlation is calculated—provide higher spatial or temporal resolution but decrease correlation accuracy.

First- and second-order correlation methods are not equivalent. The first-order correlation is more accurate and provides information about the Doppler effect, but requires phase stability within the system, which may be technically challenging to achieve. The second-order correlation is simpler and more robust, but offers lower accuracy.

Despite the range of proposed methods, achieving accurate quantitative flow measurements in all dimensions remains a significant challenge.

CHAPTER 3 ARTICLE 1 - MCOCT: AN EXPERIMENTALLY AND NUMERICALLY VALIDATED, OPEN-SOURCE MONTE CARLO SIMULATOR FOR OPTICAL COHERENCE TOMOGRAPHY

This publication presents the first experimental validation of a Monte Carlo simulator for OCT image generation. Although several such simulators have been developed, prior validations were limited to theoretical assessments. The project originated as a postdoctoral project of Udayakumar Kanniyappan, with support from Raphaël Maltais-Tariant, and was subsequently continued by Raphaël and ultimately completed by Khaliun Erdenedalai under Raphaël's supervision.

The objective of this study was to validate Monte Carlo methods for accurate OCT signal simulation by reproducing experimental attenuation curves as functions of both the sample's optical properties and the system's numerical aperture.

The potential applicability of this approach for simulating FM-OCT signals was not examined in this publication.

Contribution: Raphaël Maltais-Tariant is co-first author with then-MSc student Khaliun Erdenedalai and contributed to 50% of the overall work. His contributions included supervising literature research, providing guidance throughout the project, and developing the initial working version of the code, accompanied by a detailed plan and comprehensive commentary. He also proposed and explained new features to be incorporated into the codebase.

He authored the experimental protocol and collaborated with Khaliun on the analysis of results.

He assisted in structuring the manuscript, revised and supplemented the first draft prepared by Khaliun, and authored several parts. Following submission, he drafted the responses to reviewers and implemented all requested revisions in the manuscript.

Prof. Mathieu Dehaes, PhD, and Prof. Caroline Boudoux, Pr. Eng., PhD, served as principal investigators for this project. They provided guidance throughout the project and contributed to the revision of the article.

Authors: Khaliun Erdenedalai, Raphaël Maltais-Tariant, Mathieu Dehaes, and Caroline Boudoux.

Abstract: Here, we present MCOCT, a Monte Carlo simulator for optical coherence tomography (OCT), incorporating a Gaussian illumination scheme and a bias to increase backscattered event collection. MCOCT optical fluence was numerically compared and validated

against an established simulator (MCX) and showed concordance at the focus while diverging slightly with distance from it. MCOCT OCT signals were experimentally compared and validated against OCT signals acquired in tissue-mimicking phantoms with known optical properties, showing a similar attenuation pattern with increasing depth while diverging beyond 1.5 mm and proximal to layer interfaces. MCOCT may help in the design of OCT systems for a wide range of applications.

Article published: Biomedical Optics Express, January 2024

DOI: 10.1364/BOE.504061

Submitted: 06 septembre 2023

3.1 Introduction

Optical coherence tomography (OCT) is a high-resolution, non-invasive imaging technique increasingly used for medical and biological applications. It is based on the principle of low-coherence interferometry, which relies on utilizing a light source with a broad wavelength bandwidth to ensure coherence gating, thus leading to a high axial resolution of a few microns [75]. In OCT systems, an interference spectrum is created by combining the reflected light from a reference mirror with that from the sample arm. This pattern is used to obtain a reflectance profile of the sample as a function of depth, namely an OCT A-line. OCT imaging primarily relies on detecting ballistic and quasi-ballistic backscattered photons from turbid environments, such as biological tissues. As light penetrates deeper into the tissue, its intensity decreases exponentially due to scattering and absorption, subsequently limiting the imaging depth to a few millimeters. OCT is now a standard diagnostic tool in the field of ophthalmology and a promising candidate in various other fields, including cardiology, dermatology, gastroenterology, and laryngology [76–79].

Light propagation in a turbid medium can be modeled in simple geometries by analytically solving the radiative transfer equation (RTE) [80]. However, when imaging biological tissue with high scattering properties, the mean free path of light within the tissue is short, which renders the RTE calculation and its inverse problem reconstruction too complex. In such cases, numerical simulation techniques using Monte Carlo (MC) methods have emerged as the gold standard for modeling photon interactions in biological tissue [81–86]. With MC, light is considered a collection of photon packets tracked as they undergo multiple events of reflection, refraction, absorption, and scattering while traveling through the turbid medium. Over the past years, several MC algorithms have been developed, amongst which Monte Carlo multi-layered (MCML) is the most widely known, forming the foundation of numerous

other simulators for biomedical applications [83]. In MCML, an ensemble of photon packets is launched as a pencil beam and perpendicularly to the surface of a multi-layered medium, with a simulated beam geometry that is cylindrically symmetric around the z-axis. The use of voxels, tetrahedrons, and 3D volumetric meshes further allowed the extension of planar and cylindrical geometries to model more realistic tissue structures [85, 87–90]. To accelerate the speed and improve computational efficiency, it was also proposed to use a graphics processing unit (GPU), enabling simultaneous simulations of a higher number of photon packets [91, 92]. Monte Carlo methods were previously applied to simulate OCT signals [84, 93–100] and some open-source OCT simulators recently became available [101–103]. Monte Carlo simulation for tissue layers with embedded objects for OCT (MCEO-OCT) is a modified version of MCML that embeds geometric shapes in the multi-layered tissue to mimic vessels and utilizes the method of importance sampling to accelerate the computation time [101]. The OCT massively parallel simulator (OCT-MPS) is based on an MC approach that exploits a tetrahedron mesh and GPU programming [102]. These two simulators were developed for time-domain OCT applications as only photons describing a path length difference with the reference path length smaller than the coherence length of the OCT system are tagged as contributing to the signal. For Fourier-domain applications, three MC simulators have previously been developed: one uses a layered tissue geometry with Gaussian beam focusing [104], another exploits a 3D voxel system with a pencil beam [105], while the third tool proposed an acceleration scheme based on importance sampling with a phase-function depend on wavelength [103]. The latter tool is open-source. These tools can be used to understand OCT signals better, aid in the instrumental design and development of OCT-based applications, guide the development of OCT signal processing algorithms, and more recently train neural networks to improve OCT image reconstruction [84, 93–99, 101, 102, 104–107].

In this work, we propose an open-source Fourier-domain simulator, MCOCT, modified from MCML 3D voxel geometry *mcxyz*, in which we implemented modifications to accommodate the particular requirements of Fourier-domain OCT. To achieve depth-resolved reflectometry in addition to simulating photon propagation, photon packets are simulated at a single central wavelength and tracked to record their traveled distance and extract phase as a function of wavelength. This strategy allows mimicking coherence gating. A photon detection system with an angle of acceptance was also implemented to mimic the numerical aperture of the imaging system [84]. To achieve a significant signal-to-noise ratio and expedite computation time, importance sampling was also employed [98, 108]. Gaussian illumination was further incorporated to model the light intensity profile and better represent OCT imaging. For numerical validation, the optical fluence rate generated by MCOCT was compared to the one simulated by Monte Carlo eXtreme (MCX) [92] using the same optical properties and

geometry. For experimental validation, OCT signals generated by MCOCT were compared to OCT signals acquired at specific numerical apertures in synthetic phantoms with known optical properties.

3.2 Material and methods

In the following subsections, we will sequentially describe the specific parts of the MCOCT simulator.

3.2.1 Monte Carlo photon propagation

A standard MC simulation starts with the launch of a photon packet into a medium that is defined by its index of refraction n, absorption coefficient μ_{a}, scattering coefficient μ_{s}, and anisotropy coefficient g [83]. For voxel-based approaches, each voxel is associated with a tissue type and its optical properties. Photon packets randomly propagating through the geometry are associated upon launch with a weight $W = 1$ representing the packet intensity that decreases as it undergoes events. At the site of an absorption interaction, W is updated according to $W = W \cdot \exp -(\mu_a \cdot s)$, where s is the distance traveled by the photon in that step [83]. In the case of a scattering interaction, the diffusion direction is calculated from the azimuthal angle ϕ and the deflection angle θ_{s} [80]. ϕ is uniformly distributed in the range $[0, 2\pi]$, whereas θ_{s} is typically modeled by the Henyey-Greenstein (HG) function f_{HG} that depends on the optical properties of the medium [109,110]. Since most biological tissues have an anisotropy coefficient $g \in [0.90, 0.95]$ at the clinically applied wavelengths of OCT, the photons are more prone to scatter in the forward direction [111]. When W is below a predetermined critical threshold, a roulette process begins in which the photon packet is associated with a probability to continue its propagation, otherwise, the sequence is terminated for this particular photon packet, and W is zeroed [83]. The simulation ends upon the termination of all photon packets.

3.2.2 OCT signal simulation

In order to simulate OCT A-lines, we introduced a new beam-focusing method based on Gaussian beams, used statistical methods to increase the probability of photon detection, tracked photons path lengths, and incorporated a system mimicking photon illumination and detection.

Gaussian beam description

In OCT, beam focussing impacts both signal intensity and resolution. The diffraction-limited focal spot of a Gaussian beam at a certain wavelength λ is determined by its beam waist w_0. Employing the paraxial approximation, the beam waist can be described as $w_0 = 2\lambda f/(\pi \cdot D)$, relative to the focal length of the imaging lens f, the beam center wavelength λ and the beam diameter at the lens D [112]. In OCT imaging, light propagates through several layers of different indices of refraction n_i with each layer affecting the axial position and the width of the beam waist, i.e., the beam curvature. Figure 3.1 illustrates the curved trajectory of such a beam depicting the individual parameters where $z = 0$ corresponds to the sample surface, described by the red line. The position of the focus in the tissue is given by z_f and the distance between the tissue surface and imaging lens by $z_{f,I}$, presenting a more general approach compared to assuming the focusing lens to be at $z = 0$ [112].
To implement this beam curvature in the MC method, the beam was focused by propagating photons along the trajectory by a small step unit $s_{\min}$ to the next position (x, y, z). Thereby, the unit of the step size is defined by the optical properties of the tissue. After each step, the direction unit vector $\hat{u}$ is updated to ensure precise photon tracking along the initial trajectory. Considering a photon propagation through two layers of differing refractive indices n_1 and n_2, the beam waist of the initial beam in a medium with n_2 can be described as

$$w_{0,n_2} = \frac{\lambda \cdot n_2}{\pi \cdot n_1 \cdot \arctan\left(\frac{D}{2f}\right)} \,. \tag{3.1}$$

The Rayleigh range of the beam z_R in the medium of n_2 is

$$z_{R,n_2} = \frac{\pi \cdot w_{0,n_2}^2 \cdot n_2}{\lambda_0} \tag{3.2}$$

and the radius of curvature of the beam $R(z)$ in the medium at a position z can be expressed as

$$R_{n_2}(z) = -z_{f,L} \cdot \left(1 + \frac{z_{R,n_2}}{z_{f,L}}\right)^2 , \tag{3.3}$$

where $z_{f,L}$ is the axial distance between the focal plane in the medium and the photon position, which is updated after the photon moves. The resulting direction vector has an orientation perpendicular to the radius of the curvature of the beam and is consequently given by

$$\hat{u} = \frac{1}{\sqrt{1 + \frac{x^2+y^2}{R_{n_2}(z)^2}}} \left(-\frac{x}{R_{n_2}(z)}, -\frac{y}{R_{n_2}(z)}, 1\right) . \tag{3.4}$$

The photon packet propagates by $s_{\min}$ until it undergoes its first scattering event, after which it propagates in accordance with a traditional MC simulation [83]. To allow the photon packet to follow a curved path, the packet is moved by a distance $s_{\min}$ before its direction $\hat{u}$ is recalculated using Eq. 4. The photon is moved this way until it has traveled the entire distance s. To assess the performance of the Gaussian illumination, simulations were performed with a pencil beam and a geometric focused beam [83, 92].

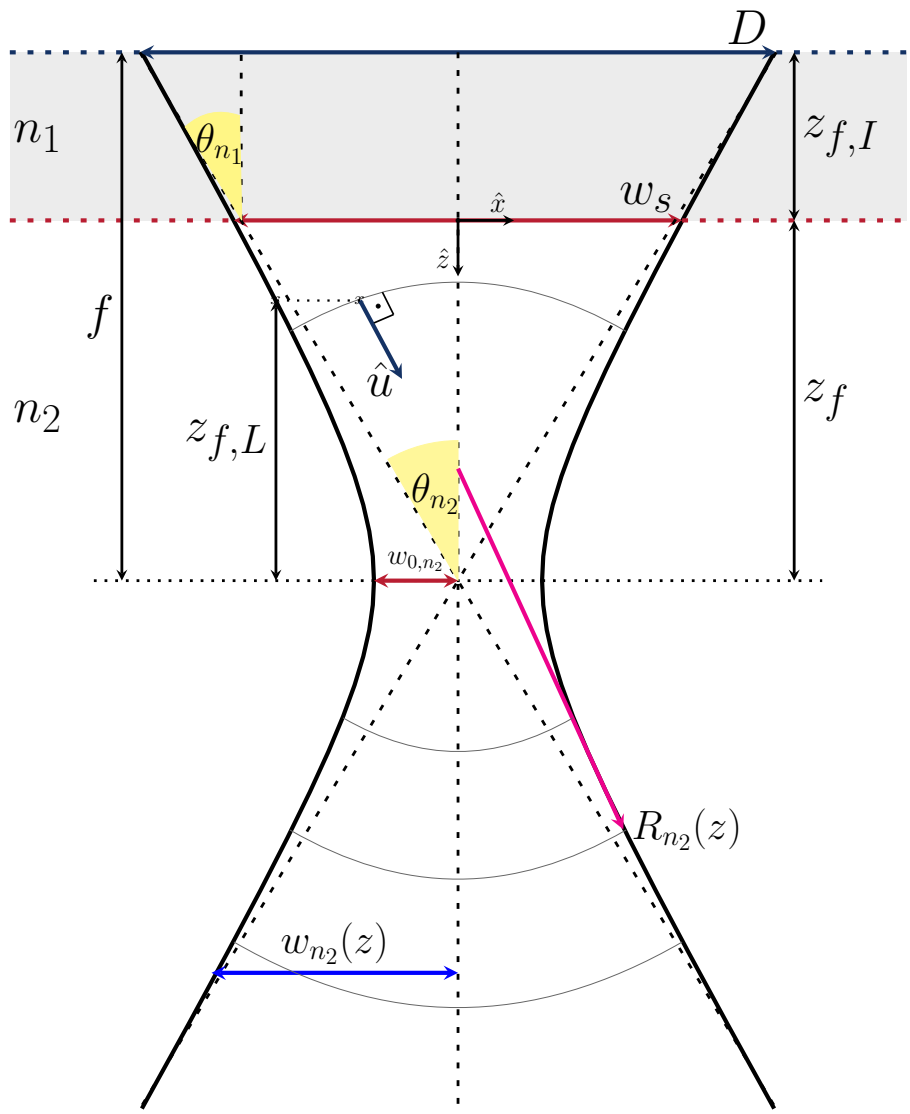

Figure 3.1 Description of the geometry and parameters used to simulate the Gaussian focusing beam. The dashed lines show the trajectory in a crossing propagation. Variables are described in Table 3.5 of the Appendix.

Importance sampling and photon splitting methods

To increase the probability of backscattering events, the method of importance sampling was implemented and combined with photon splitting (see flowchart in Fig. 3.2) [98,108]. Importance sampling is a probabilistic method to accelerate MC simulations for OCT by biasing random events leading to backscattering, thereby increasing the probability of photon detection and thus enhancing computational efficiency. An updated biased scattering function f_B based on the HG probability density function f_{HG} was then introduced. After a scattering event, this function modified the photon propagation direction to be oriented towards the detector, i.e., the collecting fiber system. The resulting bias was corrected by introducing a corresponding likelihood ratio as

$$L(\cos\,\theta_B) = \frac{f_{HG}(\cos\,\theta_S)}{f_B(\cos\,\theta_B)}, \tag{3.5}$$

where L expresses the ratio between the probability of observing the biased scattering angle in an unbiased simulation θ_S and in a biased simulation θ_B. This likelihood ratio was tracked throughout all scattering events to ultimately adjust the weight of collected photon packets. Additional scattering, biased or unbiased, can be applied once the photon undergoes a first biased scattering event. To ensure the forward scattering of some photons, photon splitting was applied such that photons, who never experienced bias-scattering, were split into two halves. One-half scattered in a biased manner towards the collecting fiber according to f_B with a likelihood of L and the other unbiased by continuing the forward propagation pursuant to f_{HG} with an assigned likelihood of $L' = 1 - L$. This last packet is considered to have never experienced bias-scattering in Fig. 3.2 and would thus split again at the next scattering event.

Optical configuration and tracking algorithm

Optical illumination and detection configurations were simulated using illumination and photon collection modules with identical properties of numerical aperture (NA), geometry, and spatial locations. Simulations of multiple A-lines were achieved by varying the lateral positions of the illumination and detection fibers. When the backscattered photon returned within the fiber's NA and radius, the photon was labeled as detected. The traveled distance of the photon packet in each different layer was tracked as opposed to the fluence absorbed by the sample. This strategy allowed us to adjust the phase of the signal for media with different refractive indices afterward. Upon photon detection, the cumulative traveled distance (total pathlength TP), weight W, and likelihood L of each photon were saved.

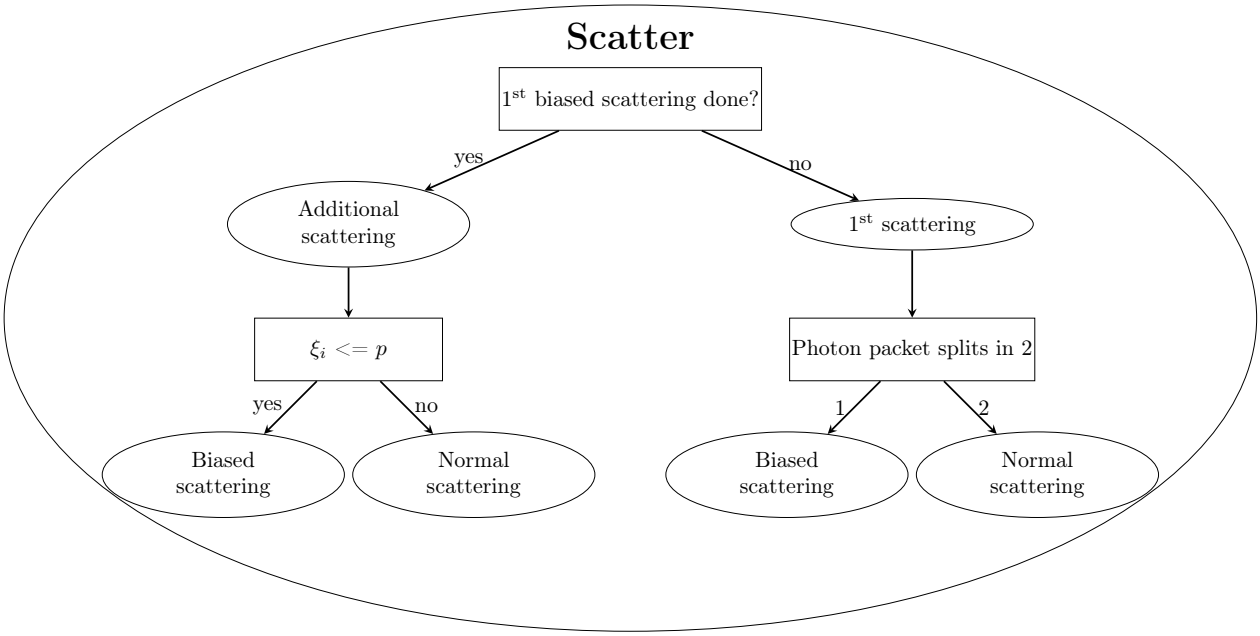

Figure 3.2 Flowchart describing the scattering process of the simulator. The randomly generated number is noted $\xi_i \in [0, 1]$ while p is the probability for biased versus unbiased scattering.

This method was implemented by modifying an existing open-source C-language software package that is available on the website of the Oregon Medical Laser Center [87]. The MCOCT photon tracking algorithm flowchart is shown in Fig. 3.3 and describes the steps of a standard MC simulation (gray background) as well as our methodological contributions (white background).

3.2.3 OCT signal reconstruction

For each A-line defined by a lateral (x) position of the illumination/detection fiber module, a number N of detected photons with their corresponding weight, likelihood, and total pathlength was acquired. These parameters were then used to reconstruct the OCT signal following a series of mathematical processes described in Fig. 3.4. To calculate the signal across the spectral bandwidth $\Delta\lambda$ at a central wavelength λ_0, a discrete k array corresponding to the mth wavenumber ($k_m = 2\pi n/\lambda_m$) was created with $\lambda_{\text{min}} = \lambda_0 - {}^{\Delta\lambda}/_{2}$ and $\lambda_{\text{max}} = \lambda_0 + {}^{\Delta\lambda}/_{2}$. The collected signal $S_S(k_m)$ from the sample was then reconstructed as a function of wavelength and for all j detected photon packets using this expression:

$$S_S(k_m) = \sum_{j=1}^{N} \sqrt{W_j L_j} \exp(-i \cdot k_m \cdot TP_j). \tag{3.6}$$

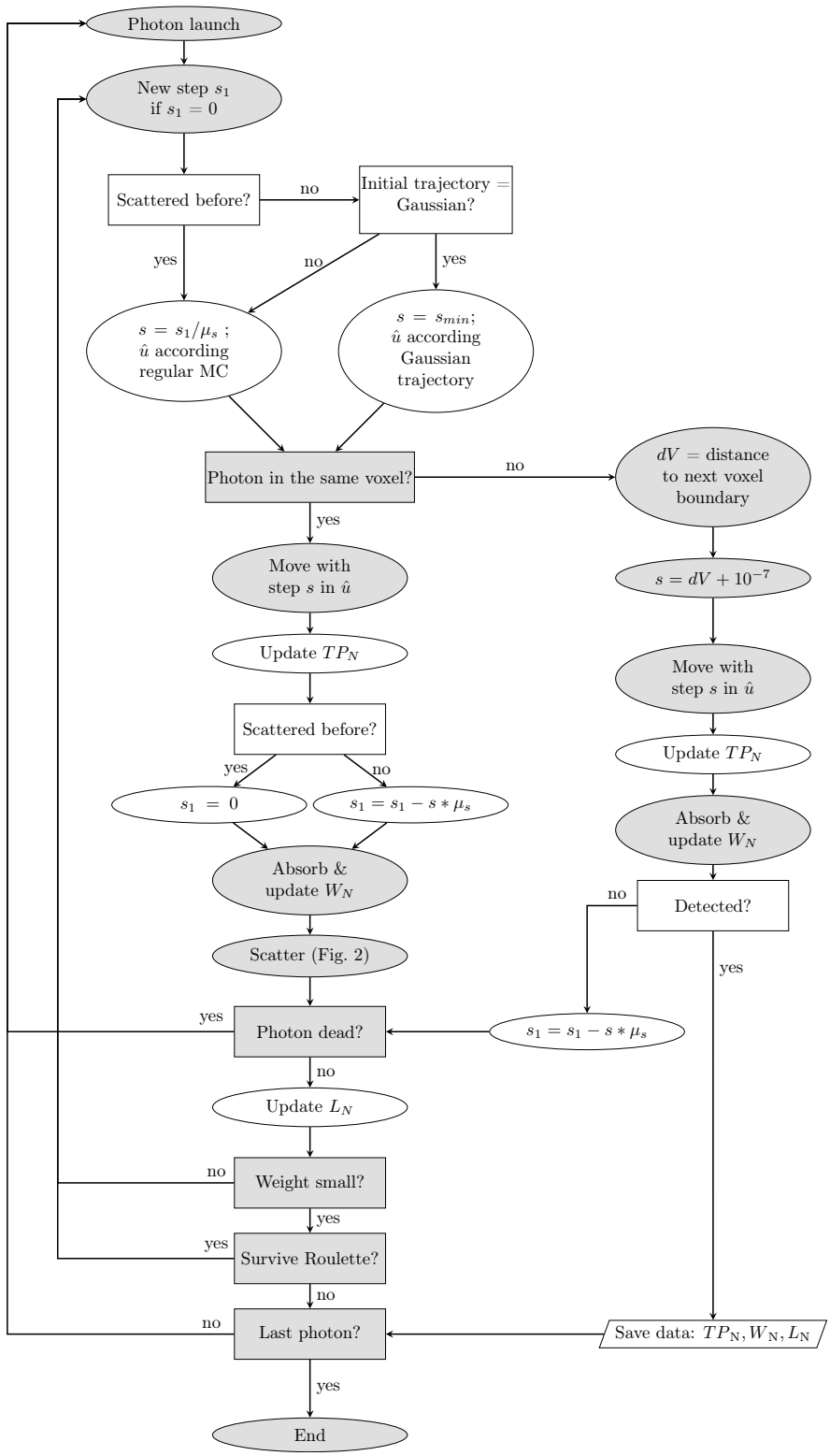

Figure 3.3 MCOCT Flowchart. Variables are described in Table 3.5 of the Appendix.

The reference arm signal amplitude $S_R(k_m)$ was calibrated as the average of the modulus $|\cdot|$ of the signal amplitude of the sample arm to ensure comparable power in both arms :

$$S_R(k_m) = \text{mean}(|S_S(k_m)|). \tag{3.7}$$

By emulating a balanced detection configuration, the signal at the detector was generated by interfering the sample arm signals $S_S(k_m)$ with the reference arm signals $S_R(k_m)$ and therefore creating the interference fringe signal $I(k_m)$ defined by

$$I(k_m) = |S_S(k_m) + S_R(k_m)|^2 - |S_S(k_m) - S_R(k_m)|^2. \tag{3.8}$$

Consequently, $I(k_m)$ was defined as a function of the wavelength and required further Fourier-domain processing to generate the OCT signal as a function of depth by applying a Hanning window, zero padding, and discrete Fourier transform. These processes were performed in Matlab (Version R2021a, Natick, MA, USA).

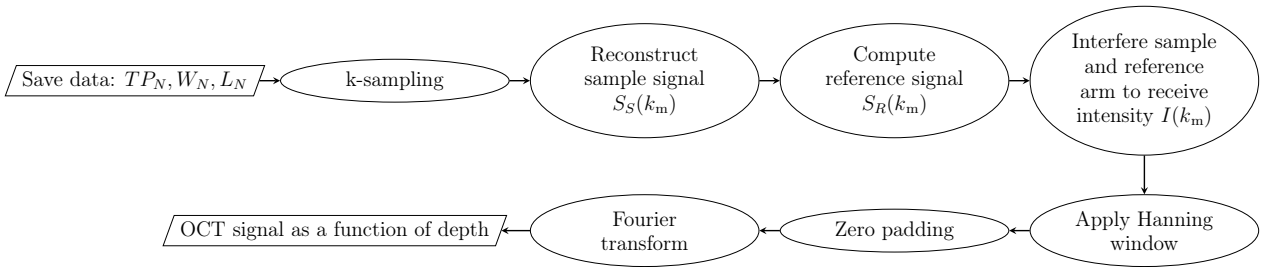

Figure 3.4 Optical coherence tomography (OCT) signal reconstruction. Definitions of variables: TP_N, total pathlength; W_N, weight; L_N, likelihood; N, N^{th} collected photon packets; k, wavelength; $S_S(k_m)$, signal amplitude from the sample arm; $S_R(k_m)$, signal amplitude from the reference arm; $I(k_m)$, reconstructed OCT signal.

3.2.4 Tissue-mimicking optical phantoms

Optical phantoms based on the optical properties of biological tissues were fabricated and characterized to validate this simulator.

Fabrication

To validate our simulator, optical phantoms mimicking biological tissue were developed with polydimethylsiloxane (PDMS) matrices. PDMS was selected for an accurate representation of the refractive index $n \sim 1.4$ of biological tissue [113]. The matrix demonstrates good

durability and is visible with the OCT system at a wavelength of 1310 nm. Nigrosine was utilized as the absorbing agent and titanium dioxide powder as the scattering agent to mimic biological tissue (see Table 3.1). Three one-layer phantoms and one bi-layer phantom were fabricated with different optical properties by varying quantities of nigrosine and titanium dioxide. The bottom layer of the bi-layer phantom was created using the same recipe as the one-layer phantom #3, wherefore the properties of these layers are assumed equal.

Optical properties characterization

The absorption coefficient μ_a and reduced scattering coefficient μ_s' defined as $\mu_s' = (1-g)\mu_s$ were determined for the one-layer phantoms. To acquire the transmission and reflection spectra, a LAMBDA 1050 spectrophotometer from PerkinElmer (Waltham, MA, USA) was used. This commercial device is equipped with a single integration sphere capable of receiving both diffuse and specular lights. The collected spectra were processed using the inverse adding-doubling method to estimate μ_a and μ_s' [114,115]. The determination of the anisotropy coefficient g was unattainable through direct measurement and was thus estimated by fitting OCT A-lines measured experimentally (see Sec. 3.2.4) to a theoretical model. In a first approximation, assuming a homogeneous turbid medium, the signal amplitude $I(z)$ at a depth z can be modeled as a single exponential decay function following a variant of the Beer-Lambert law [116–118]:

$$I(z) = I_0 \exp(-2(\mu_a + \mu_s) \cdot z), \tag{3.9}$$

where I_0 is the incident light intensity. The factor 2 in the exponential decay accounts for the round-trip photon propagation typical to OCT. Assuming a direct measurement of μ_a, the fitting procedure allowed to extract μ_s. Visual inspection of the fit was performed in the range of depths $z = [0.2, 0.5]$ mm, where $z = 0$ referred to the sample's surface. This range was selected to avoid the impact of Fresnel's reflection. This model is also called the single scattering model, which assumes that the detected backscattered light undergoes only one

Table 3.1 Quantities of the scattering (titanium dioxide) and absorbing (nigrosine) agents of the phantoms developed with polydimethylsiloxane (PDMS) matrices.

	Phantom #				
	1	2	3	4: top layer	4: bottom layer
Titanium dioxide [mg/g of PDMS]	8.5	3	1.5	6	1.5
Nigrosine [mg/g of PDMS]	25	25	25	25	25

scattering event in the sample. Measured optical properties are described in Table 3.2 and represent biological tissue for OCT imaging at 1310 nm [111, 119].

OCT imaging of phantoms

OCT imaging was performed with a VCSEL Fourier-domain system (Thorlabs, NJ, USA) at $\lambda_0 = 1310$ nm with $\Delta\lambda = 130$ nm. Two lenses of different focal lengths were used: a short one with $f = 30$ mm and a long one with $f = 75$ mm. The position of the focus inside each optical phantom z_f was determined separately for each focal lens and summarized in Table 3.3. For each experiment, OCT imaging generated 300 A-lines which were averaged for comparison with MCOCT.

3.2.5 MCOCT simulations for comparison with MCX simulations

To validate the beam focusing performance, the flux output (optical fluence rate) generated by MCOCT was compared to the one from MCX [92]. The accumulated energy was stored within the 3D voxel matrix during the simulation. The 3D matrix with the deposited weight was normalized relative to the input power, resulting in the local absorption rate per watt (W) of the incident light in units of $\mathrm{W/cm^3/W_{incident}}$. Dividing this rate by the absorption coefficients of the corresponding voxels resulted in the local fluence rate Φ in $\mathrm{W/cm^2/W_{incident}}$. The tissue was represented in both simulators by a $200 \times 200 \times 300$ voxel geometry with isotropic voxels of 0.001 $\mathrm{cm^3}$. The distance between the imaging lens and tissue surface $z_{f,I}$ was set at 0.85 cm with a beam width at imaging lens $D = 0.1$ cm. In MCOCT, the illumination beam had a Gaussian profile at the imaging lens. In MCX, the trajectory was simulated as a hyperboloid of one sheet and the photon packets propagated in straight lines along the double-ruled surface, thereby mimicking a Gaussian-distributed photon launch [92]. For both simulations, optical properties were $\mu_a = 0.001$ $\mathrm{cm^{-1}}$, $\mu_s = 0.01$ $\mathrm{cm^{-1}}$, $n = 1$, and $g = 0.5$.

Table 3.2 Optical properties of the phantoms characterized by spectrophotometry: μ_a, absorption coefficient; μ_s', reduced scattering coefficient; n, refractive index; g anisotropy coefficient.

Phantom #	Geometry	μ_a [$\mathrm{cm^{-1}}$]	μ_s' [$\mathrm{cm^{-1}}$]	n	g
1	one-layer	0.0922	16.79	1.4303	0.7
2	one-layer	0.147	6.58	1.4240	0.8
3	one-layer	0.118	2.55	1.4409	0.9
4	top layer of bi-layer	0.0912	13.23	1.3844	0.5
	bottom layer of bi-layer	0.118	2.55	1.4409	0.9

Table 3.3 Position of focus z_f [mm] below the phantom surface for each focal lens f.

Focal length f [mm]	Phantom #			
	1	2	3	4
$f = 30$	0.618	0.552	0.602	0.9
$f = 75$	1	1.16	1.14	0.9

MCOCT and MCX simulations were executed using 10^6 photon packets and were run on a desktop computer equipped with an Intel(R) Xeon(R) E5 CPU at 3.50GHz, 16GB RAM and an NVIDIA TITAN Xp card.

3.2.6 MCOCT simulations for comparison with OCT imaging in phantoms

Optical properties from Table 3.2 were used to generate OCT A-lines with MCOCT. Importance sampling was incorporated with a bias coefficient of $a = 0.9$ and an additional bias probability of $p = 0.8$, as defined in [98, 108]. A minimum step $s_{\text{min}} = 10^{-4}$ cm was used for these simulations. A scheme of 1000 equidistant illumination and detector pairs along the x-axis from $x = -1$ cm to $x = 1$ cm was used and resulted in simulating 1000 A-lines for a single B-scan. To minimize simulation time, a one-voxel slab of $2 \times 2 \times 0.5$ cm^3 was used to model the one-layer phantoms. For comparison with the bi-layer phantom, the medium was modeled as a two-voxel slab of $2 \times 2 \times 1.8$ cm^3. For all simulations, the incident light beam diameter at the focusing lens D was set to 0.07 cm for imaging at $\lambda_0 = 1310$ nm. For OCT signal reconstruction, $\lambda_{\text{min}} = 1245$ nm and $\lambda_{\text{max}} = 1375$ nm. Optical properties were approximated to be constant over the OCT reconstruction spectrum. All simulations were executed using between 10^8 and 10^9 photon packets and were ran on the same desktop computer as above. Simulated A-lines are further averaged among detectors (1000) to reduce speckle contrast.

3.3 Results

Figure 3.5 (a) and (b) show the optical fluence rates Φ at $y = 0$ mm generated by MCOCT and MCX, respectively. In both simulations, the beam appears curved as expected for a Gaussian distribution. The simulation time was 60 seconds for MCOCT and one second using MCX. Figure 3.5 (c) shows a very good agreement between optical fluence rates simulated along the x-axis at the depth of the beam focus ($z = 1.5$ mm) by MCOCT (red) and MCX (blue). Figure 3.5 (d) presents the optical fluence rates simulated along the z-axis at a fixed x-position ($x = 0$ mm) by MCOCT (red) and MCX (blue). Both curves progress similarly

around the beam waist but show more discrepancies with distance including a fastest decrease for MCX compared to MCOCT.

Figures 3.6 and Fig. 3.7 show the comparison between A-lines generated by MCOCT (blue) and those measured in the 4 experimental phantoms (red) using an imaging lens with a focal length of $f = 30$ mm and $f = 75$ mm, respectively. At $f = 30$ mm, the attenuation of the MCOCT A-line follows a similar pattern to experimental data in the one-layer phantoms except in a region close to the surface of the sample where the signal intensity is lower in experimental data. In the bi-layer phantom (phantom #4, (d)), the change of optical properties from the superficial layer to the deep layer is marked by a transient change in signal intensity at a depth corresponding to the interface between layers (0.9 mm). A change in the attenuation slope is also observed with the change of optical properties between layers. For all comparisons, the accuracy of the simulated data also decreased with increasing depth as a result of lower signal intensity due to fewer collected photons. At $f = 75$ mm, signal intensity patterns were similar to that of $f = 30$ mm while signal intensity close to the surface presented a more accurate qualitative match. For both focal lengths, A-lines obtained by simulating a pencil beam and a geometric focused beam differed significantly from the A-line simulated with the Gaussian beam as well as from experimental OCT signals acquired in Phantom #1 (see Fig. 3.8 in Appendix).

Table 3.4 reports computation times for generating a B-scan of the phantoms presented in Fig. 3.6 and Fig. 3.7 along with the quantity of simulated and detected photons. Detected photons varied between 1.5×10^5 to 2.9×10^6 for a number of photons launched varying between 10^8 to 10^9, yielding a ratio of detected/launched between 0.0525 and 0.33%.

3.4 Discussion

In this work, an OCT simulator (MCOCT) based on Monte Carlo methods was implemented and validated. The simulator was based on a Gaussian illumination profile and the importance sampling method as well as signal reconstruction in the Fourier domain. The numerical

Table 3.4 Computation time and quantity of launched and detected photons for MCOCT simulations presented in Fig. 3.6 and Fig. 3.7.

	Figure							
	3.6a	3.6b	3.6c	3.6d	3.7a	3.7b	3.7c	3.7d
Photons launched	10^9	10^9	10^9	10^8	10^8	10^8	10^8	4×10^8
Photons detected	1.5×10^6	2.2×10^6	2.5×10^6	2.9×10^5	1.5×10^5	2.2×10^5	3.3×10^5	2.1×10^5
Total time (hours)	31.5	30.8	33.3	1.5	3	3	3.3	6.7

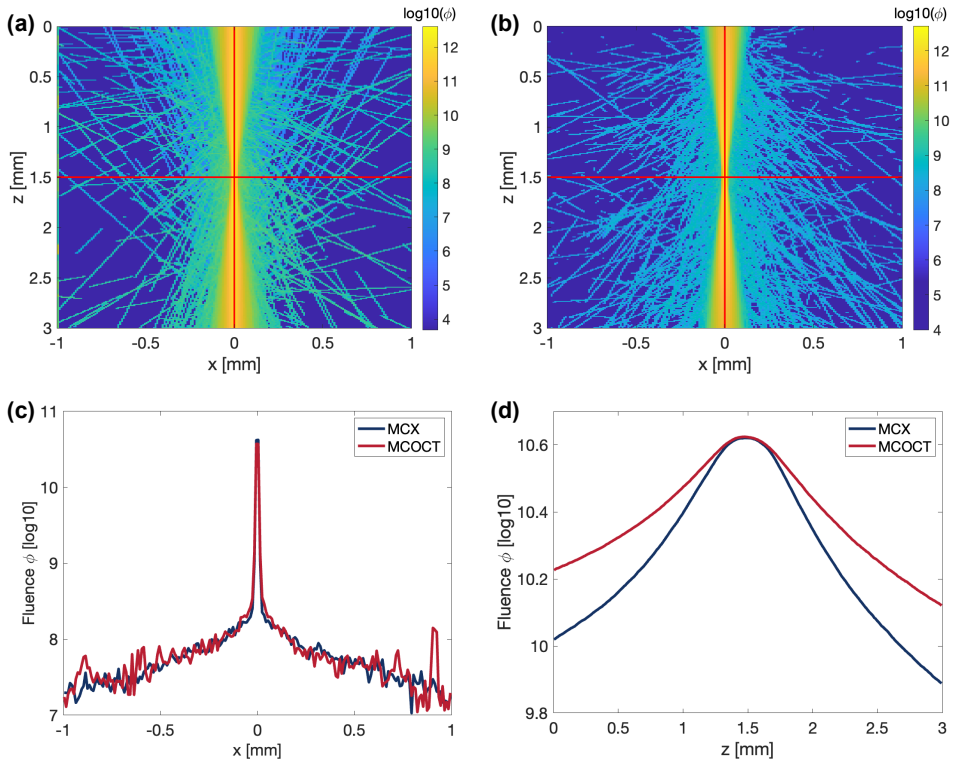

Figure 3.5 Optical fluence rates ϕ [W/cm^2/W$_{\text{incident}}$] comparison between (a) MCOCT and (b) MCX simulated with the same optical properties. (c) Comparison of optical fluence rates along x at $z = 1.5$ mm and $y = 0$ mm generated by MCOCT (red) and MCX (blue). (d) Comparison of optical fluence rates along z at $x = 0$ mm and $y = 0$ mm simulated with MCOCT (red) and MCX (blue).

comparison with MCX [92] and experimental comparisons with OCT imaging in phantoms with known optical properties allowed us to assess and validate the performance of MCOCT. This work proposes an experimental validation of an MC package for OCT combining bias scattering, detection with various NAs, phase extraction from the photon's traveled distance, and Gaussian beam focusing.

In OCT systems, the high lateral resolution is achieved through tight focusing of the probing beam, which can be performed by the implementation of a Gaussian focusing profile. A method considering the wave nature of photons was developed by focusing the light along the curved trajectories in accordance with Gaussian optics to a diffraction-limited focal spot. In the simulation, a low scattering coefficient was selected to better visualize the curved Gaussian trajectory of photons. When compared to MCX hyperboloid [92], the diffraction-limited spot size at the focus w_{0,n_2} matched well. Optical fluence rates from the two simulators showed an overlap in progression around the beam waist. With distance to the beam waist,

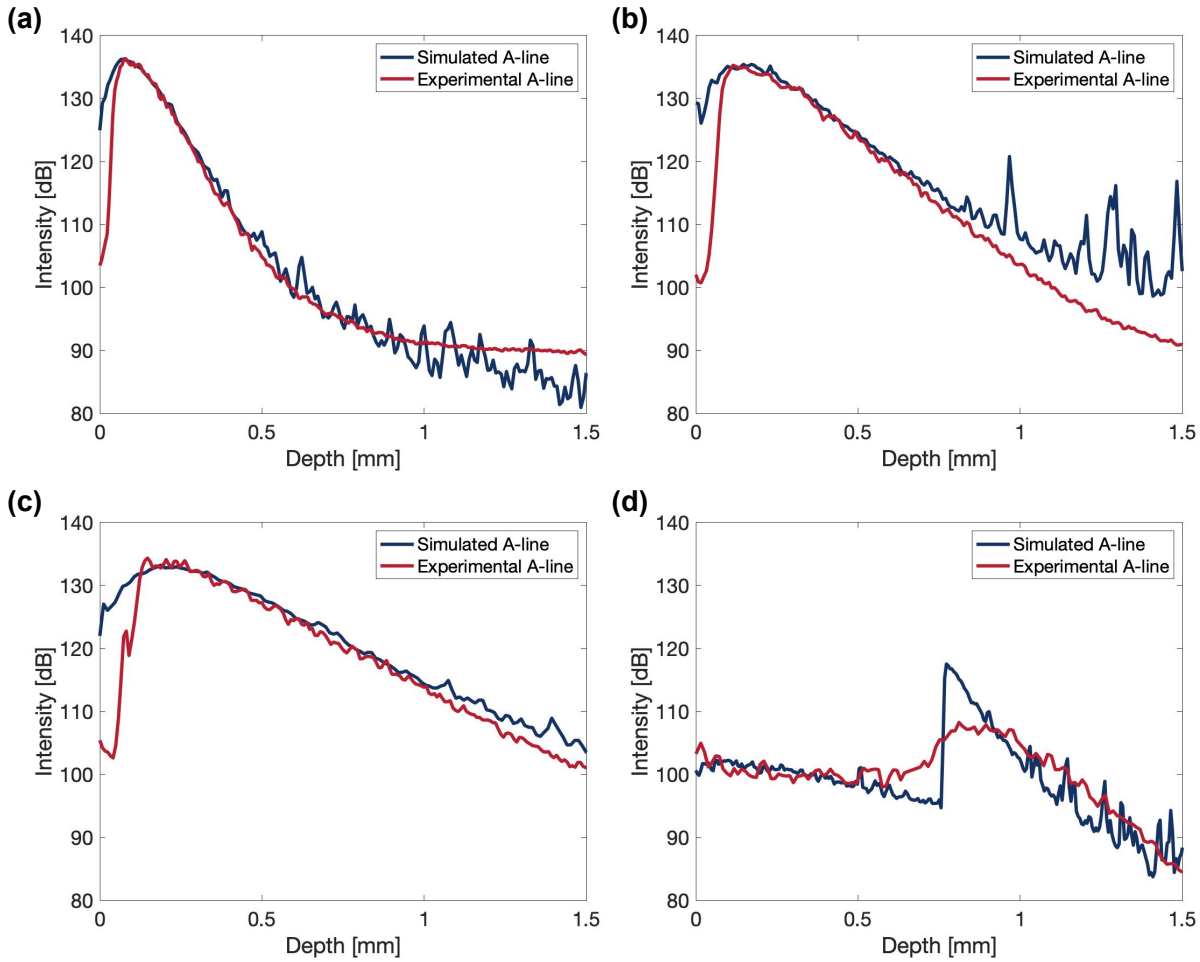

Figure 3.6 Experimentally obtained (red) *vs.* simulated (blue) OCT A-lines using an imaging lens of $f = 30$ mm of (a) Phantom #1, (b) Phantom #2, (c) Phantom #3, and (d) Phantom #4.

the fluence rates varied, which may be due to the different approaches used for mimicking the Gaussian photon trajectory (hyperboloid *vs.* Gaussian optics). The fluence generated by MCOCT was similarly higher at the surface of the medium ($z = 0$ mm) and in-depth ($z = 3$ mm) compared to MCX. Using the importance sampling method in MCOCT reduced the number of photons that scattered in the forward direction, which also includes photons that should have exited the bottom boundary of the medium but were biased back to the surface. While this number is reduced for MCOCT, the fluence was corrected by the biased likelihood ratio and therefore does not explain the higher fluences observed with distance from the beam waist. If the likelihood ratios were not corrected for the biased scattering, the disparity between fluences calculated by MCOCT and MCX at the sample's surface would be

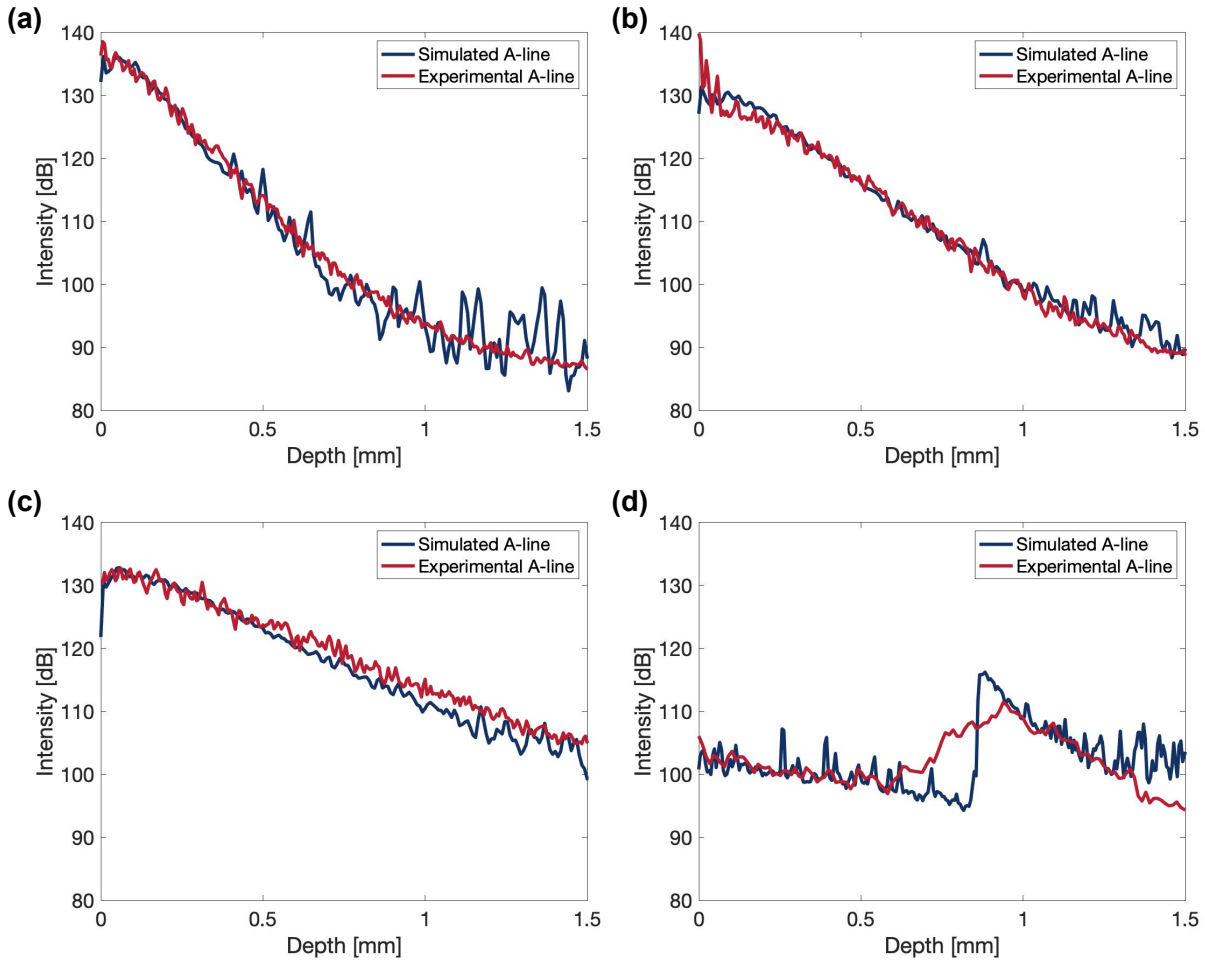

Figure 3.7 Experimentally obtained (red) *vs.* simulated (blue) OCT A-lines using an imaging lens of $f = 75$ mm of (a) Phantom #1, (b) Phantom #2, (c) Phantom #3, and (d) Phantom #4.

different from that of the bottom. When focusing the light in MCOCT, the photon packet propagated by minimal steps allowing us to track the voxel in which the photon packet was located more accurately and adapt the direction in case of changing optical properties. This strategy allowed us to bypass the need to solve an equation of motion previously proposed [104, 112]. Then, only $s_{\min}$ needs to be adapted and mainly depends on the voxel geometry. In MCOCT, the importance sampling method was used to increase the occurrence of backscattering, thereby reducing computational costs for OCT signal simulation, while in MCX all photons scattered according to the HG function. The difference in computation time between the two tools is mainly due to the computational architecture as MCX uses GPU resources while MCOCT uses CPU resources. The performance of the Gaussian illu-

mination was also clear when comparing it with simulations performed with a pencil beam and a geometric focused beam.

When compared with OCT A-lines acquired in phantoms using a short focal length (30 mm), A-lines reconstructed by MCOCT differed within the first ∼0.2 mm. This pattern was not observed at a longer focus (75 mm), where MCOCT matched OCT imaging in the four phantoms. This discrepancy is likely due to the reflection of light at the phantom surface, which is not considered in the simulator. When the surface has slight tilts, the coupling of reflected light with the incident light is higher for shorter focal lengths, leading to enhanced distortions in the A-line at the surface. It is also possible that a more accurate detection scheme [104] and scattering function [100,103] would provide a better match between MCOCT and experimental A-lines. The decrease in OCT signals with increasing penetration depth is expected as the probability of photon absorption also increases with greater propagation. A gradual deviation between A-lines generated by MCOCT and phantoms imaging occurred beyond a depth of about 1 to 1.5 mm. This difference is likely due to the fact that fewer photons reached these depths and were detected. The deviation was more prominent in one-layer phantoms imaged at the focal length of 30 mm compared to 75 mm. The reason behind this is unclear to us at present and is a current limitation of the simulator. For OCT applications in biological tissue, this limitation may not be a significant concern as typical OCT systems are designed to provide an imaging depth of approximately 1.5 mm [80].

The accurate characterization of signal intensity at interfaces is challenging when modeling complex geometry with multiple layers. When the change in refractive index occurs at the interface of two layers, photons undergo either reflection or refraction, which are mathematically described by Fresnel's equation [80]. MCOCT signal intensity simulated proximal to the interface of the two layers in the bi-layer phantom did not match the one from OCT imaging at either focal lengths. Fresnel reflection was not implemented in MCOCT and this discrepancy may be mitigated by considering such reflections as in previous works [104].

Minimizing computational costs is challenging when considering complex media with optical properties mimicking biological tissue. The computation time was higher for phantoms with higher scattering coefficients as these simulations presented more scattering events. For example, generating the OCT signal with the same quantity of detected photons for phantom #1 required higher computational resources than for phantom #3 as scattering was ∼6 times higher (see Table 3.4). Also, the quantity of photon packets launched when initiating the simulation dictates the computation time as well as the ratio of detected photons (0.0525 to 0.33%) that contributed to the OCT signal. As expected, simulations that used 10^9 photon packets (one-layer phantoms at $f = 30$ mm) were ∼10 times longer than simulations that launched 10^8 photon packets (one-layer phantoms at $f = 75$ mm). For the bi-layer phantom,

a similar pattern was observed as the simulation using 4×10^8 photon packets (at $f = 75$ mm) took ~4 times longer than one using 10^8 photon packets (at $f = 30$ mm).

In addition to the computational efficiency of the MC process, the number of voxels included in the geometry also affected the computational time of MCOCT. Each time a photon packet propagates by the distance prescribed by $s_{\min}$, MCOCT estimates its distance to the voxel boundary, which represents several occurrences when considering a geometry with a high number of voxels. This step is essential for geometry designed with multiple layers as optical properties have to be modified when propagating through different tissues. The voxel size also dictates the spatial resolution of the optical fluence rates. A strategy to minimize the number of crossing-boundary events is to use one voxel for each layer with the voxel size in the axial direction being equal to the layer thickness. This simple design can be used for simpler geometry such as rectangular slabs but is less appropriate for complex media. The axial resolution of the simulated OCT data is achieved through the imaging spectrum, whereas the quantity of simulated source/detector positions dictates the lateral resolution of the B-scan. The use of large voxels for simple geometry did not affect the lateral resolution of the OCT image. Another factor that influenced the computation time was the minimal step used to generate the Gaussian focusing beam. The selection of a short minimal step will increase the accuracy of individual photon trajectories but also increase the occurrences with which the trajectory has to be updated. Previous methods have been proposed to automatically adjust the step size during the simulation [112]. In MCOCT, an adjustable step could be implemented but it is not clear how it would reduce computation time while maintaining high accuracy. Another time-consuming procedure in the Monte Carlo module was the random number generation that is needed for each scattering event. Generating one random number each time could be substituted with an *a priori* array of random numbers generated prior to the simulation.

Our work has several limitations. MCOCT simulations were run on a single CPU thread, which limited speed compared to GPU-based simulators [92, 100, 102, 103]. Accelerating methods such as parallel computing by Compute Unified Device Architecture (CUDA) will be explored for future versions of MCOCT. Using this architecture would also allow performing the initialization, simulation running, postprocessing, and visualization entirely in Matlab. Therefore, users would not need a separate UNIX-emulating console shell to run a compiler and the MC executable, nor would there be a need for intermediate input/output files, which additionally would save storage space. Parallelization would allow simulating a higher quantity of photon packets leading to higher accuracy of the OCT signals at higher sample depths. Noise and/or dispersion were not added to MCOCT signals before reconstruction, but could be added to the reconstructed OCT signal in future works. MCOCT

used a scheme of 1000 illumination and detectors along the x-axis to generate a B-scan image. Since the geometry is described using a 3D voxel system, it is also possible to simulate a scan over the y-axis to reconstruct 3D volumes. However, a 3D scan would currently result in a significant increase in computation time. The demonstration of the ability to generate 3D volumes would be more relevant with a code based on parallelization using GPU.

Monte Carlo methods are the gold standard for studying photon propagation in turbid media [81, 86, 120] and have been instrumental in investigating the relationship between tissue optical properties and imaging results for several techniques including FD-OCT [100,121]. An accurate analytical/numerical modeling of FD-OCT imaging is critical to study light-tissue interactions, including speckle contrast [122, 123], dispersion [124, 125], and multiple scattering [126, 127]. A better understanding of these optical phenomena via accurate simulations may help to design an instrument, optimize data acquisition specs and image reconstruction parameters. Numerical and *in vitro* experiments are often used to produce preliminary results that can guide the development of an *in vivo* experimental protocol to answer a scientific question.

While further enhancements remain necessary, our open-source simulator can be employed for model validation and system optimization by generating OCT signals across a wavelength spectrum to ascertain the appropriate NA to achieve the desired contrast and its observable depth. Simulating the impact of varying NA or different modes of a photonic lantern [128] can determine the feasibility of achieving a substantial contrast. Our tool can also contribute to the planning of *in vivo* experiments to provide preliminary estimates of specific biomarkers such as changes in retinal layer thickness to characterize particular physiological/pathological conditions [12]. Previous applications [84, 93–99, 101, 102, 104, 105] and more recent ones involve the generation of OCT image datasets that can be used in the training of neural networks aimed at tackling the inverse problem in OCT. Some groups already proposed Monte Carlo simulation platforms to generate realistic OCT images for predictive model training [106, 107].

3.5 Conclusion

In this work, a novel Monte Carlo simulator for Fourier-domain OCT (MCOCT) was introduced. The incorporation of a Gaussian light illumination scheme and the ability to increase backscattered event collection allowed us to achieve a more realistic approach to OCT imaging. Optical fluence rates generated by MCOCT were compared with an established MC simulator (MCX), which provided a numerical validation. OCT signals generated by MCOCT were also compared to OCT signals acquired at specific focal lengths in tissue-mimicking

phantoms with known optical properties, which provided experimental validation. Future work involves leveraging GPU acceleration for enhanced computational efficiency and speed, as well as considering Fresnel reflections proximal to interfaces in multi-layered geometries. MCOCT may further allow the designing of OCT system hardware and image processing for various medical and biomedical applications.

Funding

This work was supported by the Natural Sciences and Engineering Research Council of Canada (NSERC) grants #RGPIN-2018-06151 (to C.B.), #RGPIN-2015-04672 and #RTI-2016-00636 (to M.D.) as well as the German Academic Exchange Service (DAAD, to K.E.).

Acknowledgements

Portions of this work were presented at the SPIE BIOS conference in 2021,116400G in an oral presentation and as a poster at the Optica Biophotonics Congress: Optics in the Life Sciences in 2023,JTu4B–29 [129, 130].

Disclosures

The authors declare no conflicts of interest.

Data Availability

The source code for MCOCT will be available on GitHub upon publication of the manuscript. Raw data used in this work are available upon appropriate request.

Appendix

Table 3.5 Variables used to describe Fig. 3.1 and Fig. 3.3

Tissue optical properties		OCT signal reconstruction	
n	refractive index of tissue	k	wavenumber
μ_a	absorption coefficient	$S_S(k)$	sample signal
μ_s	scattering coefficient	$S_R(k)$	reference signal
g	anisotopy coefficient	$I(k)$	interference signal
Scattering		**Illustration**	
θ_S	scattering angle	λ	wavelength
θ_B	scattering angle	f	focal length
f_{HG}	Henyey-Greenstein function	z_f	distance between tissue surface and focus in medium
f_B	bias function	$z_{f,I}$	distance between tissue surface and imaging lens
L	likelihood value	$z_{f,L}$	distance between focus in medium and photon position
p	probability value	D	beam width at imaging lens
ξ_i	random generated number [0,1]	w_s	beam width at tissue surface
Flowchart		w_{0,n_2}	beam waist in medium
s_1	propagating distance	$w_{n_2}(z)$	beam waist in medium at position z
s	step size of photon packet	z_{R,n_2}	Rayleigh range in medium
$s_{\min}$	predefined step size	$R_{n_2}(z)$	radius of curvature at position z
dV	distance to voxel	θ_{n_1}	half divergence angle in medium of n_1
N	number of collected photon packets	θ_{n_2}	half divergence angle in medium of n_2
TP_N	total pathlength	$\hat{u}$	direction unit vector
W_N	weight	x, y, z	x, y, z position of photon
L_N	likelihood	n_1	refractive index of first layer
		n_2	refractive index of second layer

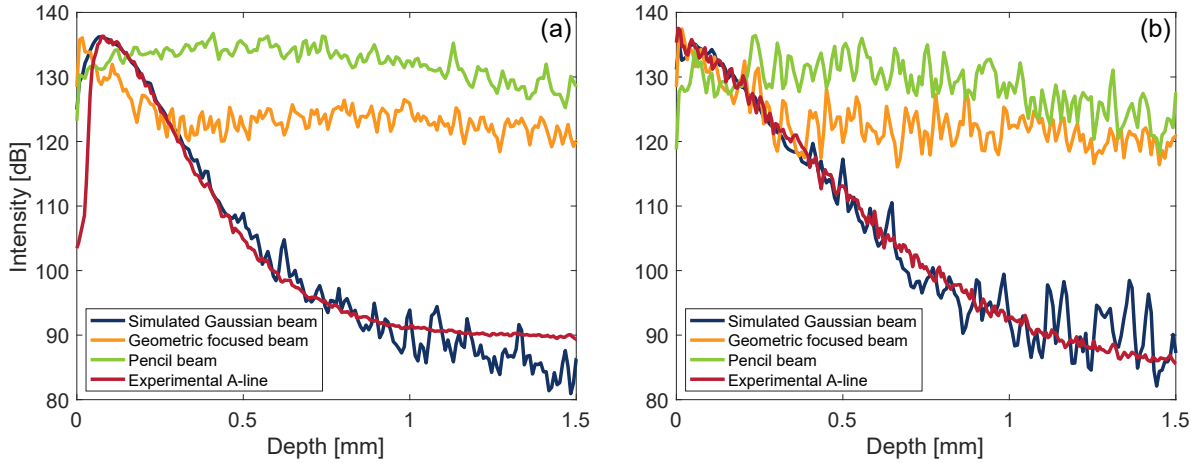

Figure 3.8 Experimentally obtained (red) *vs.* simulated using a Gaussian beam (blue) *vs.* geometric focused (orange) *vs.* pencil (green) beam OCT A-lines using an imaging lens of with the focal length $f = 30$ in (a) and $f = 75$ in (b) of phantom 1.

CHAPTER 4 ARTICLE 2 - SPECKLE CONTRAST REDUCTION THROUGH THE USE OF A MODALLY-SPECIFIC PHOTONIC LANTERN FOR OPTICAL COHERENCE TOMOGRAPHY

This article investigates the advantages and limitations of combining signal intensities from different channels in FM-OCT. It introduces a novel approach for reducing speckle contrast, effectively minimizing speckle noise with negligible impact on resolution—an improvement over existing techniques. Unlike other methods, this technique does not risk obscuring speckle-sized anatomical structures; rather, it helps to accentuate them. The effectiveness of the method is demonstrated through acquired images and quantified using a speckle contrast metric. Theoretical analysis further demonstrates that incorporating additional channels leads to further reductions in speckle contrast. The positive effect on SNR is also evaluated and demonstrated. The article also addresses additional noise introduced by back reflections from the MSPL tip and discusses strategies to mitigate it. This method is a novel means of enhancing image quality with minimal impact on resolution and can be integrated with existing techniques for further noise reduction.

Contribution: The lead author, Raphaël Maltais-Tariant, contributed approximately 90% of the work, including literature review, system assembly, software development, experimental protocol design, data acquisition and analysis, and manuscript preparation. Rodrigo Itzamna Becerra-Deana and Simon Brais-Brunet provided valuable input and contributed to manuscript revision. Prof. Mathieu Dehaes, PhD, and Prof. Caroline Boudoux, Pr. Eng., PhD, served as principal investigators, offering guidance throughout the project and assisting with article revision.

Authors: Raphaël Maltais-Tariant, Rodrigo Itzamna Becerra-Deana, Simon Brais-Brunet, Mathieu Dehaes, and Caroline Boudoux.

Abstract: A few-mode optical coherence tomography (FM-OCT) system was developed around a 2×1 modally-specific photonic lantern (MSPL) centered at 1310 nm. The MSPL allowed FM-OCT to acquire two coregistered images with uncorrelated speckle patterns generated by their specific coherent spread function. Here, we showed that averaging such images *in vitro* and *in vivo* reduced the speckle contrast by up to 28% and increased signal-to-noise ratio (SNR) by up to 48% with negligible impact on image spatial resolution. This method is compatible with other speckle reduction techniques to further improve OCT image quality.

Article published: Biomedical Optics Express, November 2023

DOI: 10.1364/BOE.504861

Submitted: September 06, 2023

4.1 Introduction

Optical coherence tomography (OCT) is a coherent imaging technique with a spatial resolution of ∼10 µm and an imaging penetration depth of ∼2 mm [18]. Due to its coherent light detection scheme, OCT suffers from speckle patterns that can mask tissue structures [131–133]. Several techniques have been previously proposed to reduce speckle noise [21–52]. These techniques however either compromised image spatial resolution [21–34], required multiple illumination and detection angles for limited improvement [35–39] or can blur intrinsic speckle-size structures of the image by removing speckles [40–50]. Neural network methods in OCT are emerging and can also be used to reduce speckle noise [51, 52]. While these methods are performant, they are limited by the need for available training datasets and may blur intrinsic structures as previously described.

Few-mode OCT (FM-OCT) is an all-fibered version of bright and dark field (BRAD) OCT [15]. In FM-OCT, the few-mode tip of a modally-specific photonic lantern (MSPL) [14, 16, 17] is coupled to an OCT imaging head allowing the collection of both the fiber fundamental mode (*i.e.* the linearly polarized (LP) mode LP01) and the first higher-order mode LP11. The MSPL then demultiplexes the two modes into two single-mode fibers connected to independent OCT systems [17]. Illumination is otherwise performed through the fundamental mode. This approach allows FM-OCT to create two OCT images (or a composite one) from the backscattered light coupled into LP01 and LP11, respectively.

Here, we demonstrate how the two distinct OCT images create specific speckle patterns that can further be averaged to reduce the speckle contrast while increasing the signal-to-noise ratio (SNR) with minimal impact on the image's lateral resolution.

4.2 Material and Methods

4.2.1 Instrumentation

The FM-OCT system used for data acquisition is illustrated in Fig. 4.1 (a) and is similar to the one used in our previous work [17]. The custom-built MSPL used to separate the modes was centered at 1310 nm. A wavelength-swept laser (Thorlabs SL1310V1, USA) and two balanced detectors (Thorlabs PDB430C, USA) were used for illumination and detection, respectively. The system allowed for simultaneous measurement of both MSPL channels (*i.e.*

LP01 and LP11 modes). The MSPL was further replaced by a single-mode fiber (SMF) for comparing the performance of the FM-OCT with a conventional OCT setup. The collimator was changed to compensate for the difference in numerical aperture (NA) between MSPL and SMF and to obtain the same collimated beam diameter, resulting in a system NA of ∼0.05 after the imaging lens (Thorlabs LSM02, USA). The resulting theoretical coherent spread functions (CSF) [19, 134] in each channel are illustrated in Fig. 4.1 (b) and (c). For the CSF in the LP11 mode, the negative response (in blue) was due to a π rotation of the detected phase signals. The symmetry and anti-symmetry between Channel 1 (LP01) and Channel 2 (LP11) allow to generate uncorrelated speckle patterns. This characteristic is key to reducing speckle contrast after averaging.

4.2.2 Imaging metrics

Following previous studies [20, 21], speckle contrast (C_s) was defined as :

$$C_s = \frac{\sigma_s}{\langle I_s \rangle}, \tag{4.1}$$

where σ_s and $\langle I_s \rangle$ are, respectively, the standard deviation and the average of the OCT speckle signal intensity in the absence of noise. More specifically, the OCT signal intensity is defined as the absolute values of the square of the complex signal of the field obtained by applying the Fourier transform [1]. Here, we define noise as the signal measured in the absence of a sample and is thus dominated by shot noise. Since noise is also uncorrelated between the two channels, it does not affect C_s. It was previously shown that for a fully developed OCT speckle contrast, $C_s = 1$ [20, 62]. For FM-OCT, theory informs that averaging two uncorrelated speckle intensity patterns allows to reduce speckle contrast such that [20]:

$$C_r = \frac{\sqrt{1+r^2}}{1+r} \qquad \text{with} \qquad r = \frac{\langle I_1 \rangle}{\langle I_2 \rangle}, \tag{4.2}$$

where $\langle I_1 \rangle$ and $\langle I_2 \rangle$ are the average OCT speckle intensities of Channels 1 and 2, respectively and C_r is the expected reduced speckle contrast. When considering $r = 1$, C_r is minimum and equals $1/\sqrt{2}$. In our work, the signal (I_a) averaged from signals measured in the two channels was calculated in linear scale as follows:

$$I_a = \frac{I_1}{\langle I_1 \rangle} + \frac{I_2}{\langle I_2 \rangle}. \tag{4.3}$$

Intensity averaging instead of complex field averaging is necessary to have a reduction in speckle contrast. When considering an FM-OCT system of N uncorrelated channels, the

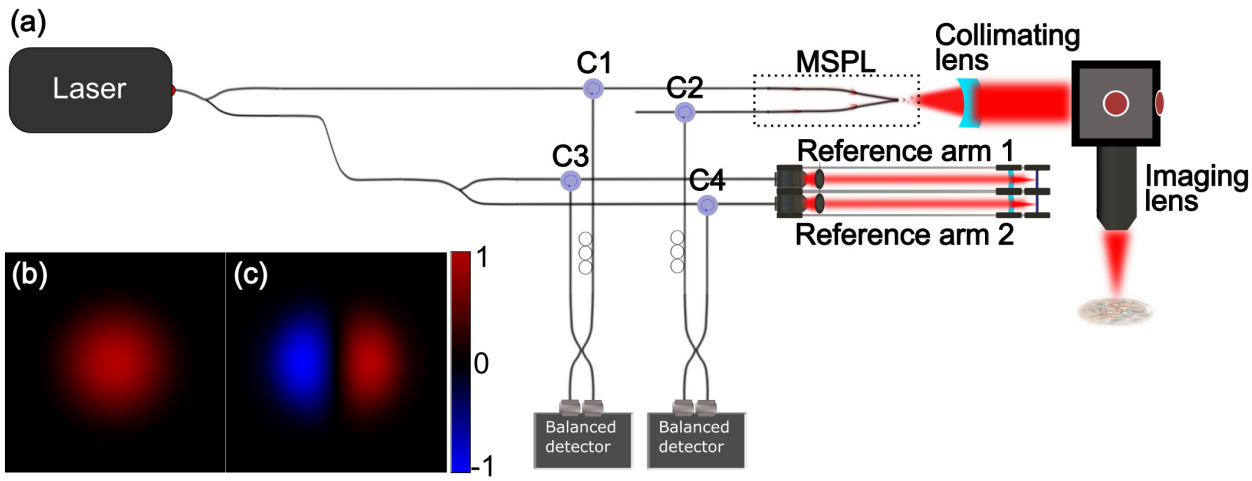

Figure 4.1 (a) Schematic of the few-mode optical coherence tomography (FM-OCT) system including the modally-specific photonic lantern, the illumination and detection components, and two reference arms; one for each mode. (b, c) Coherent spread functions of the LP01 and LP11 modes, respectively.

expected speckle contrast is given by $C_r = 1/\sqrt{N}$ [20]. To ensure that two speckle patterns are uncorrelated, their cross-correlation was calculated using the second-order correlation function [61, 62, 135]:

$$g^{(2)} = \frac{\langle I_1 \otimes I_2 \rangle}{\langle I_1 \rangle \langle I_2 \rangle}, \tag{4.4}$$

where $\langle I_1 \otimes I_2 \rangle$ is the ensemble average of the Hadamard product between I_1 and I_2.

Combining signals I_1 and I_2 also affects the SNR, which can be assessed with different approaches [1,21,136–138]. In this work, an approach considering the OCT signal intensity [137] was selected:

$$\mathrm{SNR} = \frac{\langle I_{\mathrm{OCT}} \rangle}{\sigma_{\mathrm{BN}}}, \tag{4.5}$$

where I_{OCT} is the OCT signal intensity measured from the sample while σ_{BN} is the standard deviation of the OCT signal intensity measured in the absence of a sample, *i.e.* the background noise. With this approach, σ_{BN} was dominated by shot noise, and not by speckle.

The maximum SNR of the system ($\mathrm{SNR}_{\mathrm{max}}$) was also assessed [136] for both the SMF and MSPL configurations. A mirror was used as a sample and placed at the focal plane to maximize the OCT signal. A tilted attenuator (Thorlabs NE40A, USA) was added to avoid saturating the balanced detector. One A-line was acquired to calculate $\mathrm{SNR}_{\mathrm{max}}$ using a

modified version of Eq. 4.5 to account for the presence of an attenuator:

$$\mathrm{SNR}_{\mathrm{max}} = \frac{\langle I_{\mathrm{OCT}} \rangle / R_m T^2}{\sigma_{\mathrm{BN}}}, \tag{4.6}$$

where T is the attenuation transmission that was measured experimentally using a power meter (Thorlabs S145C, USA) and R_m is the mirror power reflection coefficient, approximated as 1.

Furthermore, the retro-reflection power was measured using the same power meter by adding an extra circulator between the MSPL and circulator C1. To confirm the origin of the retro-reflection power, the reference arm length was adjusted to permit OCT imaging at the MSPL tip and determine where the retro-reflection occurred.

An A-line was acquired from the reflection of a mirror to assess the system axial resolution of all system configurations. The full width at half maximum (FWHM) was evaluated by fitting a Gaussian curve on the linear intensity signal of the mirror. The mirror was tilted to avoid the saturation of the balanced detectors. Dispersion was measured using an approach described previously [54].

To evaluate the lateral resolution, a C-scan of 840 by 920 A-lines (field-of-view of 1093 µm by 954 µm) of a negative reflective USAF-1951 resolution test chart was acquired. The resolution target was placed at the focal plane of the imaging lens by maximizing the OCT signal originating from the test chart layer. The resulting *en face* image (1 pixel thick) was displayed in dB scale. The edge response was also extracted from this image in dB scale and displayed on a normalized scale to facilitate the comparison between the different MSPL channels. The 10-90% edge response distances were calculated using the resolution chart measurement in the horizontal and vertical axes. Cubic spline interpolation was used to measure the signal transition more precisely. The edge response was not calculated for Channel 2 since its CSF does not have a Gaussian response [17]. The image spatial resolution was also assessed by measuring the smallest distinguishable USAF-1951 groups of elements (bars) in the vertical and horizontal directions. Measurements were performed for both SMF and MSPL configurations.

4.2.3 *In vitro* and *in vivo* imaging

The definition of speckle contrast from Eq. 4.1 considers that signal variability is explained only by the speckle effect. Experimentally, signal variation is caused by other processes, including, but not limited to, signal attenuation and sample heterogeneity. Because of this consideration, speckle contrast values are calculated locally, where speckle dominates signal

variability. For both *in vitro* and *in vivo* experiments, the region of interest (ROI) was subdivided in homogeneous subregion blocs of 4 by 4 pixels. C_s and SNR were calculated for each such subregion and then averaged. The metrics were calculated for the combined MSPL channel (I_a) as well as for individual MSPL Channels 1 (I_1) and 2 (I_2).

In vitro imaging was performed on a plastic cap engraved with the number "8" (Thorlabs, NJ, USA) and consisted of a C-scan composed of 840 by 920 A-lines (field-of-view of 8912 µm by 8137 µm). Speckle contrast and SNR were measured in an *en face* section within the cap (1 pixel thick) displayed in dB scale. The ROI for C_s and SNR calculations included the entire 840 by 920 *en face* image. The normalized second-order cross-correlation between Channel 1 and Channel 2 was evaluated to assess their intensity-intensity correlation.

In vivo imaging was further performed near the free edge of an index fingernail. It consisted in a single B-scan comprising 1000 A-lines. C_s and SNR were measured on a rectangular ROI of 40 pixels per 62 pixels.

4.3 Results and Discussion

Table 4.1 presents $\mathrm{SNR_{max}}$ and retro-reflection optical power measured for the SMF and MSPL optical configurations, respectively. Table 4.1 also shows the FWHM of the Gaussian fit of an OCT A-line of a mirror in intensity in linear scale. Compared to the SMF configuration, a 10-20 dB decrease in $\mathrm{SNR_{max}}$ is observed for the MSPL system. This decrease is due to increased retro-reflection power at the air-MSPL interface. Typically, fiber connectors for angled physical contact (FC/APC) are used in OCT as their tip is polished at an angle to minimize retro-reflections at the air-fiber interface. In its current configuration, the MSPL tip, however, has a minute diameter of 8 µm, which is too fragile for polishing. Cleaving the tip at a controlled angle is also challenging. An elegant solution involves splicing the MSPL tip to a few-mode fiber large enough to sustain polishing. It was successfully achieved by another group [56], albeit using equipment not currently available to our research group.

The $\mathrm{SNR_{max}}$ for Channel 2 is also significantly lower than that of Channel 1. This difference may be explained by the coupling model previously suggested by our group [17] where light reflected off a mirror was coupled back into LP11 with reduced efficiency. Indeed, if illumination was performed with LP11 instead of LP01, we expect a larger $\mathrm{SNR_{max}}$ for Channel 2. However, as the speckle reduction demonstration was performed under LP01 illumination, we present SNR data under the same experimental conditions. $\mathrm{SNR_{max}}$ was not measured when considering the combination of Channel 1 and Channel 2 since they reached a maximum SNR for their specific alignments [17]. Additionally, the power transmission of each optical

component from one channel to the other can vary, which affects SNR.

Table 4.1 Measurement of SNR_{max}, retro-reflection power and the full width at half maximum (FWHM) of an OCT A-line of a mirror in intensity in linear scale for the single-mode fiber (SMF) and modally-specific photonic lantern (MSPL) optical configurations.

Metrics	SMF	MSPL		
		Combined	Channel 1	Channel 2
SNR_{max} [dB]	111.2	–	98.2	91.1
Retro-reflection [µW]	0.02	–	77.8	35.5
FWHM [µm]	12.8	12.0	11.2	12.8

Fig 4.2(a) shows A-lines of a mirror comparing axial resolutions for the SMF and MSPL optical configurations. The normalized intensity is displayed in linear scale. The peaks were aligned and normalized for ease of comparison. In terms of FWHM (Table 4.1), Channel 1 shows a slightly higher resolution than the SMF configuration and Channel 2. This observation is likely due to the combined channels having a slightly better resolution than the SMF configuration but slightly worse than that of Channel 1. We believe these variations are due to physical compensations of the respective dispersion profiles. Fig. 4.2(b) indeed shows that Channel 1 exhibits less dispersion than Channel 2. Combining the two channels resulted in an average of the resolutions of Channel 1 and 2. The MSPL did not induce significant dispersion, nor did combining the channels deteriorate the axial resolution significantly.

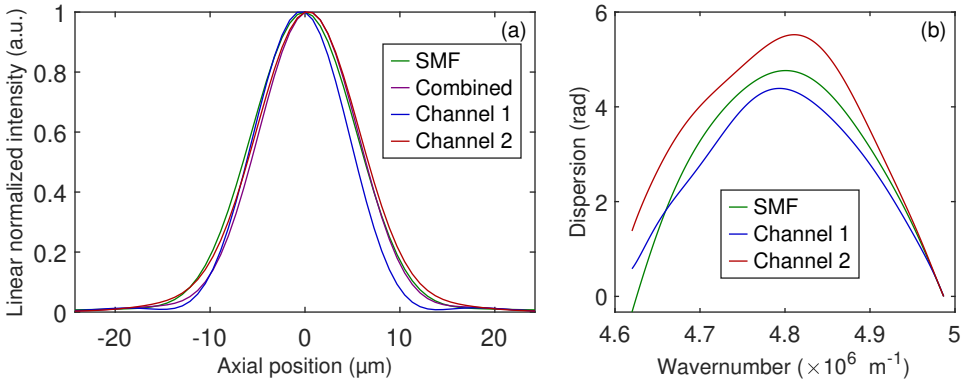

Figure 4.2 (a) Axial normalized intensity profiles (linear scale) of a mirror acquired by the single-mode fiber (SMF, green), combined modally-specific photonic lantern (MSPL) channels (purple), MSPL Channel 1 (blue), and MSPL Channel 2 (red). In (b), the associated dispersion curves (before digital compensation).

Fig. 4.3 shows *en-face* OCT images of a negative reflective USAF-1951 test chart (first row),

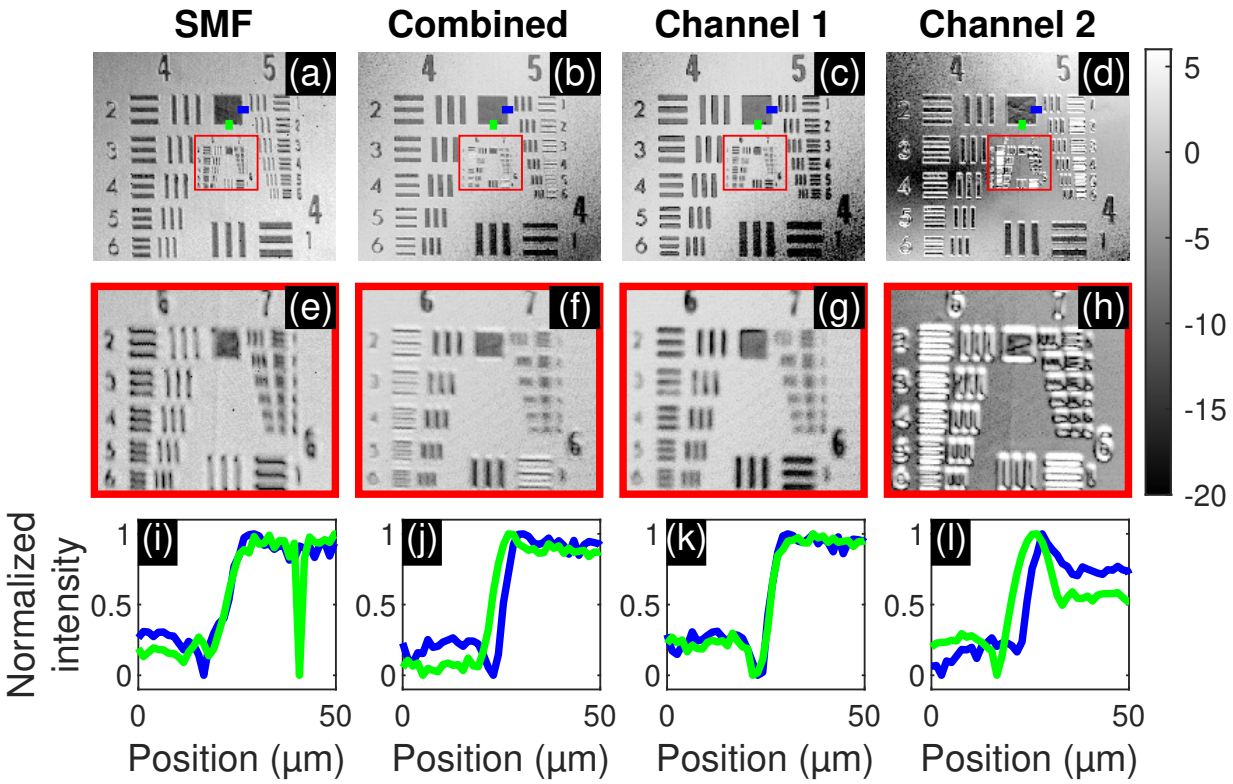

Figure 4.3 *En-face* OCT images of a negative reflective USAF-1951 resolution test chart (a–d) with a zoom-in of the region delimited by the red square (e–h) for the specific modes of collections: single-mode fiber (SMF), combined modally-specific photonic lantern (MSPL) channels, MSPL Channel 1, and MSPL Channel 2. The system's edge responses in dB (i–l) for the vertical (corresponding to signals normalized from the green region, first row) and horizontal (corresponding to signals normalized from the blue region, first row) axes. The fields of view of the first and second rows are 1093 µm by 954 µm and 283 µm by 247 µm, respectively.

zooms of the smaller groups (second row), and normalized intensity signals (third row) measured in ROIs (blue and green regions located in the squared element of the first row). Images are displayed in dB scales. The characterization of the system's lateral resolution was performed for the following optical configurations (Fig. 4.3): SMF (a, e, i), combined MSPL channels (b, f, j), MSPL Channel 1 (c, g, k), and MSPL Channel 2 (d, h, l). MSPL Channel 1, combined MSPL channels, and SMF configurations generated similar images in terms of spatial resolution. For the SMF configuration, the smallest distinguishable elements in the vertical and horizontal directions were Group 7, Element 1 (with a bar thickness of 3.91 µm) and Group 6, Element 6 (with a bar thickness of 4.38 µm), respectively. Both the combined channels and Channel 1 resolved Group 6, Element 6 (with a bar thickness of 4.38 µm) in both the vertical and horizontal directions. The difference in bar thicknesses measured for Group 6, Element 6 by the SMF and MSPL configurations might be explained by variations in the system NA as described in Sec. 4.2.1. More interestingly, the combined channels and Channel 1 could resolve the same element, suggesting that averaging the speckle with our method did not affect the image spatial resolution. Fig. 4.3 (j-l) displays the 10-90% edge response distances horizontally and vertically. The horizontal and vertical SMF edge response distances were 5.3 µm and 5.9 µm, respectively. For the combined MSPL channels, the horizontal and vertical distances were 3.0 µm and 4.0 µm, respectively, while for Channel 1, the distances were 3.0 µm and 3.6 µm, respectively. The SMF spatial resolution assessed by the quantitative method was lower than for the MSPL system, while it was the opposite observation for qualitative measurements of the smallest distinguishable elements. This inconsistency is likely due to the limitation to obtaining a perfect Gaussian response in the MSPL configuration (Fig. 4.3 (i-l)). Both the quantitative and qualitative methods to assess the MSPL spatial resolution suggest that combining the channels had limited impact on it. Fig. 2 (l) suggests that the MSPL Channel 2 acts as an edge detector in the vertical axis of the image. This is likely due to the CSF shape mimicking the application of a Sobel filter used for image edge detection [139]. In Fig. 2 (i), a dip in the signal was observed, which is not occurring in Fig. 2 (j–l). It is probably due to a speck of dust on the test chart that was not present in the other images since the alignment was slightly changed when changing from the SMF to the MSPL configurations.

Fig. 4.4 shows an OCT C-scan of the plastic cap with values of the speckle contrast (C_s) and SNR (a–c) averaged from signals in the red ROI, zoom-in images of the speckle pattern from the red ROI (d–f), and B-scans of a fingernail with corresponding C_s and SNR (g–i) for the combined MSPL channels (left column), MSPL Channel 1 (middle column), and MSPL Channel 2 (right column) calculated over the red ROI. Images are displayed in dB scale. The normalized second-order cross-correlation measured between MSPL channels was 1.04,

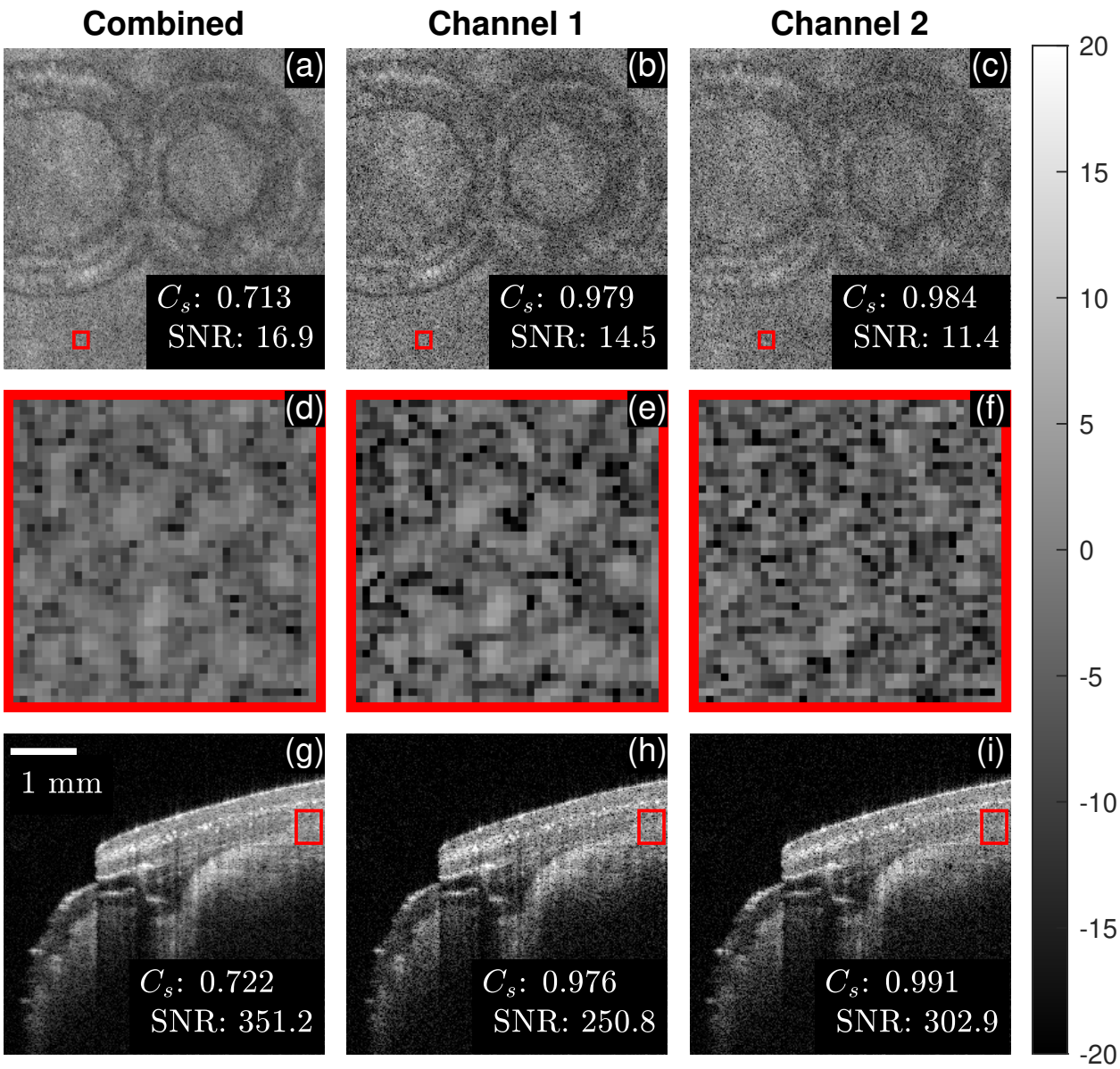

Figure 4.4 *En-face* OCT images of within a plastic cap engraved with the number 8 acquired with (a) the combined MSPL channels, (b) Channel 1, and (c) Channel 2. Speckle contrast (C_s) and SNR values are provided for each case. (d-f) Corresponding zoom-in images of the speckle pattern for each optical configuration. (g-i) *In vivo* B-scans of a fingernail and corresponding speckle contrast and SNR for each case. All images are displayed in dB scale.

suggesting that the two speckle patterns are uncorrelated. The engraved shape (number 8) of the cap becomes more visible when the speckle contrast is reduced, *i.e.* for the combined MSPL channels ($C_s = 0.713$) compared to separate channels ($C_s = 0.979$ and $C_s = 0.984$ for MSPL Channel 1 and 2, respectively). This represents a reduction of 27% and 28%, respectively. This improvement corresponds to what was predicted by Eq. 4.2. SNR also improves when combining MSPL channels (SNR = 16.9) compared to MSPL Channel 1 (SNR = 14.5) and Channel 2 (SNR = 11.4), respectively. This represents an SNR improvement of 17% and 48%, respectively. In the zoom-in images, the averaged speckle pattern becomes smoother for the MSPL combined channels configuration, which indicates a lower speckle contrast. This observation also applies to the *in vivo* images of the fingernail, where the MSPL combined speckle contrast patterns ($C_s = 0.722$) is reduced compared to that of individual channels ($C_s = 0.976$ and $C_s = 0.991$ for MSPL Channel 1 and Channel 2, respectively). This represents a reduction of speckle noise of 26% and 27% and an increase in SNR of 40% and 16%, for Channel 1 and Channel 2, respectively. A higher SNR was observed for *in vivo* images with respect to *in vitro* images. This difference is likely due to the depth of the ROI, which was higher for *in vitro* images. Furthermore, a higher SNR was observed in Channel 2 compared to Channel 1 in *in vivo* images compared to *in vitro* images. This is consistent with biological tissues containing a wide variety of scatterer geometries which were shown by our group to have a strong effect on modal coupling efficiencies [17].

These results show a reduction of speckle noise in both *in vitro* and *in vivo* experiments when using an MSPL optical configuration for OCT imaging. The results also suggest that adding additional higher modes would further decrease speckle noise as long as additional CSFs are orthogonal. In addition, the MSPL could be combined with other speckle-reduction techniques for more effectiveness. These capacities have to be demonstrated in a future study.

Aside from managing the retro-reflection from the tip of the MSPL, described earlier, limitations in this study included the SMF and MSPL having different NAs which required adapting the imaging head, namely the collimating lens, to compare the lateral resolution for each configuration properly. An additional challenge came from properly choosing the subregion size for speckle contrast measurement. The subregion size was chosen by simulating a range of phasors until speckle contrast yielded values consistent with that of a fully developed speckle pattern.

4.4 Conclusion

We have demonstrated how an MSPL can be used in an OCT system to reduce the speckle contrast and increase SNR with negligible impact on image spatial resolution. We have

measured a significant decrease in speckle contrast in both *in vitro* (27-28%) and *in vivo* (26-27%) experiments. Combining the two channels into a composite image increased the SNR over Channel 1 and Channel 2 by 17% and 48%, respectively *in vitro*, and by 40% and 16%, respectively, *in vivo*. Further improvement is expected in speckle reduction by adding modes through a 3×1 or 4×1 MSPL, and by integrating common speckle reduction techniques to the resulting OCT image. However, as several reference arms are necessary to account for different modal propagation constants, photon budgeting must be adjusted accordingly with a more powerful laser.

Funding

This work was supported by the Natural Sciences and Engineering Research Council of Canada (NSERC) grants #RGPIN-2018-06151 (to C.B.), #RGPIN-2015-04672 and #RTI-2016-00636 (to M.D.) as well as financial support from the TransMedTech Institute (to R.M.T). This research was conducted as part of the TransMedTech Institute's activities and thanks, in part, to funding from the Canada First Research Excellence Fund.

Acknowledgements

A preliminary version of this work was presented orally at the session "Bio-Optics Design and Applications" of the Optical Biophotonics Congress in 2023, "Speckle Contrast Reduction through the use of a Modally-Specific Photonic Lantern in Few-Modes Optical Coherence Tomography" [140]. The authors would like to thank Castor Optics, inc. for supplying an MSPL prototype.

Disclosures

C.B.: Castor Optics, inc. (I,P). The other authors have no conflict to disclose.

Data Availability

Imaging datasets acquired in this work are not publicly available at this time but may be obtained from the authors upon reasonable request.

CHAPTER 5 PRIOR WORKS ON FEW-MODE OPTICAL COHERENCE TOMOGRAPHY FLOW MEASUREMENTS

The article on flow measurement in Chapter 6 summarizes and concludes multiple iterations and innovations aimed at utilizing an MSPL for flow measurement. This chapter details the prior work and experimental developments that culminated in the innovation described in Chapter 6.

5.1 Prior methods

Initial experiments utilized a two-mode MSPL. The second-order autocorrelation of the LP11 channel, $g_{22}^{(2)}$, was leveraged to measure flow. Figure 5.1 displays the second-order autocorrelation curves obtained at various positions within an OCT image of diluted milk flowing through a cylindrical tube. The color gradient from dark to light blue corresponds to measurements at 0 µm, 80 µm, 120 µm, and 160 µm from the tube center, respectively. The vertical lines correspond to the positions of the second peak. The estimated average flow speed in the tube is also displayed.

The first peak occurs at zero delay and is fully correlated since it corresponds to the autocorrelation of the same image. The second peak arises when a particle moves from under one of the LP11 lobes to the other. By knowing the fixed distance between the lobes and recording the delay associated with the second peak in Fig. 5.1, the flow speed can be calculated.

This approach, however, tended to overestimate flow speed due to diffusion effects. Diffusion reduced the height of the second peak, complicating its measurement, and shifted its position to higher delay values, resulting in an overestimation of flow speed. Additionally, the broadness of the peak rendered the maximum position less reliable, further diminishing measurement accuracy.

The second approach involved using the cross-correlation between the two channel signals, $g_{12}^{(2)}$. Figure 5.2 presents $g_{12}^{(2)}$ for simulated particles moving at 8 mm/s with diffusion coefficients of 0 µm^2/s, 2 µm^2/s, 4 µm^2/s, 6 µm^2/s, and 8 µm^2/s. As in the previous method, the delay between the two peaks was used to determine the transit time of a particle from one lobe to the other, thereby allowing calculation of flow speed.

This method offered the advantage of higher correlation peak values, facilitating the measurement of peak positions and reducing the likelihood of inconclusive flow measurements. Early results indicated that this approach was more accurate than other correlation methods,

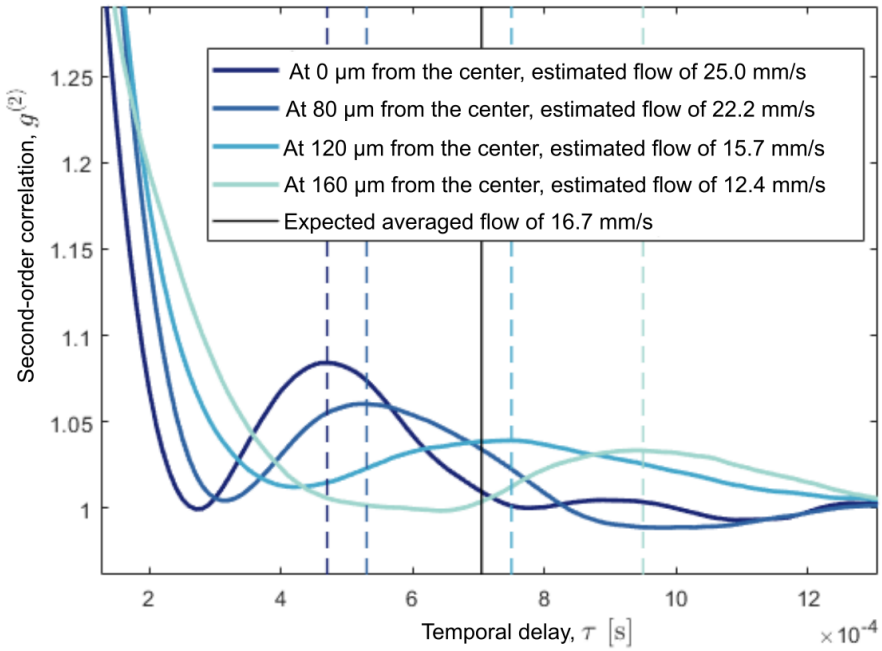

Figure 5.1 Second-order autocorrelation curves ($g_{22}^{(2)}$) measured at lateral positions of 0, 80, 120, and 160 µm from the center of a cylindrical tube containing flowing milk. The color gradient from dark to light blue corresponds to increasing distance from the tube center. Dashed vertical lines indicate the positions of the second-peak maxima, which are used to estimate the flow speed. The estimated average flow speed in the tube is 16.7 mm/s.

such as v_{sp} and v_{fit}, discussed in Chapter 6.

However, diffusion continued to cause overestimation of flow speed, as shown in Fig. 5.2, where increasing diffusion coefficients result in closer peak positions. Additionally, this technique required M-mode scans to obtain correlation measurements at multiple delays for accurate peak localization. Unlike $g_{22}^{(2)}$, cross-correlation necessitated coregistration of signals from both channels, introducing additional complexity. While the MSPL ensured lateral coregistration, axial coregistration had to be addressed separately, as described in Chapter 6.

The concept of employing a ratio was motivated by the goal of eliminating the diffusion contribution observed in the previous methods. Because the second-order correlation function exhibits a nonzero offset for completely decorrelated signals, first-order correlation was adopted. The relationship $g^{(2)} = |g^{(1)}|^2 + 1$ allows translation from second- to first-order correlation; however, the offset d discussed in Chapter 6 complicated the use of ratios in this context.

The ratios between all combinations of auto- and cross-correlation were calculated theoreti-

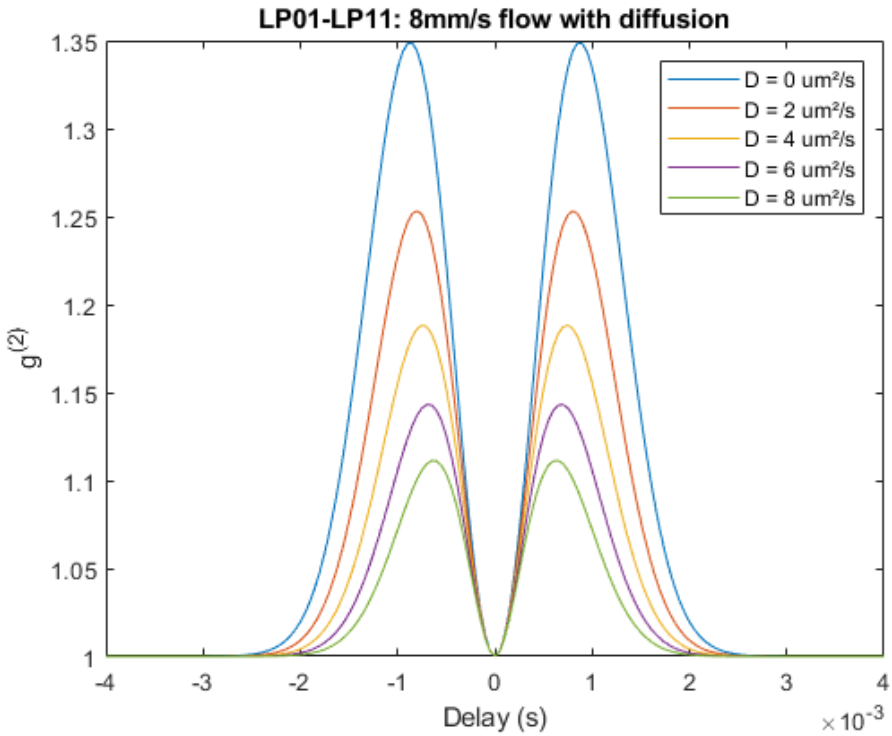

Figure 5.2 Cross-correlation curves ($g_{12}^{(2)}$) for simulated particles moving at 8 mm/s, with diffusion coefficients of 0, 2, 4, 6, and 8 µm^2/s shown in blue, orange, yellow, purple, and green, respectively.

cally and are presented in Fig. 5.3. The $\eta_{\mathrm{ij/kl}}$ represents the correlation between Channels i and j divided by the correlation between Channels k and l.

Any of these ratios could, in principle, be used to calculate flow; however, $\eta_{12/11}$ was selected due to its linear relationship with flow speed. This linearity obviated the need for curve fitting or M-mode scans. The implementation of first-order correlation, however, introduced additional complexity, as it required phase stabilization of the system.

5.2 The polarization issue

The correlation ratio method was initially tested using a two-mode MSPL. Numerous measurements were performed as the experimental methodology was refined. Additional results not included in the published manuscript include measurements using alternative liquid media and those obtained with polarization-sensitive MSPL.

Early two-mode MSPL devices exhibited partial polarization sensitivity. The orientation of the LP11 lobes could rotate slightly depending on the incident light polarization, as illustrated

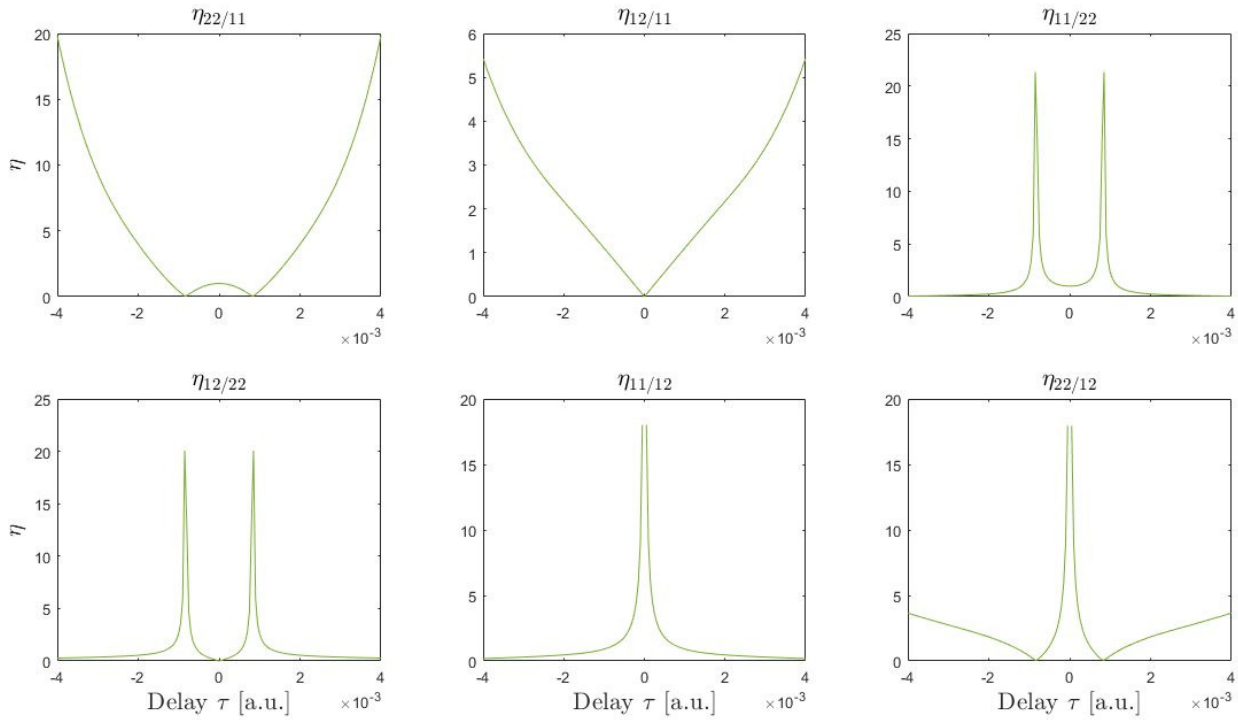

Figure 5.3 Theoretically possible correlation ratios ($\eta_{\mathrm{ij/kl}}$) calculated from all auto- and cross-correlation combinations when using two channels. Here, $\eta_{\mathrm{ij/kl}}$ denotes the ratio of the correlation between channels i and j to that between channels k and l.

in Fig. 5.4. This figure shows an en face image of the absolute value of $|g_{22}^{(1)}|$ for a static object, where delays along the two axes correspond to translations of the object. The polarization controller was used to alter the detected polarization between images (a) and (b), resulting in the observed tilt in (b).

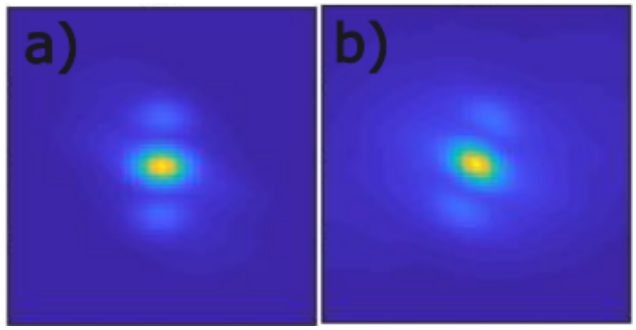

Figure 5.4 En-face images of $|g_{22}^{(1)}|$ for a static object, with both axes corresponding to translations in the x and y directions. The detected polarization was altered between (a) and (b) using a polarization controller, resulting in the observed change in lobe orientation.

This polarization dependence introduced errors due to uncertainty in the measured direction, which varied with polarization. To address this, a polarization beam splitter was placed in front of the lantern to ensure consistent polarization collection, albeit at the expense of some signal loss.

A similar phenomenon occurs with three-mode MSPL devices, which may also exhibit polarization sensitivity. While the two LP11 modes remain orthogonal, their orientations rotate with changing polarization. Unlike the two-mode case, the measured velocity remains accurate because both orthogonal directions are assessed; thus, the total velocity is the sum of speed measurements in both directions, irrespective of orientation. The preferred solution was to employ a non-polarization-sensitive MSPL.

5.3 Measurements on blood

To validate that diluted milk served as an adequate blood surrogate, the method was also tested with pork blood. The corresponding experiments, shown in the figure, mirror those in Chapter 6 but utilize a two-mode MSPL and pork blood. The blue dots represent flow measured by v_{tot}, the green circles by v_{sp}, and the black line indicates the expected flow speed. The blood, obtained from a butcher, had already begun to coagulate, making it an imperfect analogue for human blood and resulting in a low SNR image (SNR ≈ 3).

The various diffusers exhibited behavior similar to that observed with milk, confirming that diffuser size and shape do not generally affect correlation methods, as previously suggested [73]. Further tests with Intralipid yielded the same conclusion. Consequently, experiments continued with milk due to its availability and higher SNR. Notably, the blood measurements demonstrated that the ratio method remains effective for flow quantification even at SNR values as low as 3.

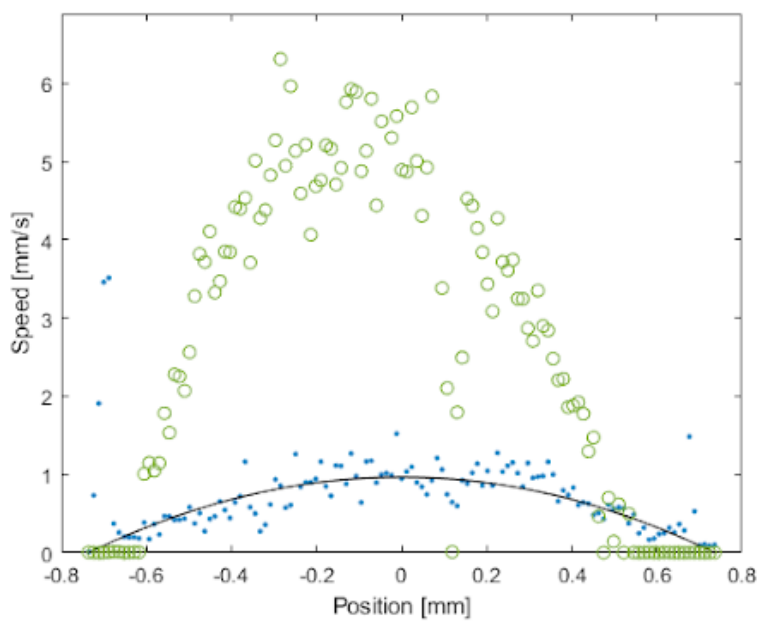

Figure 5.5 Measured flow velocities of pork blood in a cylindrical tube using a two-mode mode-selective photonic lantern. The black line represents the expected flow, while blue dots and green circles correspond to flow measurements obtained by v_{tot} and v_{sp}, respectively. The experiment demonstrates effective flow quantification even at low SNR values (≈ 3).

CHAPTER 6 ARTICLE 3 - ACCURATE FLOW SPEED MEASUREMENT THROUGH CORRELATION RATIOS USING A MODE-SELECTIVE PHOTONIC LANTERN IN OPTICAL COHERENCE TOMOGRAPHY

This article presents a novel method for flow measurement using OCT. The work described constitutes the most significant contribution of this PhD and has resulted in a patent. The article begins by developing the theoretical framework for the correlation ratio method, followed by a description of the experimental methodology. Flow measurements are performed under various conditions, and the results are compared with existing techniques, demonstrating enhanced accuracy. Additionally, the method provides information on flow direction. Further results explore the relationship between measurement precision and integration time.

Accurately and quantitatively measuring blood flow transverse to the axial direction has long been a challenge for OCTA. This article proposes a novel solution to this problem.

Contribution: The lead author, Raphaël Maltais-Tariant, contributed approximately 90% of the work, including literature review, system assembly, software development, experimental protocol design, data acquisition and analysis, and manuscript preparation. Rodrigo Itzamna Becerra-Deana and Simon Brais-Brunet provided valuable input and contributed to manuscript revision. Prof. Mathieu Dehaes, PhD, and Prof. Caroline Boudoux, Pr. Eng., PhD, served as principal investigators, offering guidance throughout the project and assisting with article revision.

Authors: Raphaël Maltais-Tariant, Rodrigo Itzamna Becerra-Deana, Simon Brais-Brunet, Mathieu Dehaes, and Caroline Boudoux.

Abstract: A novel method for measuring non-axial flow speed using optical techniques such as optical coherence tomography is introduced. The approach was based on the use of a modally-specific photonic lantern, which permits simultaneous probing of the sample with three distinct coherent spread functions. Transverse flow speed is measured from the ratio between the cross-correlation and autocorrelation of the signals. It achieved a 3 to 5 times higher accuracy than common autocorrelation approaches and measured flows as slow as 0.5 mm/s for an integration time of 1 second. Additionally, the method gives information on the flow's three-dimensional orientation, does not require information about the diffusion coefficient, and is more robust to bias errors such as a gradient in the axial flow velocity.

Article published: Biomedical Optics Express, July 2025

DOI: 10.1364/BOE.564589

Submitted: May 29, 2025

6.1 Introduction

Optical coherence tomography (OCT) is an imaging technique that has revolutionized the field of ophthalmology by providing non-invasive, high-resolution (∼10 µm), three-dimensional visualization of the retina and its vasculature without the need for contrast agents [1, 18]. Monitoring of blood flow in the retina is key for diagnosing several ophthalmologic pathologies [141,142], avoiding damage to important blood vessels during surgery or ensuring vascular integration during transplant [143, 144]. As such, many techniques have been developed to image blood vessels and quantify their flow [62,66,68,69,145–154]. Although qualitative flow measurement is readily achieved, accurate quantitative measurements remain challenging and are needed for accurate monitoring and comparative studies.

Doppler OCT can precisely and accurately measure axial flow velocity even at subdiffusion speed [68]. However, for the retina, most blood vessels are located in-plane and orthogonal to the imaging axis. Some systems image the retina at three angles to overcome this limitation [69]. Such systems are technically challenging to implement, particularly for imaging small eyeballs such as found in mouse pup models of pediatric diseases [70]. Furthermore, studies have shown how Doppler OCT can produce inaccurate measurements [10] and its particular limitation to quantify high flow speeds [62].

Neural networks, which are increasingly popular, have also been applied to the challenge [71], with limited accuracy. Alternatively, calculating variance is used to highlight blood flow. Accurate estimation of the blood flow remains challenging [66,67]. To remedy this, it is often used in conjecture with other techniques such as speckle decorrelation for more quantitative results [67, 72].

Many techniques rely on measuring blood flow-induced speckle pattern decorrelation [62–64]. The flow velocity is calculated by measuring the decorrelation at a specific delay or for multiple delays, in which case a fit of the correlation curve provides the particle speed. When measuring flow with a single delay, diffusion, signal-to-noise ratio, and bulk motion from the sample need to be accurately known or will otherwise induce a bias in the measurement. While fitting on a correlation curve is more robust to those errors, implementing the fitting approach is more challenging since it requires imaging the same point in very short intervals. Even when all those factors are adequately considered, inaccuracies occur due to axial gradient velocity (AGV) and shadow artifacts [10, 73]. AGV refers to the axial component of the flow in a single pixel that is not uniform across the pixel. The sub-resolution variation

of the axial flow causes an overestimation of the flow speed. Estimating sub-diffuse blood speed also remains problematic [74].

This work introduces a technique to accurately quantify flow using a 3-mode, mode-selective photonic lantern (MSPL) in OCT [14, 56–58]. MSPLs are fiber-based n-by-1 couplers acting as a demultiplexer for higher-order fiber spatial modes such as LP01 and the two LP11 modes. Once demultiplexed into distinct single-mode fibers, the modes are imaged by independent OCT systems, creating a few-mode OCT (FM-OCT) [14–17].

This technique is based on the calculation of correlation ratios from 3 distinct complex spread functions (CSF) [65]. This approach has shown promising results using two modes of photonic lanterns [155] and other CSF engineering methods, giving improved measurements than just using correlation [11]. Here, the technique shows that using 3 modes provides more accurate measurements of flow velocity compared to other correlation-based approaches. It also determines the flow direction in three dimensions. Furthermore, such a CSF-engineered approach is not limited to OCT and could be applied to other imaging devices based on coherent light detection such as laser speckle imaging [156–159].

6.2 Theory

In this section, we derive an expression for the ratio of correlations using an OCT system with three distinct coherent spread functions.

6.2.1 Coherent spread function in optical coherence tomography

The OCT signal (E) of a single pixel can be approximated by the light reflectance from multiple particle scatterers randomly distributed in space such as [63, 64]:

$$E = \sum_{i=1}^{N} r_i \cdot h_{xy}(x_i, y_i) \cdot h_z(z_i), \tag{6.1}$$

where N is the number of scatterers, r_i is the reflectivity of each ith scatterer, x_i, y_i, and z_i describe the 3D position of a scatterer, and h_{xy} and h_z are the CSF in the lateral and axial directions, respectively. For simplicity and without impacting the accuracy, r_i can be approximated to 1 [63]. At the beam focus location, the axial CSF is often approximated as a Gaussian curve by [64]:

$$h_z(z) = \sqrt{\frac{2}{\sqrt{\pi} w_z}} \cdot \exp\left[-iqz\right] \cdot \exp\left[-2\frac{z^2}{w_z^2}\right] \tag{6.2}$$

where $q = 2k_0 n$, k_0 is the central wavenumber, n is the refractive index, z is the axial position in depth orientation, and w_z is the beam waist. The first term is a normalization factor, the second is the phase response, while the last is the amplitude response. The lateral CSF is defined by a combination of the imaging lens, collimating lens, and the optical fiber-guided modes used for illumination and collection. The system is assumed to be free of aberrations. Since OCT typically uses single-mode fibers, the illumination and collection are performed by the LP01 mode which can be approximated by a Gaussian function [160] :

$$f_{\mathrm{LP01}}(x, y) = \exp\left[-\frac{x^2 + y^2}{w_{xy}^2}\right] \tag{6.3}$$

where x and y are the lateral positions and w_{xy} is the beam waist size.

The system was based on a 3-mode MSPL replacing the single-mode fiber used for both illumination and collection of light [14,56–58]. These optical components have been used with OCT before to reduce speckle noise and explore a new type of contrast [17,140]. Illumination was performed through the LP01 mode while light was collected from all 3 modes including LP01 and the two orthogonal LP11 modes: horizontal ($\mathrm{LP11_h}$) and vertical ($\mathrm{LP11_v}$). To simplify notation, the OCT signal collected by the LP01 mode is defined by Channel 1 (Ch1) while the ones collected by $\mathrm{LP11_h}$ and $\mathrm{LP11_v}$ are defined Channel 2 (Ch2) and Channel 3 (Ch3), respectively.

The lateral CSF is then defined by the product of the illumination and collection modes [161]:

$$h_{xy}(x, y) = f_{\mathrm{LP01}}(x, y) \cdot f_{\mathrm{LP01}}(x, y) = \exp\left[-2\frac{x^2 + y^2}{w_{xy}^2}\right]. \tag{6.4}$$

To facilitate further mathematical calculations, h_{xy} can be normalized as follows:

$$h_{xy}(x, y)|_{\mathrm{Ch1}} = \frac{2}{\sqrt{\pi} w_{xy}} \exp\left[-2\frac{x^2 + y^2}{w_{xy}^2}\right]. \tag{6.5}$$

Similarly to the approximation of f_{LP01} from Eq. 6.3, the horizontal and vertical fiber mode distributions of the higher order modes f_{LP11} are expressed as:

$$f_{\mathrm{LP11,h}}(x, y) = \frac{x}{\zeta \cdot w_{xy}} \exp\left[-\frac{x^2 + y^2}{(\gamma \cdot w_{xy})^2}\right] \text{ and } f_{\mathrm{LP11,v}}(x, y) = \frac{y}{\zeta \cdot w_{xy}} \exp\left[-\frac{x^2 + y^2}{(\gamma \cdot w_{xy})^2}\right] \tag{6.6}$$

where the fitting parameters $\zeta = 0.7036$ and $\gamma = 0.9279$ were obtained by fitting f_{LP11} over the Bessel and modified Bessel functions used to define LP11. The resulting normalized lateral CSF for Ch2 ($h_{xy,2}$) and Ch3 ($h_{xy,3}$) were obtained by multiplying the f_{LP01} (for

illumination) and $f_{\mathrm{LP11,h}}$ or $f_{\mathrm{LP11,v}}$ (for collection), respectively. This is expressed as:

$$h_{xy}(x,y)|_{\mathrm{Ch2}} = \sqrt{\frac{2}{\pi}}\frac{\xi}{w_{xy}^2}\cdot x\cdot \exp\left[-\xi\frac{x^2+y^2}{(w_{xy})^2}\right] \text{ and } h_{xy}(x,y)|_{\mathrm{Ch3}} = \sqrt{\frac{2}{\pi}}\frac{\xi}{w_{xy}^2}\cdot y\cdot \exp\left[-\xi\frac{x^2+y^2}{(w_{xy})^2}\right] \tag{6.7}$$

where $\xi = (1+\gamma^2)/\gamma^2$.

6.2.2 Signal correlation

The first-order correlation can be calculated as follows:

$$g_{AB}^{(1)}(\tau) = \frac{\langle E_A^*(0)\odot E_B(\tau)\rangle}{\sqrt{\langle|E_A^*(0)|\rangle\cdot\langle|E_B(\tau)|\rangle}}, \tag{6.8}$$

where A and B are the signals being correlated and acquired by an unspecified channel A and B, τ is the correlation delay, E is the OCT tomogram complex signal, E^* is the complex conjugate of E, $\odot$ is the Hadamard product, and $\langle ...\rangle$ is the ensemble average. The subscripts 1, 2, and 3 are used to refer to Ch1, Ch2, and Ch3, respectively, when the correlated channels A and B are specified. The theoretical expected value of Eq. 6.8 is affected by flow and can be determined as follows. The correlation values of a single moving scatterer are calculated over all possible initial positions (x_0, y_0, z_0) and averaged using an integral with normalized CSFs [63, 64]. By following this approach, we obtain this expression:

$$g_{AB}^{(1)}(\tau) = \iiint_{\infty}^{\infty} h_{xy}^*(x(0),y(0))\Big|_A \cdot h_{xy}(x(\tau),y(\tau))|_B \cdot h_z^*(z(0))\cdot h_z(z(\tau))dx_0dy_0dz_0, \tag{6.9}$$

where x, y, and z stand for the scatter position at a particular time τ. Those positions vary in time as follows:

$$\begin{aligned} x(\tau) &= x_0 + v_x\cdot\tau + x'(\tau),\\ y(\tau) &= y_0 + v_y\cdot\tau + y'(\tau),\\ z(\tau) &= z_0 + v_z\cdot\tau + z'(\tau), \end{aligned} \tag{6.10}$$

where v_x, v_y, and v_z are the flow velocity components along those axes and x', y', and z' are the displacements caused by diffusion. Thus, x_0, y_0, and z_0 are possible positions of the scatterer at time $\tau = 0$.

Separating the decorrelation signal generated by the flow ($g_{AB}^{(1)}(\tau)|_f$) and diffusion ($g_{AB}^{(1)}(\tau)|_D$)

into two terms was previously proposed since they are uncorrelated phenomena [64]:

$$g_{AB}^{(1)}(\tau) = g_{AB}^{(1)}(\tau)\Big|_f \cdot g_{AB}^{(1)}(\tau)\Big|_D, \tag{6.11}$$

where $g_{AB}^{(1)}(\tau)|_f$ can be calculated from Eq. 6.9, but without the diffusion motion in Eq. 6.10. The decorrelation due to diffusion is primarily related to the random phase variations of the signal of the scatterers caused by their axial motions instead of signal amplitude variations caused by 3D motions [64]. Thus, the diffusion decorrelation is invariant between channels and can be expressed by:

$$g_{AB}^{(1)}(\tau)\Big|_D = \exp\Big[-q^2 D \mid \tau \mid\Big], \tag{6.12}$$

where D is the diffusion coefficient. Taking the absolute value of τ accounts for negative delays. Equations 6.9, 6.11, and 6.12 can then be used to calculate the expected value for the auto-correlation of Ch1 [63, 64] as:

$$g_{11}^{(1)}(\tau) = \exp\left[iqv_z\tau\right] \cdot \exp\left[-\frac{(v_x^2+v_y^2)\tau^2}{w_{xy}^2}\right] \cdot \exp\left[-\frac{v_z^2\tau^2}{w_z^2}\right] \cdot \exp\Big[-q^2 D \mid \tau \mid\Big]. \tag{6.13}$$

The first term is the Doppler term, the second gives the decorrelation due to non-axial flow, the third is the decorrelation due to axial flow, and the last is the decorrelation due to diffusion. The cross-correlations of Ch1 with Ch2 or Ch3 are expressed by:

$$\begin{aligned} g_{12}^{(1)}(\tau) &= \exp\left[iqv_z\tau\right] \cdot 1.41\frac{v_x\tau}{w_{xy}} \cdot \exp\left[-1.04\frac{(v_x^2+v_y^2)\tau^2}{w_{xy}^2}\right] \cdot \exp\left[-\frac{v_z^2\tau^2}{w_z^2}\right] \cdot \exp\Big[-q^2 D \mid \tau \mid\Big], \\ g_{13}^{(1)}(\tau) &= \exp\left[iqv_z\tau\right] \cdot 1.41\frac{v_y\tau}{w_{xy}} \cdot \exp\left[-1.04\frac{(v_x^2+v_y^2)\tau^2}{w_{xy}^2}\right] \cdot \exp\left[-\frac{v_z^2\tau^2}{w_z^2}\right] \cdot \exp\Big[-q^2 D \mid \tau \mid\Big], \end{aligned} \tag{6.14}$$

where the factors 1.41 and 1.04 come from the constant ξ in Eq. 6.7 once integrated in Eq. 6.9. More interestingly, we can calculate the ratios of the previous equations:

$$\begin{aligned} \eta_{12/11}(\tau) &= \frac{g_{12}^{(1)}(\tau)}{g_{11}^{(1)}(\tau)} = 1.41\frac{v_x\tau}{w_{xy}} \exp\left[-0.04\frac{(v_x^2+v_y^2)\tau^2}{w_{xy}^2}\right], \\ \eta_{13/11}(\tau) &= \frac{g_{13}^{(1)}(\tau)}{g_{11}^{(1)}(\tau)} = 1.41\frac{v_y\tau}{w_{xy}} \exp\left[-0.04\frac{(v_x^2+v_y^2)\tau^2}{w_{xy}^2}\right], \end{aligned} \tag{6.15}$$

and obtain a quasi-linear relationship that is independent of diffusion. A previous study demonstrated how AGV introduces additional terms to Eq. 6.13, resulting in an increased rate of decorrelation and, consequently, an overestimation in flow measurements [10]. A similar

effect is expected for Eq. 6.14, though the exact expression remains unknown. However, using a correlation ratio cancels out such sources of error when the axial velocity is only determined by the axial position: $v_z(z)$. In this case, the triple integral from Eq. 6.9 can be divided into a double integral in the xy plane and a single integral for v_z:

$$\begin{aligned} g_{AB}^{(1)}(\tau) = &\iint_{\infty}^{\infty} h_{xy,A}^{*}(x_0, y_0) \cdot h_{xy,B}(x_0 + x(v_x \cdot \tau), y(y_0 + v_y \cdot \tau)) dx_0 dy_0 \\ &\times \int_{\infty}^{\infty} h_z^{*}(z(0)) \cdot h_z(z_0 + v_z(z) \cdot \tau) dz_0. \end{aligned} \tag{6.16}$$

The axial integral is invariant between channels and does not contribute to $\eta_{12/11}$ nor $\eta_{13/11}$. Thus, an AGV solely defined in the axial direction, as is the case considered in this work, will not affect the flow speed measurements.

Similarly to calculating statistics such as the standard deviation of a population, the more independent measurements are used to calculate the correlation, the more the measured value will converge toward its expected value (either from Eq. 6.13 or Eq. 6.14). Also, this uncertainty is higher at lower correlation values [150, 162, 163]. Since $g_{12}^{(1)}(\tau = 0) = 0$, we can expect an unknown complex number offset d. Assuming this offset, Eq. 6.15 becomes:

$$\begin{aligned} \eta_{12/11}(\tau) &= \frac{g_{12}^{(1)}(\tau)}{g_{11}^{(1)}(\tau)} = 1.41 \frac{v_x \tau}{w_{xy}} \exp\left[-0.04 \frac{(v_x^2 + v_y^2)\tau^2}{w_{xy}^2}\right] + \frac{d}{g_{11}^{(1)}(\tau)}, \\ \eta_{13/11}(\tau) &= \frac{g_{13}^{(1)}(\tau)}{g_{11}^{(1)}(\tau)} = 1.41 \frac{v_y \tau}{w_{xy}} \exp\left[-0.04 \frac{(v_x^2 + v_y^2)\tau^2}{w_{xy}^2}\right] + \frac{d}{g_{11}^{(1)}(\tau)}. \end{aligned} \tag{6.17}$$

The contribution of this offset can be canceled by calculating the variation around $\tau = 0$, while the exponential can also be neglected since its value is very close to 1. In this case, the variations of η around $\tau = 0$ can be defined by:

$$\begin{aligned} \Delta\eta_{12/11}(\tau) &= \eta_{12/11}(\tau) - \eta_{12/11}(-\tau) = 2 \cdot 1.41 \frac{v_x \tau}{w_{xy}}, \quad \text{and} \\ \Delta\eta_{13/11}(\tau) &= \eta_{13/11}(\tau) - \eta_{13/11}(-\tau) = 2 \cdot 1.41 \frac{v_y \tau}{w_{xy}}. \end{aligned} \tag{6.18}$$

Thus, the flow speed in the x and y directions can be calculated using the following equations:

$$\begin{aligned} v_x &= \frac{w_{xy}}{1.41 \cdot 2\tau} \left|\eta_{12/11}(-\tau) - \eta_{12/11}(\tau)\right|, \\ v_y &= \frac{w_{xy}}{1.41 \cdot 2\tau} \left|\eta_{13/11}(-\tau) - \eta_{13/11}(\tau)\right|. \end{aligned} \tag{6.19}$$

The application of the modulus operator is necessary since complex contributions remain

after the subtraction. Because of this, Eq. 6.19 only gives us the amplitude of the flow speed. It cannot differentiate between a positive or negative value of v_{x} or v_{y}. Finally, the total flow speed can be calculated from its components such as:

$$v_{\mathrm{tot}} = \sqrt{v_x^2 + v_y^2 + v_z^2}, \tag{6.20}$$

where v_z is the axial component of the velocity obtained through Doppler OCT [68]:

$$v_z = \langle \angle E_1(\tau) - \angle E_1(0) \rangle \cdot \frac{1}{2k_0 n \cdot \tau}, \tag{6.21}$$

where $\angle E_1(\tau)$ is the phase of the signal at a time τ. Alternatively, the ratio variation can be expressed independently of the flow direction as follows:

$$\Delta\eta_{\mathrm{tot}} = \sqrt{\Delta\eta_{12/11}^2 + \Delta\eta_{13/11}^2}. \tag{6.22}$$

6.3 Material and methods

A few-mode OCT system was designed using a three-mode, mode-selective photonic lantern to quantify the accuracy of the correlation ratio approach to estimate flow speed.

6.3.1 FM-OCT system and experiments

The FM-OCT system comprises a swept-source laser (SL1310V1, Thorlabs, NJ, USA) and two balanced detectors (PDB460C, Thorlabs, NJ, USA). Fig. 6.1 (a) shows illumination through Ch1 of the MSPL, and interferometric detection of the classical OCT image (Ch1 using balanced detector 1) and the higher-order modes (Ch2 and Ch3, using balanced detector 2). While the MSPL has three channels, and the DAQ board only two analog inputs, both higher-order modes are collected with the same balanced detector using a 50:50 fiber splitter and an adjustable free-space delay line to offset their signals. This combination of signals decreases the SNR but allows acquisition with simpler electronics. The MSPL was held in place with a 3D-printed holder, and an aspheric lens was positioned to collimate its LP01 and LP11 beams. A 2-galvanometer-mounted mirror set and a scan lens (LSM02, Thorlabs, NJ, USA) completed the imaging head. Fig. 6.1 (b, c, and d) show the lateral CSFs for Ch1, Ch2, and Ch3 of the MSPL, respectively.

The MSPL specifications were measured as explained in [58]. It has an operational wavelength range of 500 nm centered around 1300 nm, with a modal isolation of 32 dB, and an excess loss of less than 0.48 dB.

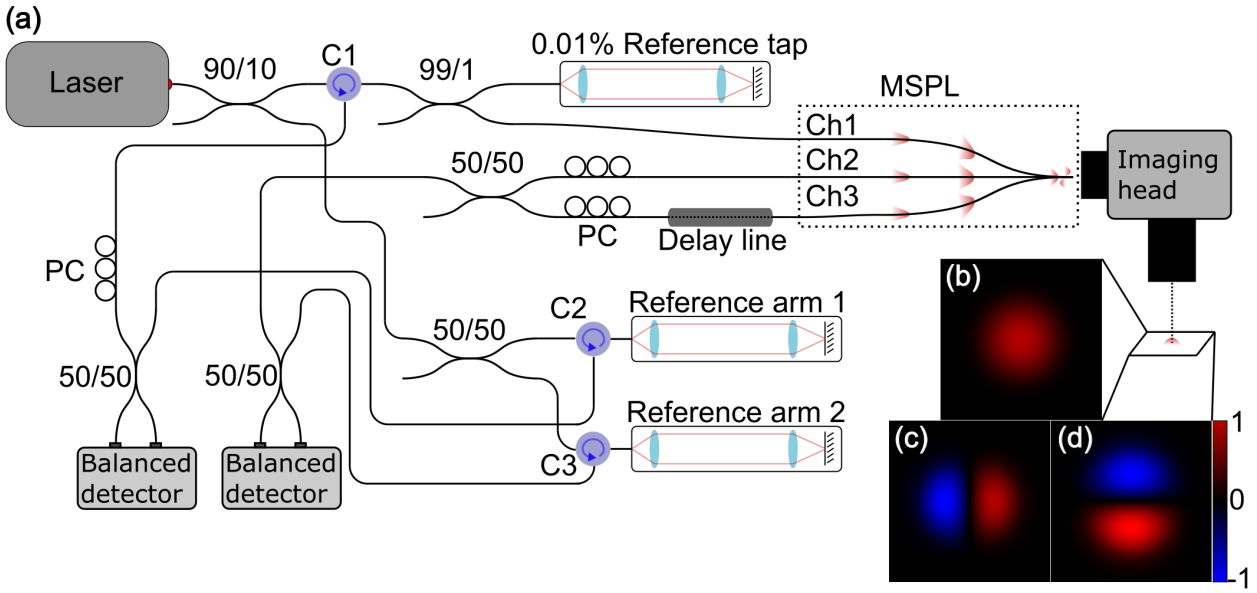

Figure 6.1 A few-mode optical coherence tomography system acquiring interferograms from all three channels of a mode-selective photonic lantern using two reference arms, one for LP01 and one for LP11 modes. Circulators (C1, C2, and C3), polarization controllers (PC) and a variable free-space delay line allow improved visibility and concurrent acquisitions, respectively. Theoretical coherent spread functions for Channels 1 (Ch1), 2 (Ch2), and 3 (Ch3) are shown in (b), (c), and (d), respectively.

First-order correlation measurements require a phase-stable OCT system. Our system was stabilized using the method suggested in a previous study [164]. As illustrated in Fig. 6.1 (a), a 99/1 coupler was added to provide 1% of the signal reflected off a mirror. The calibration signal was measured by Ch1 and numerically applied on the three channels. The calibration A-line was placed above the sample instead of below to address the laser source's phase fluctuations. Cross-correlation required the precise co-registration of the different channels. While the MSPL guarantees transverse co-registration, axial co-registration was achieved numerically. Signal acquisitions were averaged in intensity instead of the complex field to obtain a single speckle-free A-line. A-lines from Ch2 and Ch3 were then shifted in the Fourier domain [165–167] to maximize the second-order correlation function [62] with Ch1. The measured offset was then applied to co-register Ch2 and Ch3 with Ch1.

Three different experiments were performed. Initially, a C-scan of a homogenous piece of plastic was acquired to calibrate the system on a static sample. Secondly, M-mode flow scans were acquired to demonstrate the validity of the correlation ratio method and compare its performance with existing correlation techniques. Finally, flow speed was measured on B-scans to demonstrate the method with an image.

6.3.2 Calibration

A C-scan of a piece of plastic was acquired to provide correlation values for a known displacement in the absence of diffusion and flow. The measurement was used to validate the prediction of the correlations and the ratio values and to calibrate our system by the measurement of w_{xy}. Data from all channels were recorded simultaneously. The oversampled scan consisted of a 300 by 300 A-lines, resulting in a 0.15 mm by 0.17 mm scan region. Values of $g_{11}^{(1)}$, $g_{12}^{(1)}$ and $g_{13}^{(1)}$ were calculated on each en-face image as follows:

$$g_{AB}^{(1)}(\Delta_x, \Delta_y) = \frac{\langle E_A^*(0,0) \odot E_B(\Delta_x, \Delta_y)\rangle}{\sqrt{\langle |E_A(0,0)|^2\rangle \cdot \langle |E_B(\Delta_x, \Delta_y)|^2\rangle}}, \tag{6.23}$$

where $E_A(0)$ refers to a 200 by 200 pixels sub-image centered from the original 300 by 300 pixels en-face image and $E_B(\Delta_x, \Delta_y)$ refers to the sub-image with an offset of Δ_x and Δ_y on the x and y axis, respectively. The correlation was calculated on 100 en-face images inside the plastic piece, and then the absolute value was averaged axially, resulting in a single 101 by 101 pixels correlation map. Then, a fit was used to extract w_{xy}, and $\Delta\eta_{12/11}$ and $\Delta\eta_{13/11}$ were calculated for a known displacement, allowing later flow speed calculations.

6.3.3 M-mode scans

A syringe pump connected to a plastic tube was used to emulate flow as shown in Fig. 6.2. Diluted milk, one part 2% milk for three parts water, was used as a sample for its availability and low absorption. A-lines were acquired in the middle of the tube with an integration time of 1 second. To study the precision of the methods, the 1-second data was subdivided into shorter integration time segments. The flow speed was measured for each segment, and the standard deviation between them was calculated, giving us information about measurement variability. This was done for integration time of 10, 20, 30, 40, and 50 ms.

The transverse angle of the tube θ was varied to 0°, 30°, 60°, and 90° to test the angular measurement capability. The tube was also tilted axially at an angle $\phi = 15°$ to test the effect of AGV. Due to refraction at the air-tube interface, the tilt resulted in an effective angle $\phi = 10°$ between the flow direction and the transverse plane. While the tube's curvature induced optical distortion, those distortions were not on the same axis as the flow and did not contribute to it. A previous study also showed no impact of tube curvature on flow measurement [10].

The non-axial flow (xy plane) was measured using three distinct correlation-based methods: our proposed method (v_{tot}), a fitting approach in logarithmic scale (v_{fit}), and a single sampled

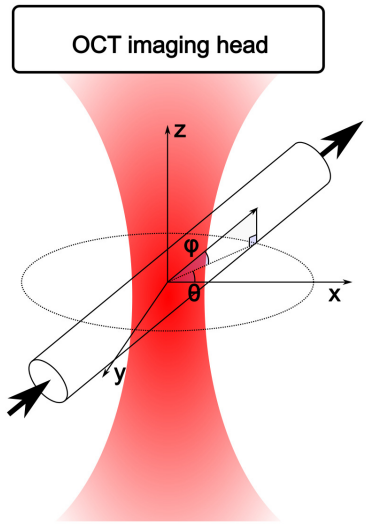

Figure 6.2 Setup used to emulate blood flow. A tube containing flowing scatterers was put at the focus of the FM-OCT imaging head and tilted in plane (four values of θ), and out of plane (one value of ϕ).

point (v_{sp}), as described [62, 64, 147]. The correlation was calculated for time delays ranging from -1 ms to 1 ms for each axial position. Noise correction was applied as described in a previous study [138]. The noise floor was measured and was similar for all depths. It was thus estimated by averaging the signal amplitude in a region without sample. To measure v_{fit}, a fit was applied on the $\log(|g_{11}^{(1)}|)$ curve using Eq. 6.13. The lateral velocity ($\sqrt{v_x^2 + v_y^2}$) was determined using the fit coefficients. The axial velocity (z direction) was added from the Doppler measurement afterward. In parallel, v_{sp} was calculated using the value of $g_{11}^{(1)}$ at $\tau = 1$ ms by isolating the lateral velocity from Eq. 6.13. A moving average of 11 temporal points was applied on the $g_{11}^{(1)}$ curve to increase precision. The delay was selected post hoc to optimize the accuracy. The diffusion coefficient needed for this method was measured by fitting $g_{11}^{(1)}$ in the absence of flow and extracting the value from the fit coefficients. To measure v_{tot}, another moving average of 11 points was first applied on $\Delta\eta$ before calculating v_x and v_y with Eq. 6.19, which also improved precision. The calculated v_x, v_y and v_z were then summed to obtain v_{tot}.

The expected flow velocity in the tube (v_{th}) was calculated from the known inner diameter of the tube and the pump-controlled volumetric flow velocity, assuming laminar flow resulting in a parabolic distribution of the flow speed from the center [168]. We compared the accuracy of the measurements of the different methods by calculating the root mean square error (RMSE). For the two existing methods, the RMSE was calculated over 1 mm in the center of the tube to avoid erroneous contributions of the tube edges. Due to image overlap and

limited SNR, Ch2 and Ch3 were imaged sequentially instead of simultaneously, as for the calibration measurements. Ch1 was recorded in both of these measurements to calculate the simultaneous cross-correlations. Only the first measurement was used for v_{sp} and v_{fit}.

6.3.4 B-scan

The flow speed was quantified with 200 B-scans, similar to the previous section. Scans were acquired at 200 Hz and consisted of 500 A-lines covering roughly a region of 1.6 mm. Thus, the shortest delay between two A-lines acquired at the same position was 5 ms. Using this delay prevented the estimation of v_{fit} as curve fitting required multiple points along the correlation curve, and given the long minimum delay, most points were entirely decorrelated and thus did not contribute to the fit. For the same reason, a moving average was not used to calculate v_{sp} or v_{tot}. Both variables were measured with $\tau = 5$ ms. The noise floor was corrected as in the previous section. The average speed versus depth was calculated over 11 A-lines in the center of the tube to facilitate comparison.

Previously, we calculated correlation by comparing a single pixel in the A-line over time. Here, given a 2D image in time, we correlated a 3×3 pixels in time, providing higher accuracy at the cost of diminished spatial resolution. Furthermore, to highlight only the region with flow, two conditions were applied: the SNR had to be higher than 2 and $g_{11}^{(1)} > 0.1$. These restrictions allowed the quantification of flow measurement in the absence of a sample or where the signal decorrelated too rapidly. The velocity was measured at $\theta = 90°$, corresponding to the fast scanning axis, and was measured both without and with a tilt at the same angle as before (i.e., $\phi = 15°$).

6.4 Results

Figure 6.3 shows the experimental (top row, a-c) and theoretical (bottom row, d-f) auto- and cross-correlation images between OCT channels. Figure 6.3 (a) shows the experimental first-order auto-correlation of Ch1, while (b) and (c) show the cross-correlations of Ch1 with Ch2 and Ch3, respectively. This pattern is repeated for theoretical values in Figure 6.3 (d) to (f). Minor differences in the experimental shape and background level are observed, but overall the system acts as theorized. These small discrepancies are primarily due to imperfections of the custom-built MSPL.

Figure 6.4 presents the experimental cross-correlation and auto-correlation ratios obtained for a static object. Fig. 6.4(a-b) shows the ratios $\eta_{12/11}$ and $\eta_{13/11}$, respectively. In Figure 6.4 (d-e), the offset d was subtracted using Eq. 6.18 to produce $\Delta\eta_{12/11}$ and $\Delta\eta_{13/11}$

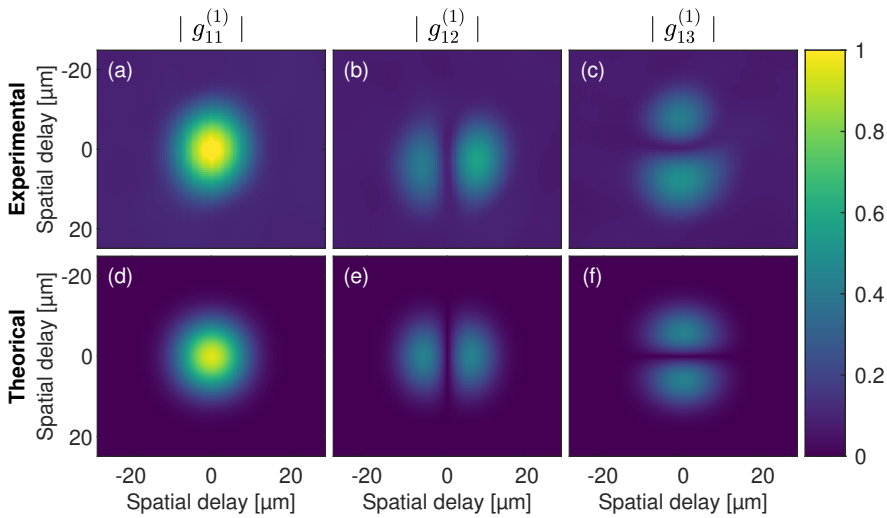

Figure 6.3 Speckle correlation of an en-face image of a piece of plastic. The auto-correlation amplitude of Ch1 is shown in (a), while the cross-correlation amplitude of Ch1 and Ch2, and Ch1 and Ch3 are shown in (b-c), respectively. The second row (d-f) shows the respective theoretical values.

images showing the linear trend between correlation ratios and delays. Figure 6.4 (f) shows $\Delta\eta_{\text{tot}}$. As expected, it produces a cone with linearity highlighted in the two orthogonal sections showed in Figure 6.4 (c). The minor astigmatism observed in Figure 6.4 (c) was taken into account when calculating v_x and v_y. Random fluctuations on the contour are due to low correlation values in those regions, as seen in Fig. 6.3. The fluctuations are present only where the correlation is close to 0, and thus measurements for such displacement are inaccurate. Compared to ratios η (Fig. 6.4(a–b)), the variation of ratios $\Delta\eta$ (Fig. 6.4 (d–e)) shows increased linearity, suggesting that the latter is more suitable for flow measurement.

Figure 6.5 shows comparisons between the measurement of laminar flow in a plastic tube at different speeds and angles using our approach (v_{tot}, blue crosses) and the existing techniques described previously (v_{sp} and v_{fit} in red and orange dots, respectively). The pump flow speeds in the center of the tube are 0.0 mm/s for sub-figures (a-d), 0.9 mm/s for (e-h), 2.7 mm/s for (i-l), 9.0 mm/s for (m-p), and 36.0 mm/s for (q-t). The flows measured by the techniques were shown for transverse angles of $\theta = 0°$ (column 1), $\theta = 30°$ (column 2), $\theta = 60°$ (column 2), and $\theta = 90°$ (column 4). An angle of $\theta = 0°$ corresponds to a flow in the x axis, as illustrated in Fig. 6.2. Meanwhile, there is no axial tilt (i.e. $\varphi = 0$). The solid black curve shows the expected flow speed. Two discrepancies are observed with the v_{fit} technique (yellow curve): in Fig. 6.5(m), flow measurement inaccuracy is observed for high values, while in Fig. 6.5 d), no flow was recorded. We hypothesize a pump and an algorithm

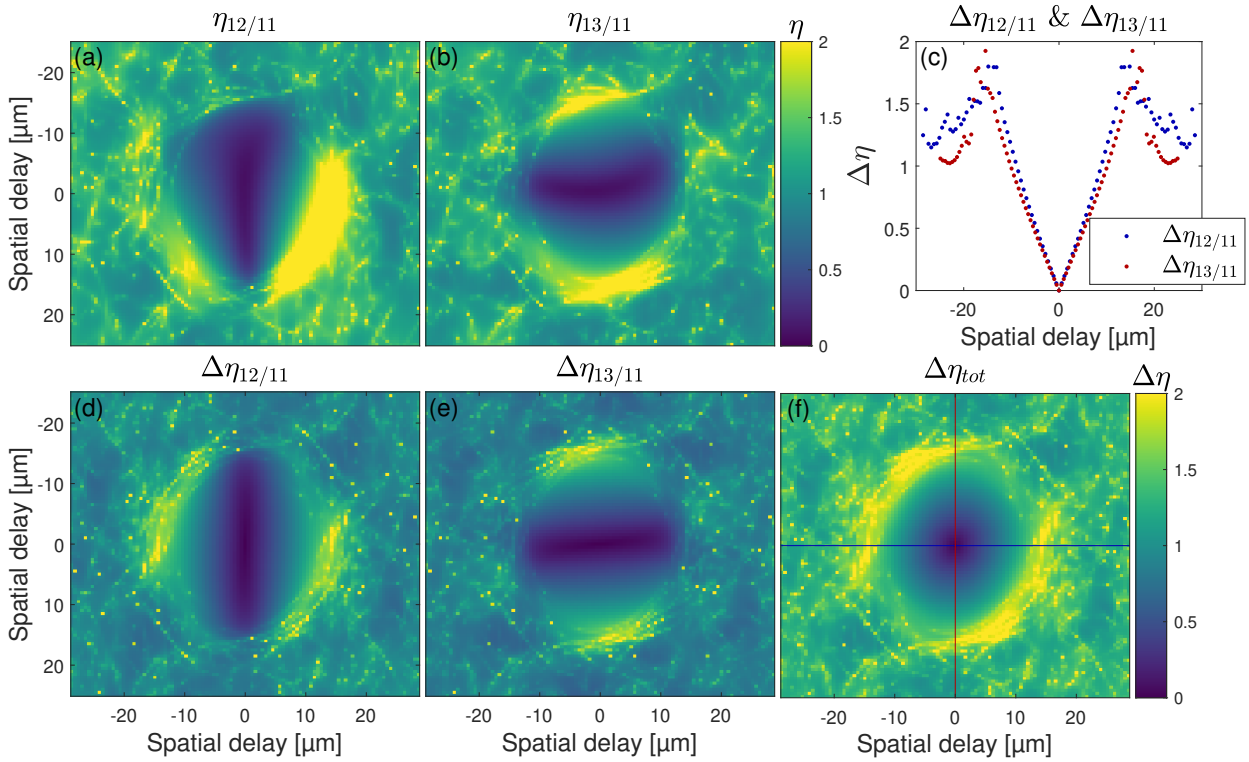

Figure 6.4 Experimental cross-correlation and auto-correlation ratios for (a) $\eta_{12/11}$, and (b) $\eta_{13/11}$ obtained for a static object. Ratio variations for (d) $\Delta\eta_{12/11}$, and (e) $\Delta\eta_{13/11}$, and their combination (f) $\Delta\eta_{\text{tot}}$. Subfigure (c) plots cross-sections of $\Delta\eta_{\text{tot}}$ shown in (f).

failure, respectively. Table 6.1 compiles the RMSE of flow speeds measured in Fig. 6.5. Our method shows increased accuracy (i.e. lower RMSE) for all flow speeds.

Table 6.1 Root-mean-square error (RMSE) of flow speed measurements (v_{tot} compared to previous published techniques (v_{sp} and v_{fit}) for the flow speeds used in Fig. 6.5.

	max speed [mm/s]:	0.0	0.9	2.7	9.0	36.0
RMSE	v_{tot}	0.22	0.14	0.43	1.13	3.99
	v_{sp}	0.97	0.48	0.61	4.17	5.19
	v_{fit}	1.20	0.86	0.84	4.63	10.2

Figure 6.6 shows comparisons between the measurement of laminar flow in a plastic tube in the presence of an effective $\varphi = 10°$ axial tilt to quantify the effects of AGV. Flow measurements were performed at different speeds and at a transverse angle $\theta = 90°$using our approach (v_{tot}, blue crosses) and the existing techniques described previously (v_{sp} and v_{fit} in red and orange dots, respectively). Figure. 6.6 shows overestimated flow speeds generated by v_{sp} and v_{tot} compared to the planar case, particularly for (d-e). Table 6.2 shows the RMSE

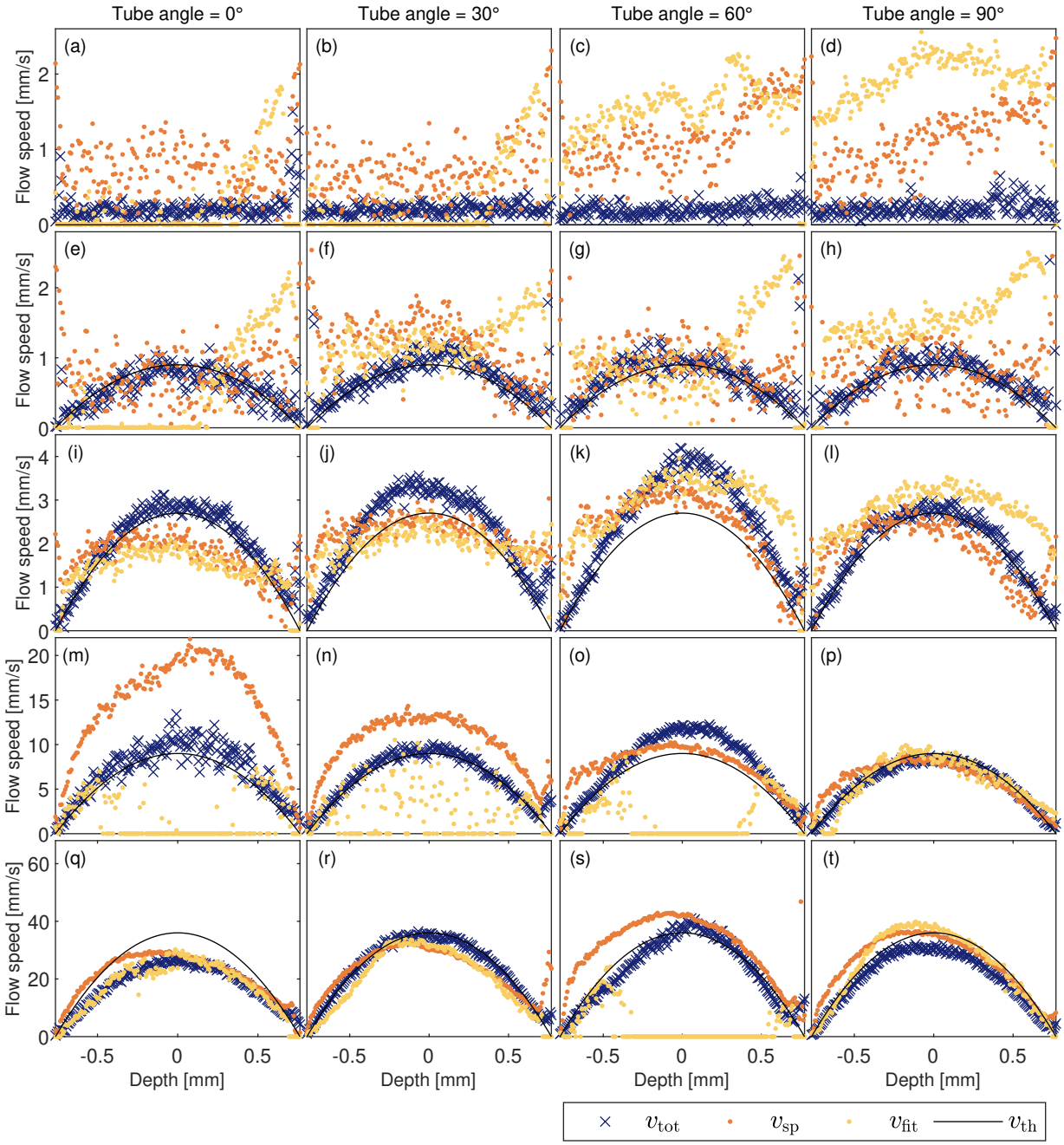

Figure 6.5 Laminar flow as measured by v_{tot} (blue crosses), v_{fit} (orange dots), and v_{sp} (yellow dots) as compared to theoretical values (solid black curve) at $\theta = 0°$ (column 1), $\theta = 30°$ (column 2), $\theta = 60°$ (column 3), and $\theta = 90°$ (column 4), and for flow speeds of 0.0 mm/s (a–d), 0.9 mm/s (e–h), 2.7 mm/s (i–l), 9.0 mm/s (m–p) and 36 mm/s (q–t).

of flow speeds measured in Fig. 6.6 in the presence of an axial tilt ($\phi = 10°$). The correlation ratio method was shown to be more accurate (except at 12.6 mm/s in comparison to v_{fit}).

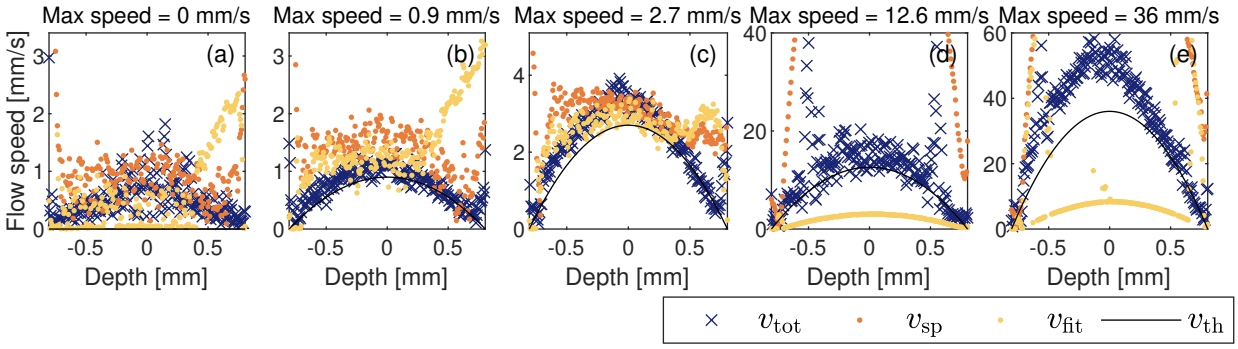

Figure 6.6 Laminar flow as measured by v_{tot} (blue crosses), v_{fit} (orange dots), and v_{sp} (yellow dots) as compared to theoretical values (solid black curve) at the center of the tube for speeds of 0.0 mm/s (a), 0.9 mm/s (b), 2.7 mm/s (c), 9.0 mm/s (d), and 36 mm/s (e) with an effective axial tilt of ϕ =10°.

Table 6.2 Root-mean-square error (RMSE) of flow measurements with a tilt angle $\phi = 10°$ (v_{tot}) compared to previously published techniques (v_{sp} and v_{fit}) for the flow speeds used in Fig. 6.6.

	max speed [mm/s]:	0.0	0.9	2.7	12.6	36
RMSE	v_{tot}	0.61	0.18	0.53	8.37	13.4
	v_{sp}	0.91	0.76	1.12	57.2	103
	v_{fit}	0.89	1.06	0.97	7.31	24.1

Figure 6.7 (a) and (b) summarize the not tilted (Fig.. 6.5) and tilted cases (Fig. 6.6), respectively, by plotting the measured velocities as a function of the expected velocities. Blue dots represent our approach (v_{tot}), while the existing techniques described previously (v_{sp} and v_{fit}) are depicted by red and orange dots, respectively. The black line shows a perfect match with the expected flow speed. To visualize all scales of flow speed, the figure is plotted on a log scale; therefore, flow speeds of zero are excluded.

Figure 6.8 shows the standard deviation of the flow speed measurements for an integration time of 50 ms at varying speeds (a) and in 21 pixels at the center region of the tube for a flow speed of 3 mm/s for varying integration times for v_{tot} (blue), v_{fit} (orange), and v_{sp} (yellow).

Figure 6.9(a-d) shows individual flow velocity components, including the axial z-direction (dark blue), transverse x-direction (light blue), and y-direction (medium blue). The total flow speed measured is also displayed (v_{tot}, blue crosses) with the expected total flow speed in a solid black line (v_{th}). From these components, the orientation is calculated and shown in Figure 6.9(e-h) with the measured angle (green dots) as well as its average value (dark green dotted line). The measured difference from the expected angle is shown in (i) for all

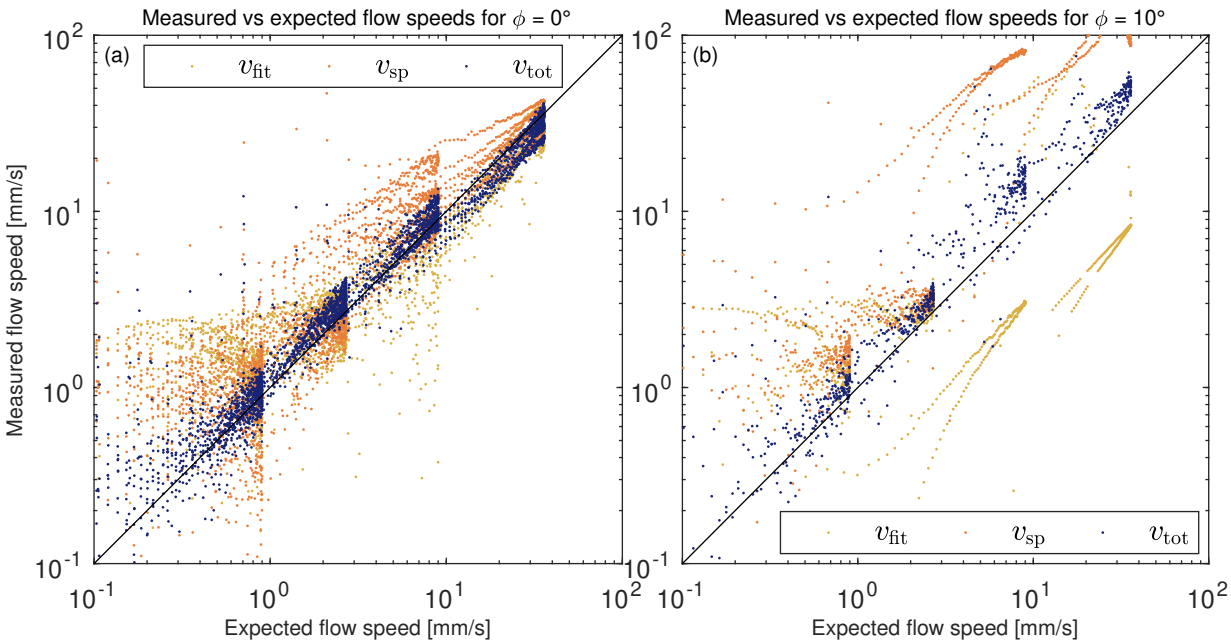

Figure 6.7 Laminar flow as measured by v_{tot} (blue dots), v_{fit} (orange dots), and v_{sp} (yellow dots) as compared to theoretical values (solid black curve) without an axial tilt (a) and with an effective axial tilt of ϕ =10° (b).

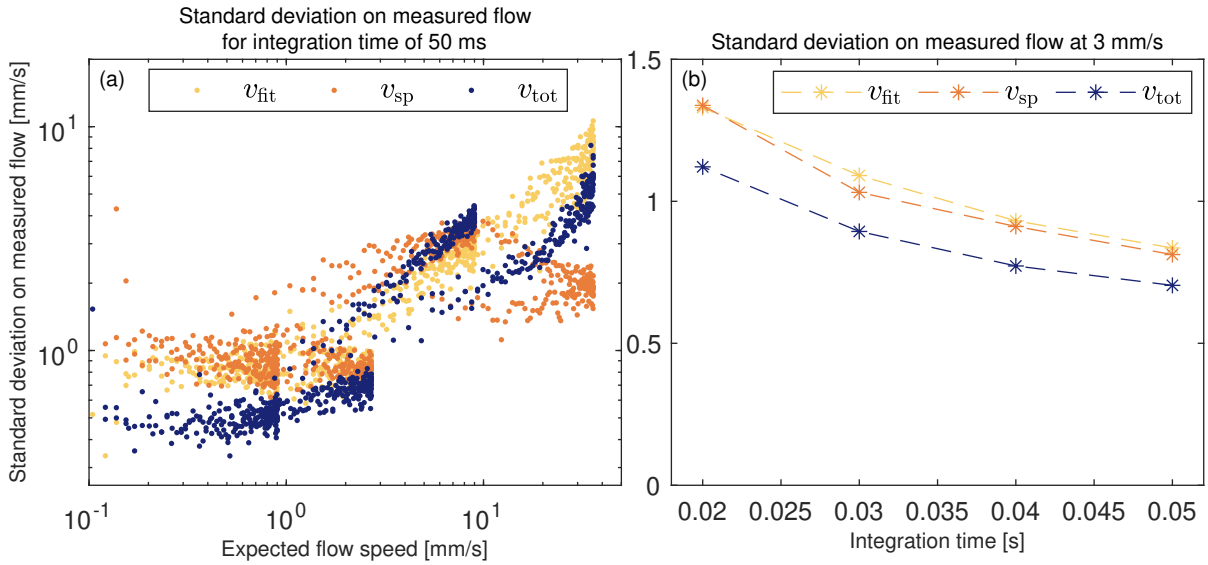

Figure 6.8 Standard deviation on laminar flow measurements done by v_{tot} (blue), v_{fit} (orange), and v_{sp} (yellow) for varying expected flow speed and an integration time of 50 ms (a) and for an expected flow speed of 3 mm/s and varying integration times.

measurements from Fig. 6.5.

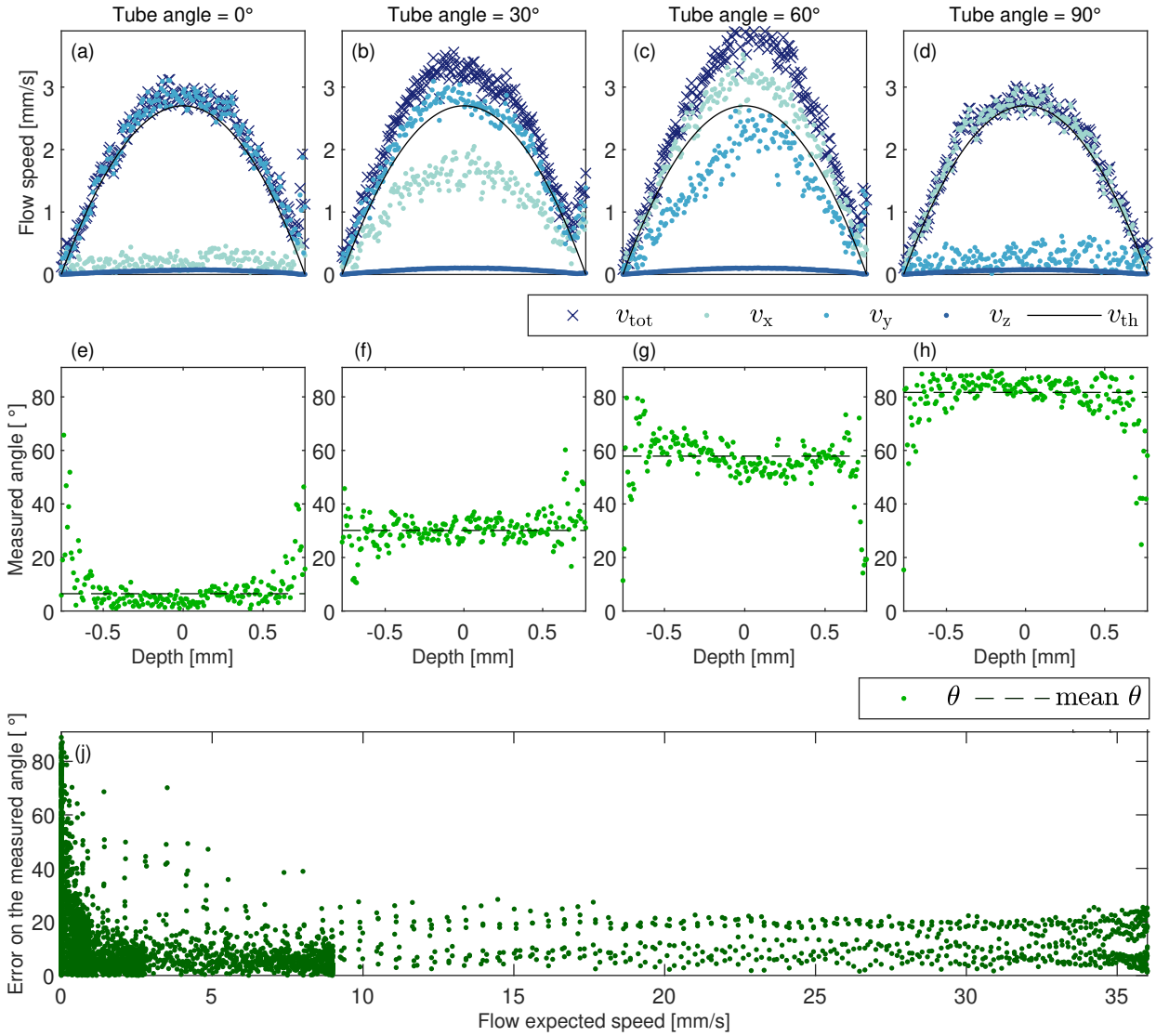

Figure 6.9 Laminar flow as measured by the correlation ratio method in the x (light blue dots), y (blue dots) and z (dark blue dots) axes for transverse flow orientations of $\theta = 0°$ (a), $\theta = 30°$ (b), $\theta = 60°$ (c), and $\theta = 90°$ (d), with v_{tot} (blue crosses) and expected flow speed (solid black line). The corresponding measured angle is shown below in (e–h) respectively. The absolute difference from the expected angles is shown in (i) for all measures made in Fig. 6.5.

Figure 6.10 shows B-scans of flow speeds of the tube measured using v_{tot} (a-d) v_{sp} (e-h). Figure 6.10 (i-l) displays flow speeds in the vertical section at the center of the B-scan measured by v_{tot} (dark blue) and v_{sp} (orange), as well as the expected value (v_{th}, solid black line). The flow speed is displayed for a maximum pump flow speed at the center of the tube

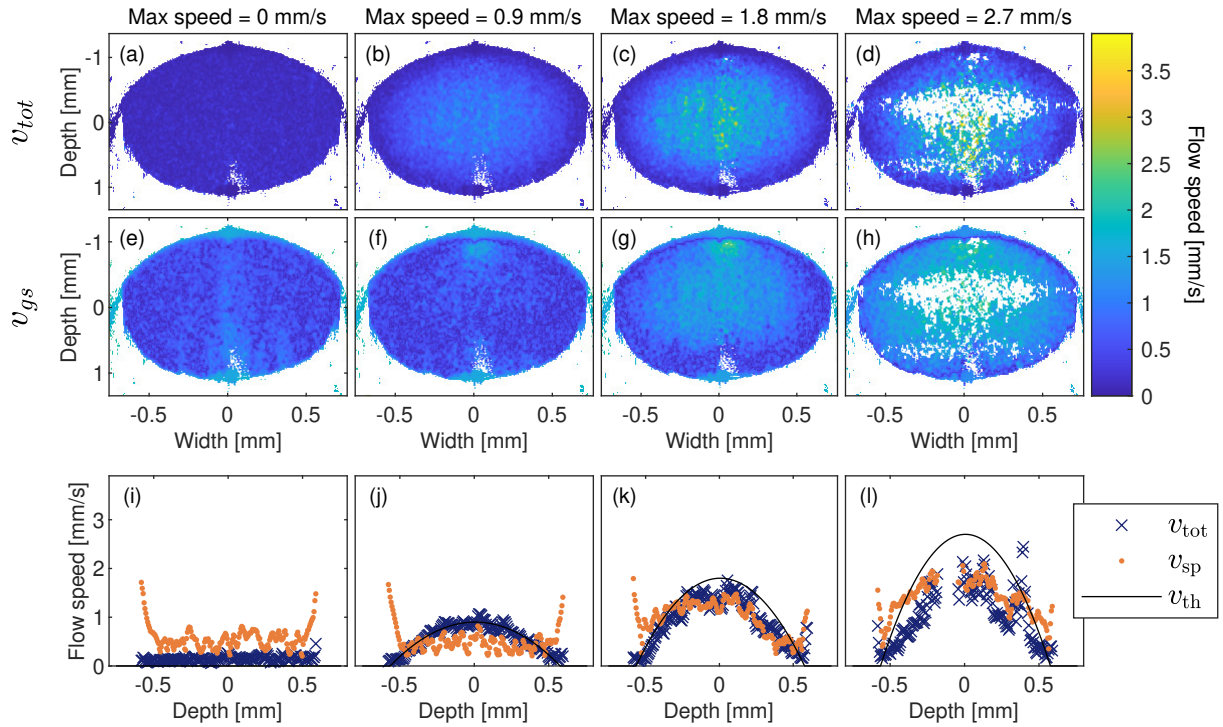

Figure 6.10 Laminar flow measured in a tube by v_{tot} (a-d) compared to v_{sp} (e-h) for flow speed of 0 mm/s (column 1), 0.9 mm/s (column 2), 1.8 mm/s (column 3) and 2.7 mm/s (column 4). The flow in the vertical axis of the tube is displayed in (i-l) with v_{tot} (blue), v_{sp} (orange), and the expected result (black solid line).

of 0 mm/s (column 1), 0.9 mm/s (column 2), 1.8 mm/s (column 3) and 2.7 mm/s (column 4). The white regions correspond to situations where either the flow could not be measured due to poor SNR (SNR < 2) or complete B-scans decorrelation ($g_{11}^{(1)} < 0.1$). Given a delay of 0.005 seconds between each B-scan, the maximum measurable speed was 1.8 mm/s. The correlation ratio method is more accurate on the edges, where the flow speed is lower.

Figure 6.11 shows similar flow speed measurements than Figure 6.10 but with the tube tilted axially at an effective angle of $\phi = 10°$. Again, (a-d) shows flow speed as measured by v_{tot} compared to (e-h), where v_{sp} is used, and (i-l) displays the flow speed in the center of the tube compared to the expected result in black. The results for both methods are less accurate than with no tilt.

6.5 Discussion

We have demonstrated a novel method for measuring transverse flow by exploiting the OCT signal obtained from three channels of an MSPL: the different channels resulting in distinct

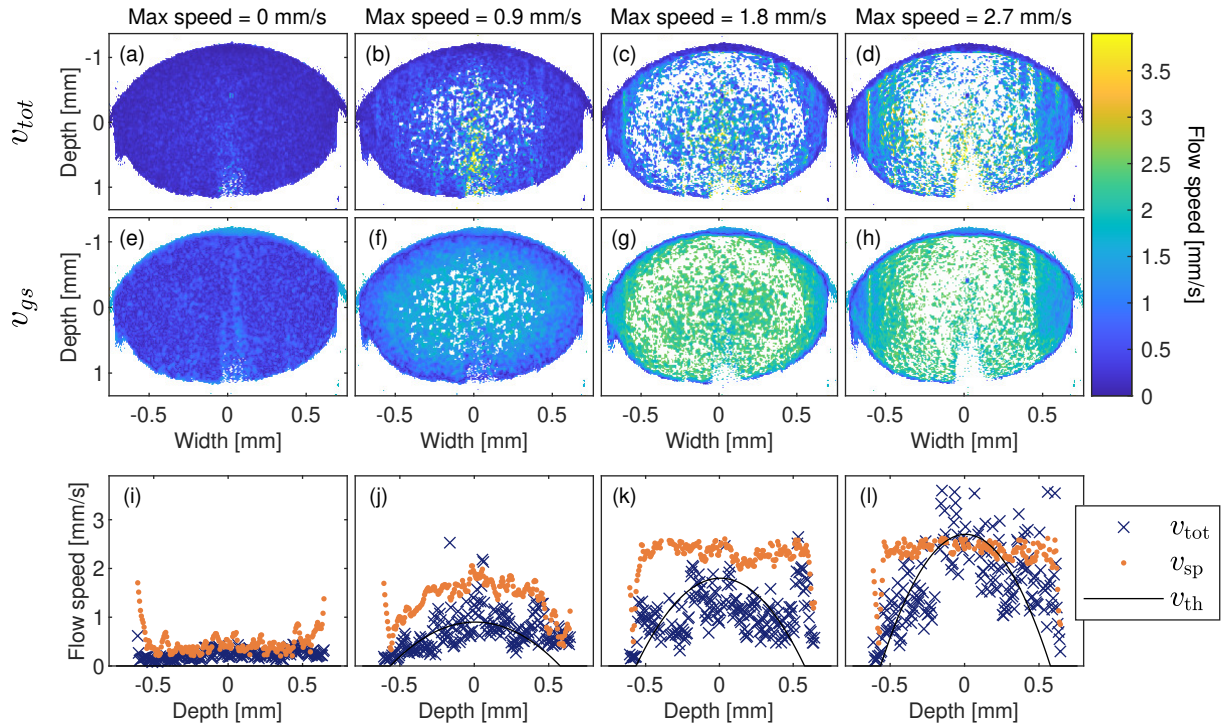

Figure 6.11 Laminar flow measured in a tube by v_{tot} (a-d) compared to using v_{sp} (e-h) for flow speed at the center of 0 mm/s (a,e,i), 0.9 mm/s (b,f,j), 1.8 mm/s (c,g,k) and 2.7 mm/s (d,h,l). The tube was tilted by an effective angle of $\phi = 10$ °. The flow in the center axis of the tube is displayed in (i-l) with v_{tot} (blue), v_{sp} (orange), and the expected result (black solid line).

CSFs. The method uses the ratios between the cross-correlation of Ch1 with either Ch2 or Ch3 and the autocorrelation of Ch1. This approach results in a linear relation between the measured ratio and the transverse component of the measured flow speed, providing more accurate measurements without a priori assumption on the diffusion coefficient value. Furthermore, the method gives information on the angle of the transverse orientation of the flow, which would allow for direct measurement of blood flow orientation.

In the following paragraphs, experimental results are further discussed. Figure 6.3 (a–c) shows higher background correlation than its theoretical values (d–f), which could either originate from the phase stabilization method [10], or from the statistical noise when calculating correlation around $\tau = 0$. As described in Sec. 6.3.2, the correlation map were first calculated for each depth and the absolute value was then averaged axially. Any negative correlation value would thus be considered as positive and created the observed background signal.

Figure 6.6 shows how accurately measuring flow with an axial tilt is much more challenging.

This technical difficulty can be due to the faster decorrelation rates caused by the AGV and the statistical noise due to the lower correlation values. However, the local overestimation of v_{tot} in (d) at depths around -0.5 mm and 0.5 mm greatly increased the RMSE, and remains unexplained. The slight overestimation in (e) seems to match the deviation observed in Fig. 6.5 and might be explained by pump instabilities. The underestimation of v_{fit} in Fig. 6.6(d-e) is due to the algorithm's inability to fit the correlation curve and return a null flow in the x and y directions. Speed is partially measured since the Doppler effect contributes to the axial direction speed flow, although some bias due to the AGV is expected [10]. Furthermore, contrary to Fig. 6.5 (a–d), some flow was detected at a pump flow speed of 0 mm/s, possibly due to a minor leak in the pumping circuit. There is no reason why a tilt in the tubing should affect flow measurement when there is no flow. Nevertheless, Fig. 6.7 highlights how our proposed method is more accurate, particularly at lower flow speeds and in the presence of an axial tilt.

Figure 6.8 (a) shows that the uncertainty decreases for lower flow speeds, allowing distinguishing small velocities from static tissues. Furthermore, as expected, precision increases inversely with longer integration times, but the exact order of the relation has yet to be determined.

Figure 6.11 highlights again challenge associated with measuring tilted flow. The maximum measurable speed decreases because of the signal decorrelating much faster due to AGV. Interestingly, Fig. 6.11 (c,g) show a white ring for which flow cannot be measured, likely resulting from higher AGV values close to the edges. At the tube's extremity, despite the AGV being at its highest value, since the flow is low, the signal does not decorrelate as fast as in the white ring region, and flow remains measurable.

The method has two fundamental advantages. Firstly, the linear relationship between speed and the correlation ratio (i.e., Eq. 6.19) allows very low values of flow to be measurable, even while using small values of τ. Secondly, using the ratio causes cancellations of artifacts impacting both channels, such as diffusion axial motions, or laser instabilities. A delay as short as the A-line period can be used, opening the door to new scanning strategies for flow measurements.

In this work, we used different scanning strategies. The first consisted of taking multiple A-lines at the same position, allowing for the measurement of faster flow speeds from the smaller τ value. However, measuring an entire B-scan or C-scan in such a way would take a long time. Alternatively, A-lines were also correlated from one B-scan to the next. This allowed us to measure the flow on an entire B-scan in the time it would take for a single A-line, which greatly reduced the acquisition time. However, this has resulted in a decreased maximum

measurable flow speed. Here, a 200 Hz scan rate resulted in a measurable maximum flow speed of ≈2 mm/s. Higher flow speed would necessitate a faster scanning system or a larger beam waist to avoid scatterers exiting the image field-of-view by the time of the next B-scan.

While a linear relationship was assumed in this work, a third-degree polynomial would have been slightly more accurate. Inspection of Fig. 6.4 (c) reveals that a third-degree polynomial or a look-up table could have improved the accuracy.

This approach has limitations. Like other correlation methods, the correlation ratio approach still lacks precision, requiring significant integration times to be precise. The statistical nature of correlation requires multiple independent measurements to converge towards the expected value. However, this technique was more precise than previously published methods for lower flow speeds [62, 64, 147].

Some issues were observed with the phase stabilization of our system. The issue was highlighted by comparing second-order correlation function ($g^{(2)}$) to the first-order correlation function ($g^{(1)}$). Light intensity is used to calculate $g^{(2)}$, and thus, the phase is unnecessary. Both correlations may be compared using the Siegert relation: $g^{(2)} = |g^{(1)}|^2 + 1$ [169]. Since $g^{(1)}$ decorrelated much faster, we hypothesize some phase instability originating from the laser source.

Phase instabilities highlighted how the correlation ratio method was more robust regarding phase disturbances. Since the phase instabilities affect $g_{11}^{(1)}$ and $g_{12}^{(1)}$ in the same way, calculating the ratio removed the error originating from phase instabilities. Such issues mainly occured when calculating v_{sp} and v_{fit}.

Moreover, the absolute value in Eq. 6.19 prevents disambiguation of the velocity direction, i.e., the left or right direction of the flow cannot be distinguished. As a consequence, negative and positive angles could not be differentiated. Indeed, for $|v_x| = |v_y|$, two flow direction exist: 45° or -45°. This also explains why in Fig. 6.9 (e, h), the measured angles were overestimated and underestimated, respectively. In this case, a 94° angle could be measured as 86°, leading to an underestimation. Something similar happened for the 0° angle but with negative angles being measured as positive. Figure 6.5 (e–h) also shows higher inaccuracies at the edges of the tube where flow speed approaches 0. Fig. 6.9 (i) illustrates it better in showing how the error increases as the flow speed goes below 1 mm/s. Theoretically, in Eq. 19, the phase variation inside the modulus operator should be indicative of the flow direction (left or right), but experiments contradict this. More work is needed to understand why and achieve complete measurement of flow direction.

From an experimental point of view, the most significant limitation originated from the

reliability of the syringe pump, in which friction varied over time. While the pump provided reliable flows in initial experiments, it became less reliable as experiments went on.

The technique presented in this paper faces similar difficulties to other correlation-based methods already used in ophthalmology, from which solutions may be leveraged. Future work involves implementing the method for in vivo imaging and solving associated challenges. For instance, lower SNR is expected in vivo; however, previous work has shown that correlation measurements are accurate at very low SNRs [138]. While this method has not yet been tested using blood, previous work has shown that the shape of diffusers does not impact measurements [73], and our own approach intrinsically compensates for diffusion. Bulk-tissue motion, however, is a challenge, but one that has already been addressed in other works [167, 170–173]. The method was successful in measuring flow through more than 1 mm of moving scatterers, but it remains to be seen whether this depth is enough for ophthalmology.

Measuring flow speeds higher than those demonstrated here is a challenge. Increasing scanning speeds, both spatially and spectrally, is a possible solution to expanding the range of measured velocities. Alternatively, using a coarser resolution could increase the maximum measurable speed as w_{xy} is related to how fast the signal decorrelates. Indeed, using an M-mode approach permits the measurement of higher velocities in a single region, as it allows for shorter delay values. Since the minimum possible delay would be 500 times shorter than for the B-scan case, we could expect 500 times faster ($\approx$1 m/s) measurable flows.

The biggest unknown is how the anatomical shape and the small size of the capillaries will affect measurement accuracy. Furthermore, the impact of varying flow speeds in arteries due to heartbeats is unknown and needs to be investigated. Theoretically, the measurement should return the average flow speed during the integration time.

While the MSPL holding an alignment was currently tricky in this work, another group [56] has successfully managed to splice the lantern tip to conventional connectors, removing the issue.

Furthermore, the analysis for AGV was limited to a single axial angle and only for a gradient in the axial direction. However, the higher accuracy on the sides of the tube in Fig. 6.11 suggests that our method is more robust for gradients in transverse directions. Further studies, both experimental and theoretical, are needed to determine with more accuracy how it affects our method.

6.6 Conclusion

In this work, we proposed a novel method for measuring flow speed using the ratios between the cross-correlation and auto-correlation of the signal acquired from two distinct CSFs through the use of a modally-specific photonic lantern. The method proved to be more accurate, particularly at low speeds, distinguishing flows as slow as 0.5 mm/s from static ones for 1 second integration time. The technique was less sensitive to errors induced by AGV in the axial component of the flow speed and did not require prior knowledge of the diffusion coefficient. Furthermore, our approach could measure the transverse angle of the flow direction, allowing, when combined with Doppler OCT, the knowledge of the 3D flow orientation.

The mathematical framework presented in this work could also be extended to other CSFs as demonstrated in a previous study [11]. Alternatively, such CSFs could be numerically assessed in the same way deconvolution can change a system's CSF. For example, an image could be digitally shifted in the axial direction to artificially create a CSF similar to $h_{xy}(x, y)|_{\mathrm{Ch2}}$. The proposed ratio method could then be used to measure the axial component of the flow. More interestingly, the approach could be extended to full-field imaging devices, where the image is manipulated numerically to create an alternate CSF.

Funding

This work was supported by the Natural Sciences and Engineering Research Council of Canada (NSERC) grant #RGPIN-2018-06151 (to C.B.) as well as financial support from the TransMedTech Institute (to R.M.T). This research was conducted as part of the TransMedTech Institute's activities and thanks, in part, to funding from the Canada First Research Excellence Fund.

Acknowledgements

The authors thank Castor Optics, inc. for supplying a MSPL prototype.

Disclosures

C.B.: Castor Optics, inc. (I,P). R.M.-T. : (P). The other authors have no conflicts of interest to disclose.

Data Availability

Imaging datasets acquired in this work are not publicly available at this time, but may be obtained from the authors upon reasonable request.

CHAPTER 7 GENERAL DISCUSSION

As outlined in Chapter 1, this thesis explored the feasibility and potential applications of FM-OCT. Several innovations were developed that were not included in the publications of Chapters 3, 4, and 6. This section presents both promising and inconclusive avenues, along with clarifications and commentary on the broader impact of the work.

7.1 Flow measurement alternatives

Research on flow measurement was ongoing, with continual innovations emerging throughout the course of this project. The following section introduces alternative methods to the flow measurement technique described in Chapter 6 and addresses questions that remain partially unresolved.

7.1.1 Using second-order correlation

The approach outlined in Chapter 6 could, in principle, be implemented using second-order rather than first-order correlations. This modification would eliminate the requirement for a phase-stable system, thereby simplifying practical implementation. However, the use of $g^{(2)}$ would necessitate twice the integration time to achieve comparable accuracy.

A key challenge in this implementation is the error term d in Eq. 6.17, which cannot be readily subtracted. By applying the Siegert relation ($g^{(2)} = |g^{(1)}|^2 + 1$) [169] and Eq. 6.14, the expression for $g_{12}^{(2)}$ becomes:

$$\begin{aligned} g_{12}^{(2)}(\tau) =& |g_{12}^{(1)}(\tau)|^2 + |g_{12}^{(1)}(\tau)|\frac{a}{2}\cos(\theta) + a^2 + 1, \text{ and} \\ g_{13}^{(2)}(\tau) =& |g_{13}^{(1)}(\tau)|^2 + |g_{13}^{(1)}(\tau)|\frac{a}{2}\cos(\theta) + a^2 + 1, \end{aligned} \tag{7.1}$$

where a and θ arise from the unknown complex offset $d = ae^{i\theta}$ in Eq. 6.17. This offset can be removed as follows:

$$\begin{aligned} g_{12}^{*(2)}(\tau) =& \frac{g_{12}^{(2)}(\tau) + g_{12}^{(2)}(-\tau)}{2} - g_{12}^{(2)}(0) + 1, \text{ and} \\ g_{13}^{*(2)}(\tau) =& \frac{g_{13}^{(2)}(\tau) + g_{13}^{(2)}(-\tau)}{2} - g_{13}^{(2)}(0) + 1, \end{aligned} \tag{7.2}$$

where $g_{12}^{*(2)}(\tau)$ and $g_{13}^{*(2)}(\tau)$ represent the corresponding correlations without the random offset

d. Here, it is assumed that d is independent of τ. The correlation ratios with the offset removed can then be calculated as:

$$\begin{aligned}\eta^*_{12/11}(\tau) =& \sqrt{\frac{g^{*(2)}_{12}(\tau)-1}{g^{(2)}_{11}(\tau)-1}} = 1.41\frac{v_x\tau}{w_{xy}}\exp\left[-0.04\frac{(v_x^2+v_y^2)\tau^2}{w_{xy}^2}\right], \text{ and} \\ \eta^*_{13/11}(\tau) =& \sqrt{\frac{g^{*(2)}_{13}(\tau)-1}{g^{(2)}_{11}(\tau)-1}} = 1.41\frac{v_y\tau}{w_{xy}}\exp\left[-0.04\frac{(v_x^2+v_y^2)\tau^2}{w_{xy}^2}\right].\end{aligned} \tag{7.3}$$

The flow speed can then be estimated as:

$$\begin{aligned}v_x =& \frac{w_{xy}}{1.41\cdot\tau}\eta^*_{12/11(\tau)}, \text{ and} \\ v_y =& \frac{w_{xy}}{1.41\cdot\tau}\eta^*_{13/11(\tau)}.\end{aligned} \tag{7.4}$$

Further work is required to evaluate the efficacy of this approach and to compare its performance with existing methods.

7.1.2 Flow direction

As discussed in Chapter 6, the correlation ratio method provides only partial information regarding flow direction; specifically, the signs of v_x and v_y cannot be determined. However, in theory, the phase variation of $\eta_{12/11}$ and $\eta_{13/11}$ should encode precise information about the direction of flow.

Figure 7.1 presents the phase values of the different first-order correlations and correlation ratios for a static sample. This figure corresponds to Fig. 6.3 and Fig. 6.4 from Chapter 6, but with phase values depicted in rows 2 to 4 instead of amplitude. Notably, the last row, which displays $\angle\Delta\eta_{12/11}$ and $\angle\Delta\eta_{13/11}$, reveals a clear distinction in phase values depending on the side of the spatial delay. In principle, this distinction could be leveraged to determine the exact orientation of the flow.

However, when applied to flow measurements, this approach does not yield the expected results. Figure 7.2 displays $\angle\Delta\eta_{12/11}$ measurements for milk flowing through a cylindrical tube at a maximum speed of 9 mm/s. The left panel shows results for two different depth positions and multiple values of τ, while the right panel presents data across all depths for a single value of τ. The flow orientation was set in the x direction, corresponding to the direction measured by $\Delta\eta_{12/11}$. These datasets are identical to those presented in Chapter 6.

As illustrated in Figure 7.2, the phase variation appears random in the presence of flow. On the left, two regions in close proximity display phase flips at zero delay, but in opposite

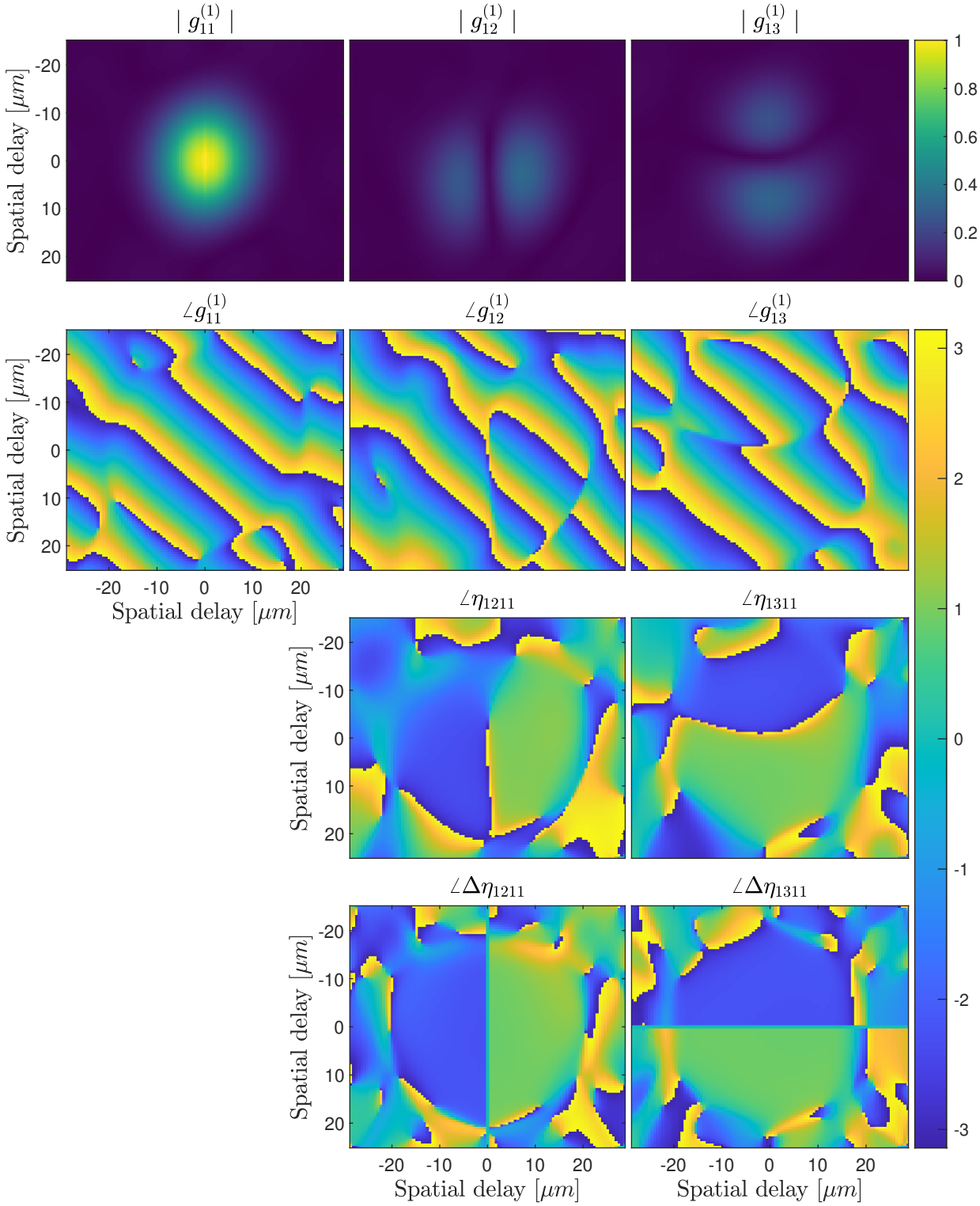

Figure 7.1 First-order correlations and correlation ratios for a static sample. The first row displays the absolute values of $g_{11}^{(1)}$, $g_{12}^{(1)}$, and $g_{13}^{(1)}$, while the second row presents their corresponding phase values. The third and fourth rows show the phase values of $\eta_{12/11}$ and $\eta_{13/11}$, and $\Delta\eta_{12/11}$ and $\Delta\eta_{13/11}$, respectively.

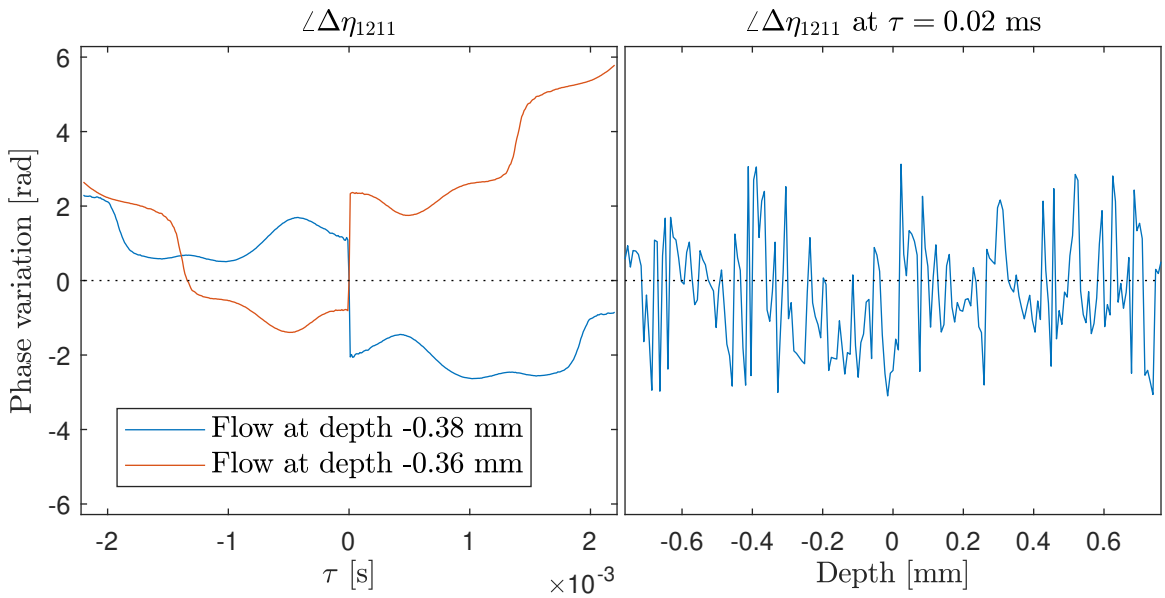

Figure 7.2 Phase values of $\Delta\eta_{12/11}$ measured on flowing milk in a cylindrical tube at a maximum speed of 9 mm/s. The left panel illustrates results for two depth positions and multiple values of τ; the right panel aggregates data across all depths for a single value of τ.

directions, despite sharing the same flow direction. The right panel further demonstrates that phase values are random and do not provide reliable information about flow direction. The underlying cause of this phenomenon remains unclear and warrants further investigation.

7.1.3 Correlation ratio without photonic lantern

The flow measurement project underwent continual development, with new innovations emerging throughout its course, resulting in the delayed publication of the correlation ratio findings. Progress continued beyond the writing of the original manuscript and this thesis. Notably, the publication in Chapter 6 asserted that an MSPL is not strictly necessary for the application of correlation ratios; alternative approaches might achieve comparable results. The following section presents how such an alternative could be possible.

The central idea is to synthetically recreate the CSF observed in Channels 2 and 3. For instance, in Chapter 6, the LP11 mode was approximated as a Gaussian multiplied by a

linear term; here, it is instead represented as the difference between two Gaussian functions:

$$\begin{aligned} f_{\mathrm{LP11,h}}(x,y) &\approx \exp\left[-\frac{(x-\kappa)^2+y^2}{w_{xy}^2}\right] - \exp\left[-\frac{(x+\kappa)^2+y^2}{w_{xy}^2}\right] \text{ and} \\ f_{\mathrm{LP11,v}}(x,y) &\approx \exp\left[-\frac{x^2+(y-\kappa)^2}{w_{xy}^2}\right] - \exp\left[-\frac{x^2+(y+\kappa)^2}{w_{xy}^2}\right], \end{aligned} \tag{7.5}$$

where κ is a fitting parameter to be determined and x and y are the two-dimensional position coordinates in the image transversal directions. Channel 2 and 3 CSF can thus be approximated through Channel 1:

$$\begin{aligned} \tilde{h}_{xy}(x,y)\Big|_{\mathrm{Ch2}} &= h_{xy}(x-\mu,y)|_{\mathrm{Ch1}} - h_{xy}(x+\mu,y)|_{\mathrm{Ch1}} \text{ and} \\ \tilde{h}_{xy}(x,y)\Big|_{\mathrm{Ch3}} &= h_{xy}(x,y-\mu)|_{\mathrm{Ch1}} - h_{xy}(x,y+\mu)|_{\mathrm{Ch1}}\,, \end{aligned} \tag{7.6}$$

where μ is an additional parameter subject to optimization. The tilde ($\tilde{}$) denotes that the functions for Channels 2 and 3 are approximated solely from Channel 1. In principle, it should be possible to recreate Channels 2 and 3 using two measurements from Channel 1; however, two practical challenges arise.

Unless the en-face image is acquired simultaneously, as in full-field OCT or related en-face imaging methods, the two Channel 1 measurements will necessarily occur at different times. This temporal offset is suboptimal for time-dependent measurements such as flow. The solution is to ensure that the interval between the two measurements is much shorter than the delay (τ) used in the correlation calculation. For example, flow in the direction of a B-scan can be assessed by using adjacent A-lines within the same B-scan to construct $\tilde{h}xy(x,y)\Big|$ Ch2 or $\tilde{h}xy(x,y)\Big|$ Ch3, and then correlating these with the subsequent B-scan. Although the small delay between adjacent A-lines may introduce a minor error, it is negligible compared to the much larger τ values used in the correlation analysis.

A second challenge is that, in practice, this approach does not yield the expected outcome. Figure 7.3 displays $|g_{1\tilde{2}}^{(1)}|$, the cross-correlation calculated with the recreated Channel 2 for a static sample. The data and methodology are identical to those used in Fig. 6.3, except $\tilde{h}xy(x,y)\Big|$ Ch2 is computed using Eq. 7.6. Rather than reproducing the characteristic two-lobed pattern of Fig. 6.3, the result is an elongated Gaussian profile, as if the two Gaussian components in Eq. 7.6 were added instead of subtracted. The cause of this discrepancy remains under investigation.

However, an alternative workaround exists: instead of subtracting the Channel 1 signal to reconstruct Channel 2 or 3, one can subtract correlations directly. This approach involves

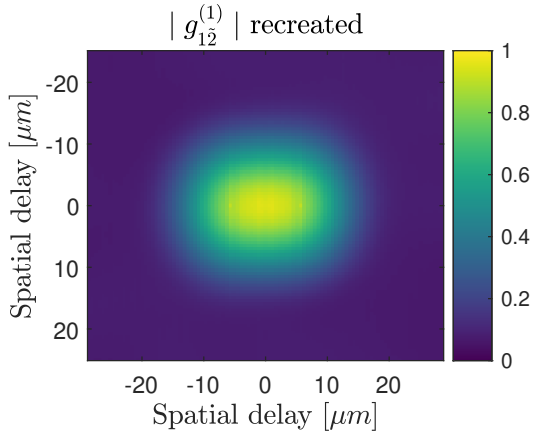

Figure 7.3 Cross-correlation between Channel 1 and the synthetically recreated Channel 2, using Eq. 7.6, for a static object. The data and methodology match those of Fig. 6.3. The result deviates from the expected two-lobed structure, instead displaying an elongated Gaussian profile, the origin of which is still under investigation.

calculating a ratio between the difference of two correlations and an autocorrelation, all derived from the same channel but at different time points:

$$\begin{aligned} \tilde{g}^{(1)}_{12}(\tau) &= \frac{|g^{(1)}_{1\mathrm{L}}(\tau)| - |g^{(1)}_{1\mathrm{R}}(\tau)|}{2} \text{ and} \\ \tilde{g}^{(1)}_{13}(\tau) &= \frac{|g^{(1)}_{1\mathrm{U}}(\tau)| - |g^{(1)}_{1\mathrm{D}}(\tau)|}{2}, \end{aligned} \tag{7.7}$$

where $\tilde{g}^{(1)}_{12}(\tau)$ and $\tilde{g}^{(1)}_{13}(\tau)$ are the recreated $g^{(1)}_{12}(\tau)$ and $g^{(1)}_{13}(\tau)$, respectively, and $g^{(1)}_{1\mathrm{L}}$, $g^{(1)}_{1\mathrm{R}}$, $g^{(1)}_{1\mathrm{U}}$ and $g^{(1)}_{1\mathrm{D}}$ are the correlation between Channel 1 and Channel 1 that has been shifted by μ in a transverse direction left, right, up or down respectively:

$$\begin{aligned} g^{(1)}_{1\mathrm{L}}(\tau) &= \frac{\langle E^*_1(x,y,z,t) \odot E_1(x-\mu,y,z,t+\tau)\rangle}{\sqrt{\langle |E^*_1(x,y,z,t)|^2\rangle \cdot \langle |E_1(x-\mu,y,z,t+\tau)|^2\rangle}}, \\ g^{(1)}_{1\mathrm{R}}(\tau) &= \frac{\langle E^*_1(x,y,z,t) \odot E_1(x+\mu,y,z,t+\tau)\rangle}{\sqrt{\langle |E^*_1(x,y,z,t)|^2\rangle \cdot \langle |E_1(x+\mu,y,z,t+\tau)|^2\rangle}}, \\ g^{(1)}_{1\mathrm{U}}(\tau) &= \frac{\langle E^*_1(x,y,z,t) \odot E_1(x,y-\mu,z,t+\tau)\rangle}{\sqrt{\langle |E^*_1(x,y,z,t)|^2\rangle \cdot \langle |E_1(x,y-\mu,z,t+\tau)|^2\rangle}} \text{ and} \\ g^{(1)}_{1\mathrm{D}}(\tau) &= \frac{\langle E^*_1(x,y,z,t) \odot E_1(x,y+\mu,z,t+\tau)\rangle}{\sqrt{\langle |E^*_1(x,y,z,t)|^2\rangle \cdot \langle |E_1(x,y+\mu,z,t+\tau)|^2\rangle}}. \end{aligned} \tag{7.8}$$

The new correlation ratios and its variation can then be calculated:

$$\begin{aligned}
\tilde{\eta}_{12/11}(\tau) &= \frac{\tilde{g}_{12}^{(1)}(\tau)}{|g_{11}^{(1)}(\tau)|}, \\
\tilde{\eta}_{13/11}(\tau) &= \frac{\tilde{g}_{13}^{(1)}(\tau)}{|g_{11}^{(1)}(\tau)|}, \\
\Delta\tilde{\eta}_{12/11}(\tau) &= \tilde{\eta}_{12/11}(\tau) - \tilde{\eta}_{12/11}(-\tau) \text{ and} \\
\Delta\tilde{\eta}_{13/11}(\tau) &= \tilde{\eta}_{13/11}(\tau) - \tilde{\eta}_{13/11}(-\tau).
\end{aligned} \tag{7.9}$$

Figure 7.4 compares the cross-correlation and correlation ratio with the reconstructed correlation ratio calculated with Eq. 7.7 and Eq. 7.9. The used data and method are the same as in Fig. 6.3. First row compares the cross-correlations ($|g_{12}^{(1)}|$ and $|g_{13}^{(1)}|$), the second row compares the correlation ratios ($|\eta_{12/11}|$ and $|\eta_{13/11}|$), the third row compares the ratio variations ($|\Delta\eta_{12/11}|$ and $|\Delta\eta_{13/11}|$), and the last row shows a plot at the center of the previous row.

In addition to not requiring an MSPL, this approach would allow determination of the entire flow direction. The sign of $\tilde{g}_{12}^{(1)}(\tau)$ and $\tilde{g}_{13}^{(1)}(\tau)$, as illustrated in Fig. 7.4, indicates the direction of the flow.

Another advantage is that the second-order correlation function can be used in its place. The system no longer needs to be phase-stable. The equations are essentially the same:

$$\begin{aligned}
g_{1\mathrm{L}}^{(2)}(\tau) &= \frac{\langle I_1^*(x,y,z,t) \odot I_1(x-\mu,y,z,t+\tau)\rangle}{\langle |I_1^*(x,y,z,t)|\rangle \cdot \langle |I_1(x-\mu,y,z,t+\tau)|\rangle}, \\
g_{1\mathrm{R}}^{(2)}(\tau) &= \frac{\langle I_1^*(x,y,z,t) \odot I_1(x+\mu,y,z,t+\tau)\rangle}{\langle |I_1^*(x,y,z,t)|\rangle \cdot \langle |I_1(x+\mu,y,z,t+\tau)|\rangle}, \\
g_{1\mathrm{U}}^{(2)}(\tau) &= \frac{\langle I_1^*(x,y,z,t) \odot I_1(x,y-\mu,z,t+\tau)\rangle}{\langle |I_1^*(x,y,z,t)|\rangle \cdot \langle |I_1(x,y-\mu,z,t+\tau)|\rangle} \text{ and} \\
g_{1\mathrm{D}}^{(2)}(\tau) &= \frac{\langle I_1^*(x,y,z,t) \odot I_1(x,y+\mu,z,t+\tau)\rangle}{\langle |I_1^*(x,y,z,t)|\rangle \cdot \langle |I_1(x,y+\mu,z,t+\tau)|\rangle}.
\end{aligned} \tag{7.10}$$

The Siegert relation ($g^{(2)} = |g^{(1)}|^2 + 1$) [169] is then applied before calculating the cross-correlation:

$$\begin{aligned}
\hat{g}_{12}^{(1)}(\tau) &= \frac{\sqrt{|g_{1\mathrm{L}}^{(2)}(\tau) - 1|} - \sqrt{|g_{1\mathrm{R}}^{(2)}(\tau) - 1|}}{2} \text{ and} \\
\hat{g}_{13}^{(1)}(\tau) &= \frac{\sqrt{|g_{1\mathrm{U}}^{(2)}(\tau) - 1|} - \sqrt{|g_{1\mathrm{D}}^{(2)}(\tau) - 1|}}{2}.
\end{aligned} \tag{7.11}$$

The hat is used to distinguish it from the version calculated from the first-order correlation

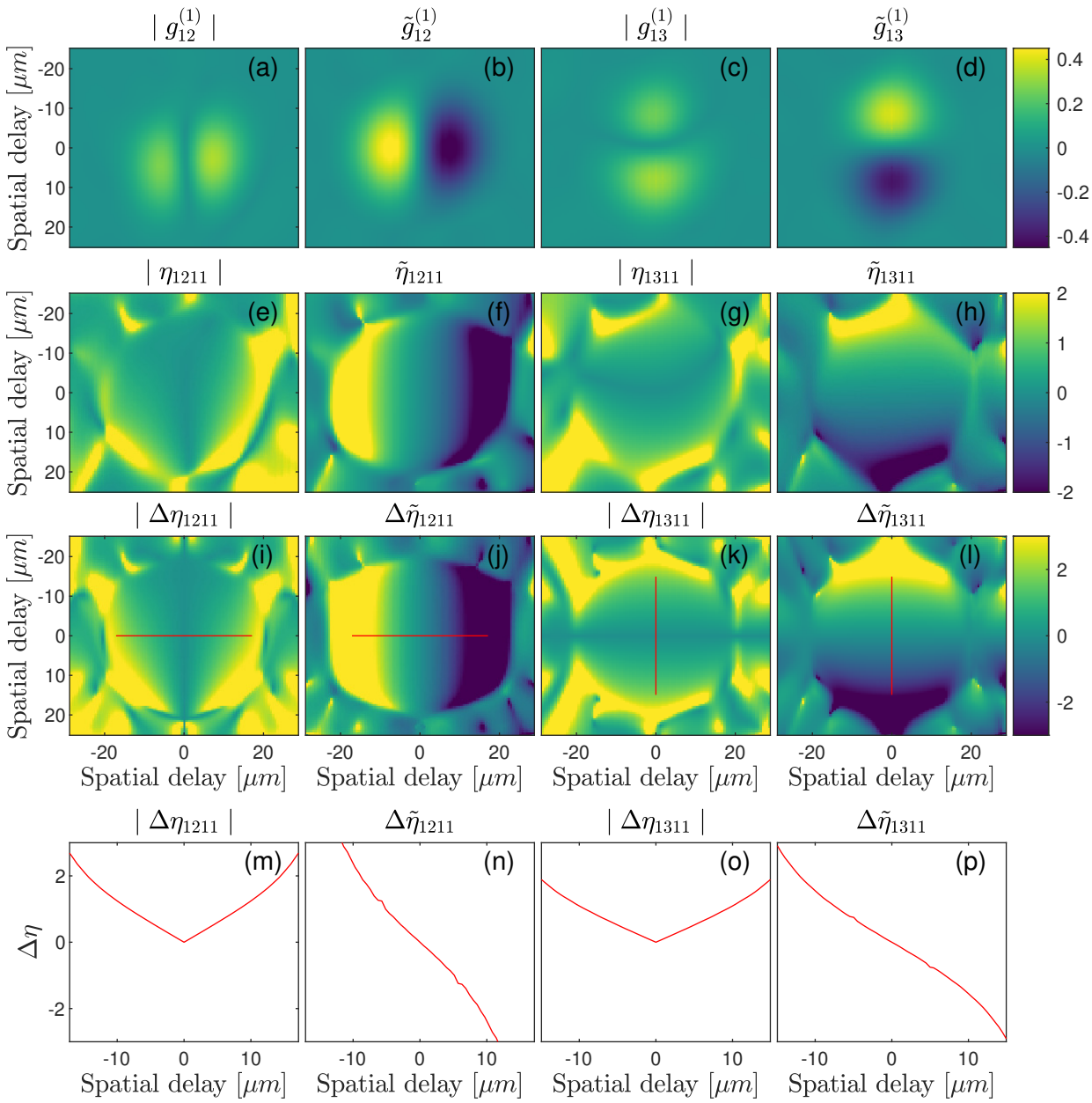

Figure 7.4 Comparison between correlation ratios calculated using the signal from a mode-selective photonic lantern and those reconstructed from Channel 1 alone. The first row presents the cross-correlation between channels, the second row displays the correlation ratio, the third row illustrates the variation of the correlation ratio, and the last row plots the central profile from the previous row.

and the one from the MSPL extra channels. The correlation ratio and the ratio variation are

calculated in the same way:

$$
\begin{aligned}
\hat{\eta}_{12/11}(\tau) &= \frac{\hat{g}_{12}^{(1)}(\tau)}{\sqrt{|g_{11}^{(2)}(\tau) - 1|}}, \\
\hat{\eta}_{13/11}(\tau) &= \frac{\hat{g}_{13}^{(1)}(\tau)}{\sqrt{|g_{11}^{(2)}(\tau) - 1|}}, \\
\Delta\hat{\eta}_{12/11}(\tau) &= \hat{\eta}_{12/11}(\tau) - \hat{\eta}_{12/11}(-\tau) \text{ and} \\
\Delta\hat{\eta}_{13/11}(\tau) &= \hat{\eta}_{13/11}(\tau) - \hat{\eta}_{13/11}(-\tau).
\end{aligned}
\tag{7.12}
$$

Figure 7.5, similarly to Fig. 7.4, shows the previous equation when applied to a static object that has been translated. It is the same method and dataset as in Fig. 6.3, but using Eqs. 7.11 and 7.12. The first and third columns compare the cross-correlation and correlation ratios of Channels 2 and 3, respectively, to their reconstructed counterparts using the second-order correlation function in the second and fourth columns, respectively. The first row shows the cross-correlation; the second row shows the correlation ratios; the third row shows the variation in correlation ratios; and the last row shows the center of the correlation ratio variation in the plot.

Both approaches appear to reproduce the results from Chapter 6, while additionally enabling determination of the complete flow direction. Notably, this method does not require an MSPL. However, it introduces the challenge of shifting the image by μ, which can be addressed by using either an oversampled full-field image or oversampling adjacent A-lines. Furthermore, the proposed methodology is not limited to OCT, but may also be applicable to any imaging technique affected by speckle noise.

Further flow measurements are needed to validate the efficacy of this approach in the presence of flow. Nevertheless, the results presented in Fig. 7.4 and Fig. 7.5 are highly promising.

A strictly linear relationship between the ratio and flow speed is not required. Instead of relying on a closed-form equation, a look-up table derived from figures such as Fig. 6.3, 7.4, or 7.5—which plot measured displacement as a function of the measured ratio—could be used. This approach would allow for the adoption of custom CSF profiles that differ from $hxy(x, y)|$ Ch2 and $hxy(x, y)|$ Ch3 and may otherwise be analytically intractable.

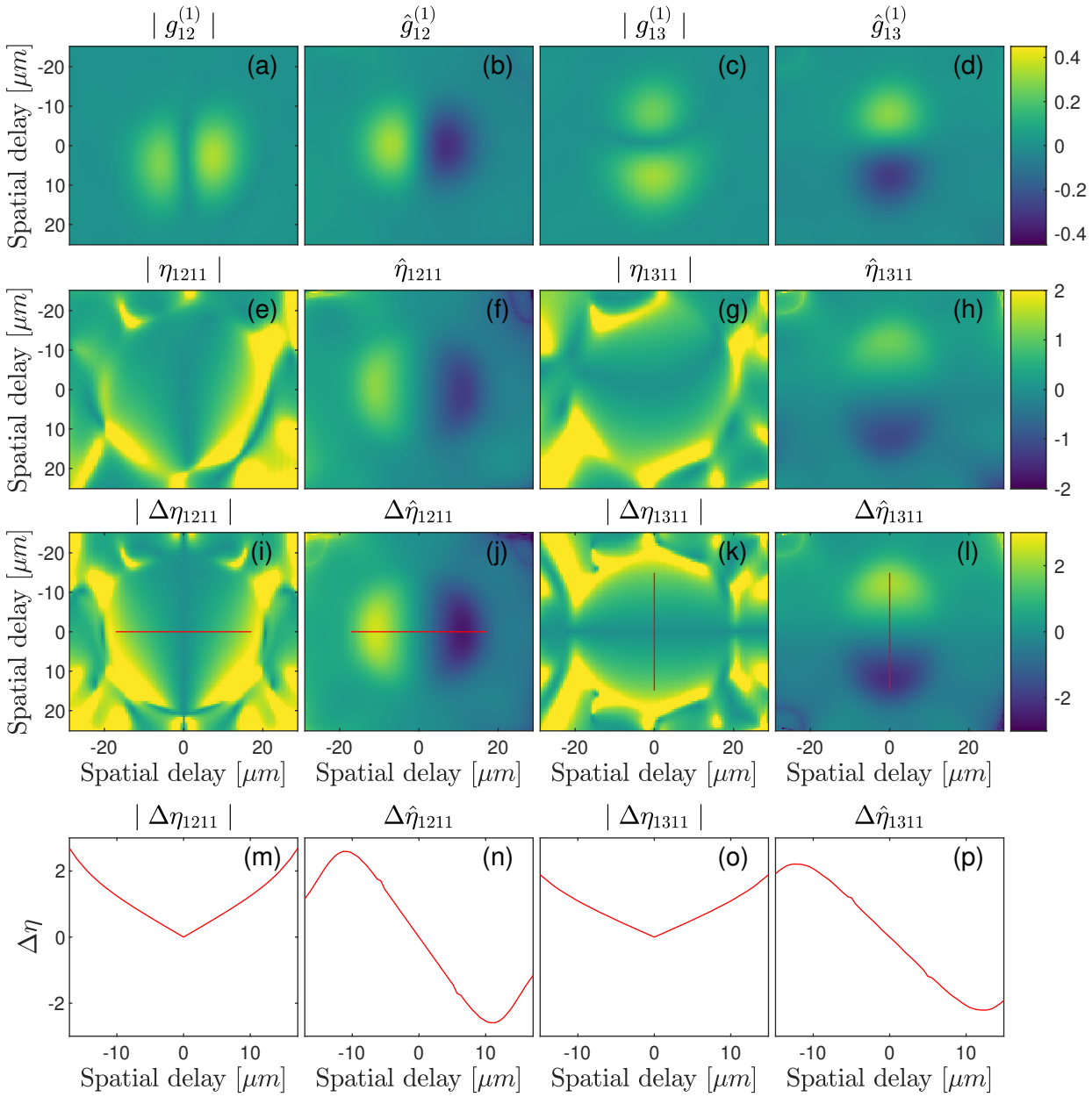

Figure 7.5 Comparison between correlation ratios calculated from mode-selective photonic lantern signals and those reconstructed from Channel 1 using the second-order correlation function. The first row presents the cross-correlation between channels, the second row displays the correlation ratio, the third row illustrates the variation of the correlation ratio, and the last row shows the central profile of the previous row.

7.2 Inconclusive avenues

This section presents ideas that were explored but ultimately found to be inconclusive, along with explanations for why certain avenues were not pursued further.

7.2.1 Super-resolution

Given that the superposition of the two LP11 modes forms a disk, there was interest in using the MSPL to achieve super-resolution. Subtracting this disk from a Gaussian beam could, in principle, create a beam with a diameter below the Rayleigh criterion. However, this subtraction of the LP11 modes is only feasible in the intensity domain.

OCT is inherently affected by speckle noise, which presents a significant challenge. When two LP11 modes are combined and then subtracted in the intensity domain, speckle noise prevents a true increase in resolution. The intention behind this subtraction is to remove the signal originating from the edges of the beam, but this edge signal is randomly interfered with by signal from the beam interior due to speckle. Since only the intensity is considered, phase information is lost, making it impossible to selectively remove the edge contribution to the speckle noise. Retaining phase information would be necessary for such selective removal.

Attempting this in the phase domain introduces a new problem: the two lobes of LP11 have opposite phases. Subtracting LP11 from LP01 thus results in constructive addition in one lobe and destructive subtraction in the other, necessitating a new CSF. Experiments were conducted using both illumination and detection with LP11 simultaneously, which should generate a CSF resembling LP11 with both lobes in phase. This approach was successfully tested on a resolution target, producing a modest increase in resolution; however, the target consisted of a glass surface and exhibited no speckle noise. When the same approach was applied to a sample with speckle, it did not yield improved resolution for reasons that remain unclear. Further investigation was discontinued in favor of more promising alternatives.

A colleague, Martin Poinsinet de Sivryl-Houle, proposed utilizing an even higher-order mode, LP02, to interfere with the Gaussian mode, LP01, thereby creating a physically narrower beam and potentially circumventing speckle noise issues. While this approach is theoretically promising, it requires an MSPL capable of supporting higher-order modes, which are not currently available, and thus remains speculative. Future investigation into this strategy is warranted as a possible route to super-resolution, although phase alignment and polarization matching between modes will present significant challenges.

7.2.2 Axial gradient velocity simulations

AGV presents a significant limitation for flow measurement using correlation methods. Although a model exists to describe its impact on conventional correlation schemes, it is not readily adaptable to the correlation ratio approach proposed in Chapter 6. Attempts were made to extend this model; however, the mathematics of the original work were neither straightforward nor explicit, and the correlation-ratio case proved to be considerably more complex.

Consequently, a simulation-based approach was attempted. Unfortunately, the simulation produced questionable results that partially contradicted the experimental findings described in Chapter 6. The source of this discrepancy was not identified, and the simulation results remain uninterpreted.

7.2.3 Scatterer size contrast

Previous research on FM-OCT has highlighted mode-coupling sensitivity to scatterer size as a potentially valuable source of contrast. This avenue was not pursued in the present thesis, primarily due to the difficulty of obtaining suitable samples for testing and the prioritization of other, more promising applications.

It is also challenging to attribute observed contrast reliably, as prior models considered only spherical scatterers. Thorough investigation of this avenue would require extensive trial-and-error experimentation to identify which pathologies could be diagnosed with this contrast mechanism. Additionally, since similar approaches have been explored by other groups, it was uncertain whether FM-OCT offered a distinct advantage. As a result, other applications were prioritized in this work.

7.3 Thesis-specific objectives

This section provides a critical reflection on the thesis-specific objectives, assesses the extent to which the research objectives were achieved, and considers areas for potential improvement and their impact.

7.3.1 Building the system

The design of the FM-OCT system was accomplished. Both hardware and software components were adapted from a previous OCT setup, which was subsequently upgraded to a fiber-based FM-OCT configuration. In the absence of a fiber connector, the tip of the MSPL remained unconnectorized; however, its short length mitigated the risk of breaking or moving. Nevertheless, the component was overall delicate and broke twice, necessitating replacement. Specular reflection at the MSPL tip also posed a significant challenge, limiting SNR and requiring the tip to be positioned farther from the imaging lens to reduce its impact on SNR.

While the fragility of the system limited its portability, the primary constraint was the laser source, which was shared among multiple projects and therefore could not be transported with the rest of the setup. This limitation prevented the system from being deployed in a hospital setting for testing on biological samples. However, this restriction afforded additional time to focus on theoretical work and the development of new innovations.

Overall, the system closely resembled the previous FM-OCT configuration, albeit operating at a different wavelength, with increased signal strength and a faster A-line acquisition rate. The broader impact of FM-OCT will likely remain constrained until a connectorized MSPL devices become commercially available.

A similar system was also constructed for a four-mode FM-OCT as part of a separate project.

7.3.2 Modeling multi-modal signals

Several points from the publication presented in Chapter 3 warrant further discussion. The comparison of optical fluence maps with MCX served to validate whether the developed code and associated schemes functioned as intended. MCX is a widely used and validated Monte Carlo simulator. Demonstrating that our simulator could reproduce similar results confirmed its ability to accurately simulate photon distribution within the sample, even when employing a biased scattering function. This finding supports the use of a biased scattering function in combination with photon splitting and a likelihood ratio as a valid modeling strategy.

The OCT signal simulation was validated by comparing simulated data with experimental

measurements. Specifically, the objective was to reproduce the experimental attenuation curves based on the sample's optical properties. For this comparison, amplitude normalization was performed. After OCT signal processing and prior to displaying the signal on a logarithmic scale, both simulated and experimental signals were divided by the average signal amplitude just below the surface (approximately 60 µm). This region was chosen because it is unaffected by strong Fresnel reflections at the air-sample interface and maintains a high SNR.

A deeper understanding of the OCT signal can facilitate the development of advanced OCT-based applications [84, 93–99, 101, 102, 104–107].

More specifically, in relation to this thesis, the objective was to investigate how altering the detected mode influences the relative signal amplitude between modes. Similar approaches have been employed as contrast mechanisms for disease tissue identification by other groups [14–16]. While normalization was necessary when comparing experimental data to simulations, it should not be required for comparing simulations that employ the same number of photons.

The publication presented in Chapter 3 did not fully achieve this objective, as other avenues were prioritized, as explained in Sec. 7.2.3.

Although the work did not ultimately simulate an FM-OCT signal, it resulted in a publication that, for the first time, experimentally validated Monte Carlo methods for OCT signal simulation. To extend this work further, one could consider switching the illumination and detection modes; for example, simulating both LP01 and LP11 illumination while maintaining a consistent detection scheme. In such a scenario, the initial random Gaussian distribution would be replaced by a random LP11 distribution.

Furthermore, the Henyey-Greenstein scattering function could be replaced with more modern and accurate models that better represent the scattering properties of biological tissue.

Instead, to simulate FM-OCT—and specifically FM-OCT speckle signals—simple simulators, such as the one described in Sec. 2.5, were utilized. Although this did not result in a publication, modeling scatterers as particles contributed to understanding few-mode signals. This approach aided in interpreting initial experimental results and informed the direction of subsequent investigations. Even though these simulations are not included in the papers published in Chapters 4 and 6, they were instrumental as an early testbed for developing new methods.

Unfortunately, the overall impact of this effort is limited. The original Monte Carlo code underlying the simulator should have been replaced earlier with a more modern, computationally

efficient alternative. Instead, emphasis was placed on validating the modeling approach and pursuing more productive research directions. Nonetheless, the published work contributes to validating the methodologies used by other groups and introduces a novel illumination scheme. Future research should focus on adopting faster simulation codes and integrating innovations from multiple sources.

7.3.3 Improving signal quality

Several points from the publication presented in Chapter 4 merit further discussion. While the MSPL guarantees transverse coregistration, axial coregistration must be performed separately. The axial mismatch arises primarily from differences in fiber length in the different channels. Although different modes exhibit distinct effective refractive indices during fiber propagation, higher-order modes are only present within the MSPL tip, which is approximately 3 cm long. Thus, the induced delay from modal dispersion is minimal compared to the delay introduced by differences in fiber length.

Two reference arms were incorporated to coarsely adjust the axial delay, but they were insufficient for subresolution axial coregistration. Fine coregistration was achieved by measuring the delay via correlation and applying subresolution translation to the image. B-scans from both channels were averaged into a single A-line to reduce speckle noise. Subresolution translation [167] was performed to maximize the cross-correlation between the two A-lines. Figure 4.2 demonstrates the system's response to a mirror after successful axial coregistration.

Due to differences in the collection mode, Channels 1 and 2 exhibit distinct responses. As previously mentioned, Channel 2 functions analogously to a Sobel filter for edge detection, as the LP11 mode closely resembles the Sobel filter in its mathematical form. This is equivalent to applying the filter directly to the OCT complex signal in the transverse plane.

Accordingly, evaluating the edge response is challenging for Channel 2 because it lacks a Gaussian profile. However, our main focus was on the edge response of the combined signals, as this configuration yields lower speckle contrast, and comparing it to the response of Channel 1. The response of the combined channels was sufficiently close to Gaussian for evaluation and closely matched that of Channel 1. An increase in transverse resolution of 11% was measured in one direction, while no change was observed in the other.

Speckle reduction is achieved because the speckle patterns in Channels 1 and 2 are uncorrelated. This results from the LP01 and LP11 mode functions being inherently uncorrelated, and thus their associated transverse CSF are also uncorrelated. A second-order correlation value of 1.04 was measured between the speckle patterns of both channels. The slight

deviation from 1—which would indicate complete decorrelation—may be attributed to imperfections in the MSPL, which cause the actual CSF to be slightly correlated. Nevertheless, strong decorrelation is demonstrated between the channels.

An improvement in SNR was observed, though its origin warrants clarification. As two channels are imaged simultaneously, the signal is effectively collected twice within the same integration time. Normalization does not affect the SNR, as it scales both the signal and noise components proportionally. Combining the signals averages out the noise, similar to the way speckle noise is reduced. This process is analogous to averaging two consecutive A-lines to enhance SNR, with the distinction that the two channels may not possess identical SNR as two A-lines acquired from the same channel.

Overall, the speckle reduction method was successful. Although some speckle remains, the technique reduces speckle noise at only a minor cost to resolution and with an improvement in SNR. It can also be combined with existing solutions to further reduce speckle noise. The primary limitation is the requirement for an FM-OCT system. The method's broader impact is currently constrained by the limited availability of MSPL devices on the market, though this is expected to change in the near future. Once such devices are readily accessible, image quality should improve, facilitating the visualization of small structures.

It is suspected that the approach used is analogous to wavelet-based methods for speckle noise reduction. The FM-OCT technique may serve as an empirical counterpart applied to digital wavelet filtering.

Super-resolution would have been an interesting direction to pursue; however, at the time, it was anticipated that an MSPL supporting LP02 would become available in the near future. As a result, further work with LP11 was deprioritized in favor of awaiting LP02. Once such an MSPL is accessible, this application should be revisited. Notably, lateral resolution in OCT is often limited by the imaging lens, which must be selected based on the desired Rayleigh length of the beam or, in ophthalmology, by the fact that the lens is the patient's eye. Super-resolution would permit going beyond this limit.

7.3.4 Flow measurement

Arguably, the most innovative contribution of this thesis is the correlation-ratio method described in Chapter 6. This technique was successfully demonstrated as a more accurate alternative to existing methods. Table 6.2 indicates that v_{fit} has a lower RMSE than v_{tot} in one specific case; however, inspection of Fig. 6.6 (d) reveals that v_{fit} failed to accurately measure transverse flow speed, whereas v_{tot} provided results that were closer to the expected

values. The higher RMSE observed for v_{tot} is most likely attributable to outliers rather than a lack of accuracy in the technique itself.

The technique was tested using both diluted milk and ex vivo pork blood. As no significant difference was observed when changing the sample—consistent with previous findings [73]—diluted milk was selected for the experiments reported in Chapter 6. However, the method has not yet been evaluated in vivo and therefore requires further investigation before clinical implementation. Unfortunately, the system was not portable and did not operate at the optimal wavelength for retinal imaging. Further research is also required to assess the approach without an MSPL.

As with much of the work in this thesis, the broader impact of the correlation-ratio method is currently constrained by the limited commercial availability of MSPL, a situation that is expected to improve in the near future. Once this limitation is overcome, the method could have a substantial impact, as it provides a much-needed tool for accurate lateral flow measurement. Its high accuracy enables precise detection of sub-pixel displacements, and the additional information it provides about flow orientation could facilitate studies of retinal disease progression. Furthermore, the versatility of the method allows for its application in devices beyond OCT.

CHAPTER 8 CONCLUSION

This section provides a summary of the contributions made in this thesis, highlighting their impact and limitations and offering an outlook on future research directions.

8.1 Summary of work and limitations

Technological innovations often serve as catalysts for further progress. This project began as an investigation into the opportunities offered by a new optical component—the MSPL—for the field of OCT, but ultimately expanded beyond this initial focus.

A fiber-based FM-OCT system and its accompanying software were developed, featuring both two- and three-channel configurations. The three-channel configuration could image Channels 2 and 3 simultaneously or independently. This system represented a significant improvement over its predecessor, constructed by a colleague [17]. The imaging head was made more robust by using a shorter, better-supported MSPL, and the system enabled faster acquisitions with a more user-friendly software interface.

However, several limitations remain. The laser used in the system operates at a suboptimal wavelength for retinal imaging due to absorption in the eye. While the system can image small eyes, such as those of mouse pups, this comes at a high cost to signal quality. Additionally, although the system is faster than its predecessor, it remains somewhat slower than contemporary clinical devices, limiting its clinical applicability. Finally, the system could not be transported to the hospital, primarily because the laser was required for other projects in the laboratory.

The constructed system demonstrated that FM-OCT can operate robustly despite the inherent fragility of MSPL components.

Several methods for modeling light propagation in OCT signals were proposed. A Monte Carlo approach was refined and experimentally validated to accurately replicate OCT A-lines, representing the first experimental validation for reproducing OCT A-line attenuation curves.

However, the simulator is limited by its underlying codebase. The modified code was CPU-based rather than GPU-based, making it significantly slower than GPU-accelerated alternatives and limiting its broader usability. Ideally, the original code should have been replaced earlier with a GPU version, and validation should have been performed on the upgraded software. Due to time constraints, the code was not sufficiently advanced to simulate FM-OCT

signals and thus cannot be used to compare the sensitivity of FM-OCT channels to different samples.

Nonetheless, the code validated the use of Monte Carlo approaches for simulating OCT signals, thereby supporting the work of other groups using similar simulators and paving the way for future research in this area.

To simulate FM-OCT speckle patterns, simpler speckle simulators were developed to support the validation and development of various theoretical models presented in the thesis. These simulators did not result in publications, as the concept was not novel. Instead, their main contribution was enabling the development and publication of new models for speckle reduction and flow measurement.

A novel speckle-reduction method was demonstrated, which also improves SNR. This method relies on detecting signals from higher-order modes collected by the MSPL to generate simultaneous images with distinct speckle noise patterns. The speckle noise can then be reduced by averaging these images. Unlike other approaches, this method incurs only a 0 to 10% cost in resolution for a speckle contrast reduction factor of $1/\sqrt{2}$. Furthermore, it does not rely on distinguishing between variations due to speckle and those due to anatomy, as some other approaches do.

This approach enables improved image quality, particularly for small structures near the resolution limit of OCT, which are often difficult to distinguish from the speckle pattern. Conventional speckle-reduction methods rely on averaging neighboring pixels, which suppresses both speckle noise and small structural details. In contrast, angled detection may be the only way to reveal structures that would otherwise be obscured by speckle. Moreover, this method is complementary to alternative approaches and can be combined with them to further enhance speckle reduction.

The method is conceptually similar to wavelet-based techniques used in the literature for speckle noise reduction; however, unlike wavelets, it constitutes an empirical rather than a numerical solution.

The method was demonstrated only with a two-channel FM-OCT. Increasing the number of channels could yield further speckle reduction and greater SNR improvement, as predicted in Chapter 4. However, adding more channels introduces scalability challenges, as additional OCT systems would be required to detect each channel.

Once MSPLs become commercially available, this speckle-reduction method could be readily implemented in clinical applications to enhance image quality.

Finally, a novel method for flow measurement was developed and demonstrated. This method

relies on a ratio of correlation measurements to achieve greater accuracy than existing alternatives. It measures flow (or displacement) perpendicular to the imaging axis—an orientation that has traditionally been challenging to assess. The technique provides previously unavailable information on flow orientation, although it yields only the absolute values of v_x and v_y, not their signs. While the method was demonstrated using an MSPL, alternative approaches employing standard OCT systems were also proposed, yielding promising preliminary results and enabling determination of full flow direction.

Ultimately, the most significant advantage of this method over alternative approaches is that it relies on signal re-correlation rather than decorrelation to measure flow. While signal decorrelation can result from multiple sources—such as flow, diffusion, and shadow artifacts—signal re-correlation is specifically attributed to scatterers moving from one location to another, thereby minimizing sources of bias.

This method addresses a critical need in OCTA by enabling flow measurement in the transverse direction. A direction most retinal blood vessels are. It can also differentiate between blood diffusion and flow, as well as facilitate measurement of much slower flow rates. Reliable quantitative measurements remain a challenge for OCTA, limiting the scope of studies on retina-related diseases. The correlation-based approach may also be applicable to other organs where accurate blood flow measurement is required.

The scope of this contribution is limited by the fact that it has not yet been demonstrated *in vivo*. Further work is required to implement the method *in vivo* and to evaluate its feasibility in this challenging context.

The alternative implementation without MSPL also requires validation on dynamic samples, as it has only been demonstrated on static data. Furthermore, it has not yet been compared to alternative methods, so its relative performance remains unknown.

In summary, the correlation ratio approach has the potential to change the paradigm of flow measurement in the retina by providing a more accurate alternative. Its initial impact is likely to be in research, supporting the study of diseases and determining whether improved measurement accuracy can offer diagnostic benefits.

8.2 Outlook

While the current impact of the work presented here is primarily limited by the market accessibility of MSPL, this situation is evolving. MSPLs are inherently fragile due to their small tip diameter (approximately 10 µm), making them susceptible to movement when suspended in air. This fragility also complicates the creation of a standard fiber connector at

the tip, resulting in an uncontrolled cleave angle. Significant backreflection from this cleave can introduce considerable noise into the OCT signal, as was observed with the MSPLs used in this project. However, another group [56] has addressed this by splicing a short multimode fiber to the tip, and such solutions are now being adopted in the industry. The commercialization of connectorized MSPL devices is imminent, which will address issues of availability, reduce backreflection, and improve integration with optical systems.

As a result, FM-OCT systems will become much easier to construct. However, as MSPLs with increasing channel counts are developed, it will become costly to use a parallel OCT setup for each channel. Employing a swept-source laser OCT is a more economical solution, as extra balanced detectors are generally less expensive than additional spectrometers. Another cost-effective alternative is to combine the signals from multiple channels into a single detector, as demonstrated in Chapter 6. Since the axial imaging range of OCT typically far exceeds the imaging depth, it is feasible to add multiple OCT images within one axial imaging range. However, this approach does not improve SNR, as the signal lost through the coupler used to combine channels offsets the gain from adding an additional channel.

Future work on Monte Carlo simulation for OCT should focus on integrating the various methods developed by different research groups into a unified, GPU-based codebase. The code could also be upgraded to simulate FM-OCT signals, as proposed by adapting the illumination scheme. This enhancement would enable the comparison of different types of modal collection and NA, helping to determine which combinations offer the most promising contrast for specific clinical applications.

Regarding the simulation of speckle dynamics, the method presented in Sec. 2.5 remains appropriate, though further development is possible. For example, it could be utilized to calculate the convergence rate of correlation calculations, thereby providing better estimates of the integration time required to achieve a desired precision in flow measurements.

The most immediate impact is likely to arise from the speckle-reduction method, which is straightforward to implement once MSPLs become available. Future work should focus on applying this approach to FM-OCT systems with a greater number of channels and on evaluating its performance in clinical applications. However, as the number of channels increases, higher-order LP modes will broaden, which may gradually affect resolution.

Alternatively, PL could be used instead of MSPL. PL devices typically support a greater number of channels than MSPL. Although the LP modes are mixed in PL, this may not pose a problem if the main objective is speckle noise reduction through signal combination, making this avenue worth investigating.

Alternatively, a similar strategy employing wavelets could be explored. Using wavelets for speckle noise reduction appears to be a numerical analogue to the empirical approach presented here. The fiber LP modes could inspire the construction of a wavelet basis, enabling numerical reproduction of the empirical results. This concept is reminiscent of the previously proposed correlation ratio method for flow measurement without a PL. While such an approach would avoid the need for a PL, wavelets with higher spatial frequencies could introduce SNR challenges, similar to those encountered in deconvolution-based super-resolution methods.

The most impactful contribution of this thesis is the new flow measurement method. The logical next step is to test the method *in vivo*. The primary objective should be to determine whether the method can be successfully applied to retinal imaging in a clinical context. However, several challenges remain for implementation. The first is compensating for sample motion in *in vivo* applications. The most significant challenge, however, is to identify an appropriate scanning strategy.

Correlation methods require temporal comparison of images. If the time delay between correlated pixels is too long, the signal becomes fully decorrelated and flow speed cannot be measured. This necessitates a sufficiently rapid scanning scheme. The most straightforward approach is to perform B-scans as quickly as possible. While feasible, capturing the fastest anatomical flow speeds demands the fastest available systems. An alternative, only briefly explored, involves acquiring two consecutive A-lines at each position in a B-scan. This approach is difficult to implement with conventional galvanometer-mirror scanning systems, as maintaining the mirror in a fixed position before moving at OCT scanning speed is challenging.

The M-mode approach may be well-suited for other applications. For example, a recurrent challenge in surgery is determining when a surgeon is about to cut or pierce a region with significant blood flow. A fiber equipped with a MSPL could readily assess blood flow at a specific location. Surgical applications requiring point-specific blood flow measurements warrant further exploration.

Subsequent validation of the measurement *in vivo* will be challenging, as there is no direct reference standard available for verification; the presented method aims to provide a more accurate alternative to existing techniques. The method should also be evaluated in capillary-sized tubing *ex vivo* with a known flow velocity.

REFERENCES

[1] W. Drexler and J. G. Fujimoto, *Optical coherence tomography: technology and applications*. Springer Science & Business Media, 2008.

[2] M. A. Windsor, S. J. J. Sun, K. D. Frick, E. A. Swanson, P. J. Rosenfeld, and D. Huang, "Estimating Public and Patient Savings From Basic Research—A Study of Optical Coherence Tomography in Managing Antiangiogenic Therapy," *American Journal of Ophthalmology*, vol. 185, pp. 115–122, 2018.

[3] H. Yabushita, B. E. Bouma, S. L. Houser, H. T. Aretz, I.-K. Jang, K. H. Schlendorf, C. R. Kauffman, M. Shishkov, D.-H. Kang, E. F. Halpern, and G. J. Tearney, "Characterization of Human Atherosclerosis by Optical Coherence Tomography," *Circulation*, vol. 106, no. 13, pp. 1640–1645, 2002.

[4] N. Uribe-Patarroyo and B. E. Bouma, "Rotational distortion correction in endoscopic optical coherence tomography based on speckle decorrelation," *Optics Letters*, vol. 40, no. 23, p. 5518, 2015.

[5] M. Gan, C. Wang, T. Yang, N. Yang, M. Zhang, W. Yuan, X. Li, and L. Wang, "Robust layer segmentation of esophageal OCT images based on graph search using edge-enhanced weights," *Biomedical Optics Express*, vol. 9, no. 9, pp. 4481–4495, 2018.

[6] J. M. Schmitt, S. H. Xiang, and K. M. Yung, "Speckle in optical coherence tomography," *Journal of Biomedical Optics*, vol. 4, no. 1, pp. 95 – 105, 1999.

[7] I. Rubinoff, L. Beckmann, Y. Wang, A. A. Fawzi, X. Liu, J. Tauber, K. Jones, H. Ishikawa, J. S. Schuman, R. Kuranov, and H. F. Zhang, "Speckle reduction in visible-light optical coherence tomography using scan modulation," *Neurophotonics*, vol. 6, no. 4, p. 041107, 2019.

[8] T. E. de Carlo, A. Romano, N. K. Waheed, and J. S. Duker, "A review of optical coherence tomography angiography (OCTA)," *International Journal of Retina and Vitreous*, vol. 1, p. 5, 2015.

[9] P. H. Le, K. Kaur, and B. C. Patel, "Optical Coherence Tomography Angiography," in *StatPearls*. Treasure Island (FL): StatPearls Publishing, 2026.

[10] N. Uribe-Patarroyo and B. E. Bouma, "Velocity gradients in spatially-resolved laser Doppler flowmetry and dynamic light scattering with confocal and coherence gating," *Physical review. E*, vol. 94, p. 022604, 2016.

[11] Z. Xu, Y. Wang, X. Chen, K. Lin, and L. Liu, "Dual beam optical coherence tomography angiography for decoupling axial velocity gradient," *Scientific Reports*, vol. 14, 2024.

[12] S. Brais-Brunet, É. Heckel, U. Kanniyappan, S. Chemtob, C. Boudoux, J.-S. Joyal, and M. Dehaes, "Morphometric and microstructural changes during murine retinal development characterized using in vivo optical coherence tomography," *Investigative Ophthalmology & Visual Science*, vol. 62, no. 13, pp. 20–20, 2021.

[13] M. Pircher, C. K. Hitzenberger, and U. Schmidt-Erfurth, "Polarization sensitive optical coherence tomography in the human eye," *Progress in Retinal and Eye Research*, vol. 30, no. 6, pp. 431–451, 2011.

[14] T. A. Birks, I. Gris-Sánchez, S. Yerolatsitis, S. G. Leon-Saval, and R. R. Thomson, "The photonic lantern," *Advances in Optics and Photonics*, vol. 7, pp. 107–167, 2015.

[15] P. Eugui, A. Lichtenegger, M. Augustin, D. J. Harper, M. Muck, T. Roetzer, A. Wartak, T. Konegger, G. Widhalm, C. K. Hitzenberger, A. Woehrer, and B. Baumann, "Beyond backscattering: optical neuroimaging by BRAD," *Biomed. Opt. Express*, vol. 9, no. 6, pp. 2476–2494, 2018.

[16] S. G. Leon-Saval, N. K. Fontaine, J. R. Salazar-Gil, B. Ercan, R. Ryf, and J. Bland-Hawthorn, "Mode-selective photonic lanterns for space-division multiplexing," *Opt. Express*, vol. 22, no. 1, pp. 1036–1044, 2014.

[17] M. P. d. Sivry-Houle, S. Bolduc-Beaudoin, S. Brais-Brunet, M. Dehaes, N. Godbout, and C. Boudoux, "All-fiber few-mode optical coherence tomography using a modally-specific photonic lantern," *Biomed. Opt. Express*, vol. 12, pp. 5704–5719, 2021.

[18] D. Huang, E. A. Swanson, C. P. Lin, J. S. Schuman, W. G. Stinson, W. Chang, M. R. Hee, T. Flotte, K. Gregory, and C. A. Puliafito, "Optical coherence tomography," *science*, vol. 254, no. 5035, pp. 1178–1181, 1991.

[19] C. Boudoux, *Fundamentals of Biomedical Optics*. Blurb, Incorporated, 2016.

[20] J. W. Goodman, *Speckle phenomena in optics: theory and applications*. Roberts and Company Publishers, 2007.

[21] M. Szkulmowski and M. Wojtkowski, "Averaging techniques for OCT imaging," *Opt. Express*, vol. 21, no. 8, pp. 9757–9773, 2013.

[22] M. H. Eybposh, Z. Turani, D. Mehregan, and M. Nasiriavanaki, "Cluster-based filtering framework for speckle reduction in OCT images," *Biomed. Opt. Express*, vol. 9, no. 12, pp. 6359–6373, 2018.

[23] M. Gargesha, M. W. Jenkins, A. M. Rollins, and D. L. Wilson, "Denoising and 4D visualization of OCT images," *Opt. Express*, vol. 16, no. 16, pp. 12 313–12 333, 2008.

[24] M. Szkulmowski, I. Gorczynska, D. Szlag, M. Sylwestrzak, A. Kowalczyk, and M. Wojtkowski, "Efficient reduction of speckle noise in Optical Coherence Tomography," *Opt. Express*, vol. 20, no. 2, pp. 1337–1359, 2012.

[25] C. Magnain, H. Wang, S. Sakadžić, B. Fischl, and D. A. Boas, "En face speckle reduction in optical coherence microscopy by frequency compounding," *Opt. Lett.*, vol. 41, no. 9, pp. 1925–1928, 2016.

[26] L. Fang, S. Li, R. P. McNabb, Q. Nie, A. N. Kuo, C. A. Toth, J. A. Izatt, and S. Farsiu, "Fast Acquisition and Reconstruction of Optical Coherence Tomography Images via Sparse Representation," *IEEE Transactions on Medical Imaging*, vol. 32, no. 11, pp. 2034–2049, 2013.

[27] G. van Soest, M. Villiger, E. Regar, G. J. Tearney, B. E. Bouma, and A. F. W. van der Steen, "Frequency domain multiplexing for speckle reduction in optical coherence tomography," *J. Biomed. Opt.*, vol. 17, no. 7, p. 076018, 2012.

[28] L. Fang, S. Li, D. Cunefare, and S. Farsiu, "Segmentation Based Sparse Reconstruction of Optical Coherence Tomography Images," *IEEE Transactions on Medical Imaging*, vol. 36, no. 2, pp. 407–421, 2017.

[29] Z. Jian, Z. Yu, L. Yu, B. Rao, Z. Chen, and B. J. Tromberg, "Speckle attenuation in optical coherence tomography by curvelet shrinkage," *Opt. Lett.*, vol. 34, no. 10, pp. 1516–1518, 2009.

[30] J. Cheng, D. Tao, Y. Quan, D. W. K. Wong, G. C. M. Cheung, M. Akiba, and J. Liu, "Speckle Reduction in 3D Optical Coherence Tomography of Retina by A-Scan Reconstruction," *IEEE Transactions on Medical Imaging*, vol. 35, no. 10, pp. 2270–2279, 2016.

[31] M. Pircher, E. Götzinger, R. A. Leitgeb, A. F. Fercher, and C. K. Hitzenberger, "Speckle reduction in optical coherence tomography by frequency compounding," *J. Biomed. Opt.*, vol. 8, no. 3, pp. 565 – 569, 2003.

[32] B. F. Kennedy, T. R. Hillman, A. Curatolo, and D. D. Sampson, "Speckle reduction in optical coherence tomography by strain compounding," *Opt. Lett.*, vol. 35, no. 14, pp. 2445–2447, 2010.

[33] Z. Jian, L. Yu, B. Rao, B. J. Tromberg, and Z. Chen, "Three-dimensional speckle suppression in optical coherence tomography based on the curvelet transform," *Opt. Express*, vol. 18, no. 2, pp. 1024–1032, 2010.

[34] D. Alonso-Caneiro, S. A. Read, and M. J. Collins, "Speckle reduction in optical coherence tomography imaging by affine-motion image registration," *J. Biomed. Opt.*, vol. 16, no. 11, p. 116027, 2011.

[35] A. E. Desjardins, B. J. Vakoc, W. Y. Oh, S. M. R. Motaghiannezam, G. J. Tearney, and B. E. Bouma, "Angle-resolved Optical Coherence Tomography with sequential angular selectivity for speckle reduction," *Opt. Express*, vol. 15, no. 10, pp. 6200–6209, 2007.

[36] P. Li, L. Zhou, Y. Ni, Z. Ding, and P. Li, "Angular compounding by full-channel B-scan modulation encoding for optical coherence tomography speckle reduction," *J. Biomed. Opt.*, vol. 21, no. 8, p. 086014, 2016.

[37] C. Chen, W. Shi, R. Deorajh, N. Nguyen, J. Ramjist, A. Marques, and V. X. Yang, "Beam-shifting technique for speckle reduction and flow rate measurement in optical coherence tomography," *Opt. Lett.*, vol. 43, no. 24, pp. 5921–5924, 2018.

[38] D. Cui, E. Bo, Y. Luo, X. Liu, X. Wang, S. Chen, X. Yu, S. Chen, P. Shum, and L. Liu, "Multifiber angular compounding optical coherence tomography for speckle reduction," *Opt. Lett.*, vol. 42, no. 1, pp. 125–128, 2017.

[39] N. Iftimia, B. E. Bouma, and G. J. T. M.D, "Speckle reduction in optical coherence tomography by "path length encoded" angular compounding," *J. Biomed. Opt.*, vol. 8, no. 2, pp. 260 – 263, 2003.

[40] L. Wang, Z. Meng, X. S. Yao, T. Liu, Y. Su, and M. Qin, "Adaptive Speckle Reduction in OCT Volume Data Based on Block-Matching and 3-D Filtering," *IEEE Photonics Technology Letters*, vol. 24, no. 20, pp. 1802–1804, 2012.

[41] J. Aum, J.-h. Kim, and J. Jeong, "Effective speckle noise suppression in optical coherence tomography images using nonlocal means denoising filter with double Gaussian anisotropic kernels," *Appl. Opt.*, vol. 54, pp. D43–D50, 2015.

[42] A. Wong, A. Mishra, K. Bizheva, and D. A. Clausi, "General Bayesian estimation for speckle noise reduction in optical coherence tomography retinal imagery," *Opt. Express*, vol. 18, no. 8, pp. 8338–8352, 2010.

[43] H. Yu, J. Gao, and A. Li, "Probability-based non-local means filter for speckle noise suppression in optical coherence tomography images," *Opt. Lett.*, vol. 41, no. 5, pp. 994–997, 2016.

[44] L. Fang, S. Li, Q. Nie, J. A. Izatt, C. A. Toth, and S. Farsiu, "Sparsity based denoising of spectral domain optical coherence tomography images," *Biomed. Opt. Express*, vol. 3, no. 5, pp. 927–942, 2012.

[45] H. Lv, S. Fu, C. Zhang, and L. Zhai, "Speckle noise reduction for optical coherence tomography based on adaptive 2D dictionary," *Laser Physics Letters*, vol. 15, no. 5, p. 055401, 2018.

[46] H. Ren, L. Qin, and X. Zhu, "Speckle reduction and cartoon-texture decomposition of ophthalmic optical coherence tomography images by variational image decomposition," *Optik*, vol. 127, no. 19, pp. 7809–7821, 2016.

[47] T. Wu, Y. Shi, Y. Liu, and C. He, "Speckle reduction in optical coherence tomography by adaptive total variation method," *Journal of Modern Optics*, vol. 62, no. 21, pp. 1849–1855, 2015.

[48] A. Ozcan, A. Bilenca, A. E. Desjardins, B. E. Bouma, and G. J. Tearney, "Speckle reduction in optical coherence tomography images using digital filtering," *J. Opt. Soc. Am. A*, vol. 24, no. 7, pp. 1901–1910, 2007.

[49] D. Yin, Y. Gu, and P. Xue, "Speckle-constrained variational methods for image restoration in optical coherence tomography," *J. Opt. Soc. Am. A*, vol. 30, no. 5, pp. 878–885, 2013.

[50] Y. Gu and X. Zhang, "Spiking cortical model based non-local means method for despeckling multiframe optical coherence tomography data," *Laser Physics Letters*, vol. 14, no. 5, p. 056201, 2017.

[51] Y. Huang, Z. Lu, Z. Shao, M. Ran, J. Zhou, L. Fang, and Y. Zhang, "Simultaneous denoising and super-resolution of optical coherence tomography images based on generative adversarial network," *Opt. Express*, vol. 27, no. 9, pp. 12 289–12 307, 2019.

[52] W. Lee, H. S. Nam, J. Y. Seok, W.-Y. Oh, J. W. Kim, and H. Yoo, "Deep learning-based image enhancement in optical coherence tomography by exploiting interference fringe," *Communications Biology*, vol. 6, no. 1, p. 464, 2023.

[53] C. Boudoux, *Fundamentals of biomedical optics*, 2017.

[54] X. Attendu, R. M. Ruis, C. Boudoux, T. G. v. Leeuwen, and D. J. Faber, "Simple and robust calibration procedure for k-linearization and dispersion compensation in optical coherence tomography," *J. Biomed. Opt.*, vol. 24, no. 5, p. 056001, 2019.

[55] M. Wojtkowski, V. J. Srinivasan, T. H. Ko, J. G. Fujimoto, A. Kowalczyk, and J. S. Duker, "Ultrahigh-resolution, high-speed, Fourier domain optical coherence tomography and methods for dispersion compensation," *Optics Express*, vol. 12, no. 11, pp. 2404–2422, 2004.

[56] A. M. Velázquez-Benítez, K. Y. Guerra-Santillán, R. Caudillo-Viurquez, J. E. Antonio-López, R. Amezcua-Correa, and J. Hernández-Cordero, "Optical trapping and micromanipulation with a photonic lantern-mode multiplexer," *Opt. Lett.*, vol. 43, pp. 1303–1306, 2018.

[57] R. I. Becerra-Deana, R. Maltais-Tariant, G. Ramadier, M. P. de Sivry-Houle, S. Virally, C. Boudoux, and N. Godbout, "Three-mode photonic lanterns: comprehensive analysis from theory to experiments," *Opt. Continuum*, vol. 4, no. 6, pp. 1198–1211, 2025.

[58] R. I. Becerra-Deana, M. P. de Sivry-Houle, S. Virally, C. Boudoux, and N. Godbout, "Mode-selective photonic lanterns with double-clad fibers," *Journal of Lightwave Technology*, vol. 43, no. 12, pp. 5829–5835, 2025.

[59] A. Tanskanen, J. Malone, E. Brace, C. MacAulay, and P. Lane, "Endoscopic few-mode fiber optical coherence tomography," in *Endoscopic Microscopy XX*, vol. PC13334. SPIE, 2025, p. PC133340G.

[60] V. Y. Zaitsev, L. A. Matveev, A. L. Matveyev, G. V. Gelikonov, and V. M. Gelikonov, "A model for simulating speckle-pattern evolution based on close to reality procedures used in spectral-domain oct," *Laser Physics Letters*, vol. 11, no. 10, p. 105601, 2014.

[61] R. Maltais-Tariant, C. Boudoux, and N. Uribe-Patarroyo, "Real-time co-localized OCT surveillance of laser therapy using motion corrected speckle decorrelation," *Biomed. Opt. Express*, vol. 11, no. 6, pp. 2925–2950, 2020.

[62] N. Uribe-Patarroyo, M. Villiger, and B. E. Bouma, "Quantitative technique for robust and noise-tolerant speed measurements based on speckle decorrelation in optical coherence tomography," *Opt. Express*, vol. 22, pp. 24 411–24 429, 2014.

[63] J. Lee, W. Wu, J. Y. Jiang, B. Zhu, and D. A. Boas, "Dynamic light scattering optical coherence tomography," *Optics Express*, vol. 20, pp. 22 262–22 277, 2012.

[64] N. Weiss, T. G. van Leeuwen, and J. Kalkman, "Localized measurement of longitudinal and transverse flow velocities in colloidal suspensions using optical coherence tomography," *Physical Review E*, vol. 88, p. 042312, 2013.

[65] J. Mertz, *Introduction to optical microscopy.* Cambridge University Press, 2019.

[66] I. Gorczynska, J. V. Migacz, R. J. Zawadzki, A. G. Capps, and J. S. Werner, "Comparison of amplitude-decorrelation, speckle-variance and phase-variance OCT angiography methods for imaging the human retina and choroid," *Biomedical Optics Express*, vol. 7, pp. 911–942, 2016.

[67] A. Mariampillai, B. A. Standish, E. H. Moriyama, M. Khurana, N. R. Munce, M. K. Leung, J. Jiang, A. Cable, B. C. Wilson, I. A. Vitkin, and V. X. D. Yang, "Speckle variance detection of microvasculature using swept-source optical coherence tomography," *Optics Letters*, vol. 33, pp. 1530–1532, 2008.

[68] R. A. Leitgeb, R. M. Werkmeister, C. Blatter, and L. Schmetterer, "Doppler Optical Coherence Tomography," *Progress in Retinal and Eye Research*, vol. 41, pp. 26–43, 2014.

[69] O. Tan, R. Konduru, X. Zhang, S. R. Sadda, and D. Huang, "Dual-Angle Protocol for Doppler Optical Coherence Tomography to Improve Retinal Blood Flow Measurement," *Translational Vision Science & Technology*, vol. 3, p. 6, 2014.

[70] S. Brais-Brunet, E. Heckel, U. Kanniyappan, S. Chemtob, C. Boudoux, J.-S. Joyal, and M. Dehaes, "Morphometric and Microstructural Changes During Murine Retinal Development Characterized Using In Vivo Optical Coherence Tomography," *Invest. Ophthalmol. Vis. Sci.*, vol. 62, p. 20, 2021.

[71] B. Braaf, S. Donner, N. Uribe-Patarroyo, B. E. Bouma, and B. J. Vakoc, "A Neural Network Approach to Quantify Blood Flow from Retinal OCT Intensity Time-Series Measurements," *Scientific Reports*, vol. 10, p. 9611, 2020.

[72] Y. Hwang, J. Won, A. Yaghy, H. Takahashi, J. M. Girgis, K. Lam, S. Chen, E. M. Moult, S. B. Ploner, A. Maier, N. K. Waheed, and J. G. Fujimoto, "Retinal blood flow speed quantification at the capillary level using temporal autocorrelation fitting OCTA [Invited]," *Biomedical Optics Express*, vol. 14, pp. 2658–2677, 2023.

[73] N. G. Ferris, T. M. Cannon, M. Villiger, B. E. Bouma, and N. Uribe-Patarroyo, "Forward multiple scattering dominates speckle decorrelation in whole-blood flowmetry using optical coherence tomography," *Biomedical Optics Express*, vol. 11, no. 4, 2020.

[74] C. Z. Jafari, S. A. Mihelic, S. Engelmann, and A. K. Dunn, "High-resolution three-dimensional blood flow tomography in the subdiffuse regime using laser speckle contrast imaging," *Journal of Biomedical Optics*, vol. 27, p. 083011, 2022.

[75] D. Huang, E. A. Swanson, C. P. Lin, J. S. Schuman, W. G. Stinson, W. Chang, M. R. Hee, T. Flotte, K. Gregory, C. A. Puliafito, and J. G. Fujimoto, "Optical coherence tomography," *Science*, vol. 254, no. 5035, pp. 1178–1181, 1991.

[76] M. Wojtkowski, R. Leitgeb, A. Kowalczyk, T. Bajraszewski, and A. F. Fercher, "In vivo human retinal imaging by Fourier domain optical coherence tomography," *Journal of Biomedical Optics*, vol. 7, no. 3, pp. 457–463, 2002.

[77] I.-K. Jang, B. E. Bouma, D.-H. Kang, S.-J. Park, S.-W. Park, K.-B. Seung, K.-B. Choi, M. Shishkov, K. Schlendorf, E. Pomerantsev, S. L. Houser, H. Aretz, and G. J. Tearney, "Visualization of coronary atherosclerotic plaques in patients using optical coherence tomography: comparison with intravascular ultrasound," *Journal of the American College of Cardiology*, vol. 39, no. 4, pp. 604–609, 2002.

[78] T. Gambichler, G. Moussa, M. Sand, D. Sand, P. Altmeyer, and K. Hoffmann, "Applications of optical coherence tomography in dermatology," *Journal of Dermatological Science*, vol. 40, no. 2, pp. 85–94, 2005.

[79] F. Benboujja, J. A. Garcia, K. Beaudette, M. Strupler, C. J. Hartnick, and C. Boudoux, "Intraoperative imaging of pediatric vocal fold lesions using optical coherence tomography," *Journal of Biomedical Optics*, vol. 21, no. 1, p. 016007, 2016.

[80] L. V. Wang and H.-i. Wu, *Biomedical optics: principles and imaging.* John Wiley & Sons, 2012.

[81] B. C. Wilson and G. Adam, "A Monte Carlo model for the absorption and flux distributions of light in tissue," *Medical Physics*, vol. 10, no. 6, pp. 824–830, 1983.

[82] S. T. Flock, M. S. Patterson, B. C. Wilson, and D. R. Wyman, "Monte Carlo modeling of light propagation in highly scattering tissues. I. Model predictions and comparison with diffusion theory," *IEEE Transactions on Biomedical Engineering*, vol. 36, no. 12, pp. 1162–1168, 1989.

[83] L. Wang, S. L. Jacques, and L. Zheng, "MCML—Monte Carlo modeling of light transport in multi-layered tissues," *Computer Methods and Programs in Biomedicine*, vol. 47, no. 2, pp. 131–146, 1995.

[84] G. Yao and L. V. Wang, "Monte Carlo simulation of an optical coherence tomography signal in homogeneous turbid media," *Physics in Medicine & Biology*, vol. 44, no. 9, p. 2307, 1999.

[85] D. A. Boas, J. P. Culver, J. J. Stott, and A. K. Dunn, "Three dimensional Monte Carlo code for photon migration through complex heterogeneous media including the adult human head," *Optics Express*, vol. 10, no. 3, pp. 159–170, 2002.

[86] C. Zhu and Q. Liu, "Review of Monte Carlo modeling of light transport in tissues," *Journal of Biomedical Optics*, vol. 18, no. 5, pp. 050 902–050 902, 2013.

[87] S. Jacques, T. Li, and S. Prahl, "mcxyz. c, a 3D Monte Carlo simulation of heterogeneous tissues," *omlc.*, 2013.

[88] D. Marti, R. N. Aasbjerg, P. E. Andersen, and A. K. Hansen, "MCmatlab: an open-source, user-friendly, MATLAB-integrated three-dimensional Monte Carlo light transport solver with heat diffusion and tissue damage," *Journal of Biomedical Optics*, vol. 23, no. 12, pp. 121 622–121 622, 2018.

[89] H. Shen and G. Wang, "A tetrahedron-based inhomogeneous Monte Carlo optical simulator," *Physics in Medicine & Biology*, vol. 55, no. 4, p. 947, 2010.

[90] Q. Fang, "Mesh-based Monte Carlo method using fast ray-tracing in Plücker coordinates," *Biomedical Optics Express*, vol. 1, no. 1, pp. 165–175, 2010.

[91] E. Alerstam, T. Svensson, and S. Andersson-Engels, "Parallel computing with graphics processing units for high-speed Monte Carlo simulation of photon migration," *Journal of Biomedical Optics*, vol. 13, no. 6, pp. 060 504–060 504, 2008.

[92] Q. Fang and D. A. Boas, "Monte Carlo simulation of photon migration in 3D turbid media accelerated by graphics processing units," *Optics Express*, vol. 17, no. 22, pp. 20 178–20 190, 2009.

[93] Y. Pan, R. Birngruber, J. Rosperich, and R. Engelhardt, "Low-coherence optical tomography in turbid tissue: theoretical analysis," *Applied Optics*, vol. 34, no. 28, pp. 6564–6574, 1995.

[94] D. J. Smithies, T. Lindmo, Z. Chen, J. S. Nelson, and T. E. Milner, "Signal attenuation and localization in optical coherence tomography studied by Monte Carlo simulation," *Physics in Medicine & Biology*, vol. 43, no. 10, p. 3025, 1998.

[95] A. Tycho, T. M. Jørgensen, H. T. Yura, and P. E. Andersen, "Derivation of a Monte Carlo method for modeling heterodyne detection in optical coherence tomography systems," *Applied Optics*, vol. 41, no. 31, pp. 6676–6691, 2002.

[96] Q. Lu, X. Gan, M. Gu, and Q. Luo, "Monte Carlo modeling of optical coherence tomography imaging through turbid media," *Applied Optics*, vol. 43, no. 8, pp. 1628–1637, 2004.

[97] G. Xiong, P. Xue, J. Wu, Q. Miao, R. Wang, and L. Ji, "Particle-fixed Monte Carlo model for optical coherence tomography," *Optics Express*, vol. 13, no. 6, pp. 2182–2195, 2005.

[98] I. T. Lima, A. Kalra, H. E. Hernández-Figueroa, and S. S. Sherif, "Fast calculation of multipath diffusive reflectance in optical coherence tomography," *Biomed. Opt. Express*, vol. 3, no. 4, pp. 692–700, 2012.

[99] M. Kirillin, I. Meglinski, V. Kuzmin, E. Sergeeva, and R. Myllylä, "Simulation of optical coherence tomography images by Monte Carlo modeling based on polarization vector approach," *Optics Express*, vol. 18, no. 21, pp. 21 714–21 724, 2010.

[100] J. Mao, Y. Ling, P. Xue, and Y. Su, "Monte carlo-based full-wavelength simulator of fourier-domain optical coherence tomography," *Biomed. Opt. Express*, vol. 13, no. 12, pp. 6317–6334, 2022.

[101] V. Periyasamy and M. Pramanik, "Importance sampling-based Monte Carlo simulation of time-domain optical coherence tomography with embedded objects," *Applied Optics*, vol. 55, no. 11, pp. 2921–2929, 2016.

[102] S. Malektaji, I. T. Lima Jr, S. S. Sherif *et al.*, "Massively parallel simulator of optical coherence tomography of inhomogeneous turbid media," *Computer Methods and Programs in Biomedicine*, vol. 150, pp. 97–105, 2017.

[103] J. Mao, Y. Ling, P. Xue, and Y. Su, "Importance sampling-accelerated simulation of full-spectrum backscattered diffuse reflectance," *Biomed. Opt. Express*, vol. 14, no. 9, pp. 4644–4659, 2023.

[104] Y. Wang and L. Bai, "Accurate Monte Carlo simulation of frequency-domain optical coherence tomography," *International Journal for Numerical Methods in Biomedical Engineering*, vol. 35, no. 4, p. e3177, 2019.

[105] A. E. Hartinger, A. S. Nam, I. Chico-Calero, and B. J. Vakoc, "Monte Carlo modeling of angiographic optical coherence tomography," *Biomedical Optics Express*, vol. 5, no. 12, pp. 4338–4349, 2014.

[106] N. Mavaddat, S. Ahderom, V. Tiporlini, and K. Alameh, "Simulation of biomedical signals and images using Monte Carlo methods for training of deep learning networks," in *Deep Learning Techniques for Biomedical and Health Informatics*. Elsevier, 2020, pp. 213–236.

[107] S. Guo and J. U. Kang, "Convolutional neural network-based common-path optical coherence tomography A-scan boundary-tracking training and validation using a parallel Monte Carlo synthetic dataset," *Optics Express*, vol. 30, no. 14, pp. 25 876–25 890, 2022.

[108] I. T. Lima, A. Kalra, and S. S. Sherif, "Improved importance sampling for Monte Carlo simulation of time-domain optical coherence tomography," *Biomed. Opt. Express*, vol. 2, no. 5, pp. 1069–1081, 2011.

[109] L. G. Henyey and J. L. Greenstein, "Diffuse radiation in the galaxy," *Astrophysical Journal*, vol. 93, pp. 70–83, 1941.

[110] T. Binzoni, T. S. Leung, A. H. Gandjbakhche, D. Ruefenacht, and D. Delpy, "The use of the Henyey–Greenstein phase function in Monte Carlo simulations in biomedical optics," *Physics in Medicine & Biology*, vol. 51, no. 17, p. N313, 2006.

[111] S. L. Jacques, "Optical properties of biological tissues: a review," *Physics in Medicine & Biology*, vol. 58, no. 11, p. R37, 2013.

[112] B. H. Hokr, J. N. Bixler, G. Elpers, B. Zollars, R. J. Thomas, V. V. Yakovlev, and M. O. Scully, "Modeling focusing Gaussian beams in a turbid medium with Monte Carlo simulations," *Optics Express*, vol. 23, no. 7, pp. 8699–8705, 2015.

[113] F. Schneider, J. Draheim, R. Kamberger, and U. Wallrabe, "Process and material properties of polydimethylsiloxane (PDMS) for Optical MEMS," *Sensors and Actuators A: Physical*, vol. 151, no. 2, pp. 95–99, 2009.

[114] S. A. Prahl, M. J. van Gemert, and A. J. Welch, "Determining the optical properties of turbid media by using the adding–doubling method," *Applied Optics*, vol. 32, no. 4, pp. 559–568, 1993.

[115] R. B. Saager, C. Kondru, K. Au, K. Sry, F. Ayers, and A. J. Durkin, "Multilayer silicone phantoms for the evaluation of quantitative optical techniques in skin imaging," in *Design and Performance Validation of Phantoms Used in Conjunction with Optical Measurement of Tissue II*, vol. 7567. SPIE, 2010, pp. 40–47.

[116] J. Schmitt, A. Knüttel, and R. Bonner, "Measurement of optical properties of biological tissues by low-coherence reflectometry," *Applied optics*, vol. 32, no. 30, pp. 6032–6042, 1993.

[117] F. J. van der Meer, D. J. Faber, D. M. B. Sassoon, M. C. Aalders, G. Pasterkamp, and T. G. van Leeuwen, "Localized measurement of optical attenuation coefficients of atherosclerotic plaque constituents by quantitative optical coherence tomography," *IEEE transactions on medical imaging*, vol. 24, no. 10, pp. 1369–1376, 2005.

[118] M. Almasian, N. Bosschaart, T. G. van Leeuwen, and D. J. Faber, "Validation of quantitative attenuation and backscattering coefficient measurements by optical coherence tomography in the concentration-dependent and multiple scattering regime," *Journal of Biomedical Optics*, vol. 20, no. 12, pp. 121 314–121 314, 2015.

[119] A. N. Bashkatov, E. A. Genina, and V. V. Tuchin, "Optical properties of skin, subcutaneous, and muscle tissues: a review," *Journal of Innovative Optical Health Sciences*, vol. 4, no. 01, pp. 9–38, 2011.

[120] I. Krasnikov, A. Seteikin, and B. Roth, "Advances in the simulation of light–tissue interactions in biomedical engineering," *Biomedical Engineering Letters*, vol. 9, pp. 327–337, 2019.

[121] Q. Lu, X. Gan, M. Gu, and Q. Luo, "Monte carlo modeling of optical coherence tomography imaging through turbid media," *Appl. Opt.*, vol. 43, no. 8, pp. 1628–1637, 2004.

[122] J. Shin, B. T. Bosworth, and M. A. Foster, "Single-pixel imaging using compressed sensing and wavelength-dependent scattering," *Opt. Lett.*, vol. 41, no. 5, pp. 886–889, 2016.

[123] M. Y. Kirillin, G. Farhat, E. A. Sergeeva, M. C. Kolios, and A. Vitkin, "Speckle statistics in oct images: Monte carlo simulations and experimental studies," *Opt. Lett.*, vol. 39, no. 12, pp. 3472–3475, 2014.

[124] V. V. Tuchin, "Tissue optics and photonics: light-tissue interaction," *Journal of Biomedical Photonics & Engineering*, vol. 1, no. 2, pp. 98–134, 2015.

[125] C. Photiou, E. Bousi, I. Zouvani, and C. Pitris, "Using speckle to measure tissue dispersion in optical coherence tomography," *Biomed. Opt. Express*, vol. 8, no. 5, pp. 2528–2535, 2017.

[126] M. Rinehart, Y. Zhu, and A. Wax, "Quantitative phase spectroscopy," *Biomed. Opt. Express*, vol. 3, no. 5, pp. 958–965, 2012.

[127] Y. Ling, Y. Gan, X. Yao, and C. P. Hendon, "Phase-noise analysis of swept-source optical coherence tomography systems," *Opt. Lett.*, vol. 42, no. 7, pp. 1333–1336, 2017.

[128] M. P. de Sivry-Houle, S. B. Beaudoin, S. Brais-Brunet, M. Dehaes, N. Godbout, and C. Boudoux, "All-fiber few-mode optical coherence tomography using a modally-specific photonic lantern," *Biomed. Opt. Express*, vol. 12, no. 9, pp. 5704–5719, 2021.

[129] R. Maltais-Tariant, K. Erde, U. Kanniyappan, C. Boudoux, and M. Dehaes, "An open-source platform for optical coherence tomography Monte Carlo simulation," in *Optical Interactions with Tissue and Cells XXXII*, vol. 11640. SPIE, 2021, p. 116400G.

[130] K. Erdenedalai, R. Maltais-Taraint, M. Dehaes, and C. Boudoux, "Experimentally Validated Monte Carlo Simulator for Fourier-Domain Optical Coherence Tomography," in *Optical Manipulation and Its Applications*. Optica Publishing Group, 2023, pp. JTu4B–29.

[131] J. M. Schmitt, S. H. Xiang, and K. M. Yung, "Speckle in optical coherence tomography," *J. Biomed. Opt.*, vol. 4, no. 1, pp. 95–105, 1999.

[132] B. Karamata, K. Hassler, M. Laubscher, and T. Lasser, "Speckle statistics in optical coherence tomography," *J. Opt. Soc. Am. A*, vol. 22, no. 4, pp. 593–596, 2005.

[133] M. Bashkansky and J. Reintjes, "Statistics and reduction of speckle in optical coherence tomography," *Opt. Lett.*, vol. 25, no. 8, pp. 545–547, 2000.

[134] J. Mertz, *Introduction to Optical Microscopy*, 2nd ed. Cambridge University Press, 2019.

[135] Y. Bromberg, Y. Lahini, E. Small, and Y. Silberberg, "Hanbury Brown and Twiss interferometry with interacting photons," *Nature Photonics*, vol. 4, no. 10, pp. 721–726, 2010.

[136] A. Agrawal, T. J. Pfefer, P. D. Woolliams, P. H. Tomlins, and G. Nehmetallah, "Methods to assess sensitivity of optical coherence tomography systems," *Biomed. Opt. Express*, vol. 8, no. 2, pp. 902–917, 2017.

[137] B. Baumann, C. W. Merkle, R. A. Leitgeb, M. Augustin, A. Wartak, M. Pircher, and C. K. Hitzenberger, "Signal averaging improves signal-to-noise in OCT images: But which approach works best, and when?" *Biomed. Opt. Express*, vol. 10, no. 11, pp. 5755–5775, 2019.

[138] N. Uribe-Patarroyo, A. L. Post, S. Ruiz-Lopera, D. J. Faber, and B. E. Bouma, "Noise and bias in optical coherence tomography intensity signal decorrelation," *OSA Continuum*, vol. 3, no. 4, pp. 709–741, 2020.

[139] R. C. Gonzalez and R. E. Woods, *Digital Image Processing*. Pearson, 2018.

[140] R. Maltais-Tariant, S. Brais-Brunet, M. Dehaes, and C. Boudoux, "Speckle Contrast Reduction through the use of a Modally-Specific Photonic Lantern in Few-Modes Optical Coherence Tomography," in *Biophotonics Congress: Optics in the Life Sciences 2023 (OMA, NTM, BODA, OMP, BRAIN)*. Optica Publishing Group, 2023, p. DM3A.8.

[141] E. Courtie, T. Veenith, A. Logan, A. K. Denniston, and R. J. Blanch, "Retinal blood flow in critical illness and systemic disease: a review," *Annals of Intensive Care*, vol. 10, p. 152, 2020.

[142] L. Nicholson, S. J. Talks, W. Amoaku, K. Talks, and S. Sivaprasad, "Retinal vein occlusion (RVO) guideline: executive summary," *Eye*, vol. 36, pp. 909–912, 2022.

[143] M. S. Rendell, B. K. Milliken, M. F. Finnegan, D. A. Finney, and J. C. Healy, "The Skin Blood Flow Response in Wound Healing," *Microvascular Research*, vol. 53, pp. 222–234, 1997.

[144] C.-P. Liang, J. Wierwille, T. Moreira, G. Schwartzbauer, M. S. Jafri, C.-M. Tang, and Y. Chen, "A forward-imaging needle-type OCT probe for image guided stereotactic procedures," *Optics Express*, vol. 19, pp. 26 283–26 294, 2011.

[145] Y. Li, J. Chen, and Z. Chen, "Advances in Doppler optical coherence tomography and angiography," *Translational Biophotonics*, vol. 1, no. 1-2, p. e201900005, 2019.

[146] A. S. Nam, I. Chico-Calero, and B. J. Vakoc, "Complex differential variance algorithm for optical coherence tomography angiography," *Biomedical Optics Express*, vol. 5, p. 3822, 2014.

[147] B. Braaf, S. Donner, A. S. Nam, B. E. Bouma, and B. J. Vakoc, "Complex differential variance angiography with noise-bias correction for optical coherence tomography of the retina," *Biomedical Optics Express*, p. 486, 2018.

[148] S. Makita, K. Kurokawa, Y.-J. Hong, M. Miura, and Y. Yasuno, "Noise-immune complex correlation for optical coherence angiography based on standard and Jones matrix optical coherence tomography," *Biomedical Optics Express*, vol. 7, pp. 1525–1548, 2016.

[149] A. H. Kashani, C.-L. Chen, J. K. Gahm, F. Zheng, G. M. Richter, P. J. Rosenfeld, Y. Shi, and R. K. Wang, "Optical Coherence Tomography Angiography: A Comprehensive Review of Current Methods and Clinical Applications," *Progress in retinal and eye research*, vol. 60, pp. 66–100, 2017.

[150] L. Huang, Y. Fu, R. Chen, S. Yang, H. Qiu, X. Wu, S. Zhao, Y. Gu, and P. Li, "SNR-Adaptive OCT Angiography Enabled by Statistical Characterization of Intensity and Decorrelation With Multi-Variate Time Series Model," *IEEE Transactions on Medical Imaging*, vol. 38, 2019.

[151] K. Kurokawa, S. Makita, Y.-J. Hong, and Y. Yasuno, "In-plane and out-of-plane tissue micro-displacement measurement by correlation coefficients of optical coherence tomography," *Optics Letters*, vol. 40, pp. 2153–2156, 2015.

[152] K. Cheishvili and J. Kalkman, "Sub-diffusion flow velocimetry with number fluctuation optical coherence tomography," *Optics Express*, vol. 31, pp. 3755–3773, 2023.

[153] K. Kurokawa, S. Makita, Y.-J. Hong, and Y. Yasuno, "Two-dimensional micro-displacement measurement for laser coagulation using optical coherence tomography," *Biomedical Optics Express*, vol. 6, no. 1, pp. 170–190, 2015.

[154] J. Tokayer, Y. Jia, A.-H. Dhalla, and D. Huang, "Blood flow velocity quantification using split-spectrum amplitude-decorrelation angiography with optical coherence tomography," *Biomedical Optics Express*, vol. 4, no. 10, pp. 1909–1924, 2013.

[155] R. Maltais-Tariant, M. Dehaes, and C. Boudoux, "Exact measurement of transverse flow velocity using few-mode optical coherence tomography," in *Optical Coherence Tomography and Coherence Domain Optical Methods in Biomedicine XXVII*, J. A. Izatt and J. G. Fujimoto, Eds., vol. PC12367, International Society for Optics and Photonics. SPIE, 2023, p. PC123670G.

[156] J. W. Goodman, "Statistical Properties of Laser Speckle Patterns," in *Laser Speckle and Related Phenomena*, J. C. Dainty, Ed. Berlin, Heidelberg: Springer, 1975, pp. 9–75.

[157] J. D. Briers and A. F. Fercher, "Retinal blood-flow visualization by means of laser speckle photography." *Investigative Ophthalmology & Visual Science*, vol. 22, pp. 255–259, 1982.

[158] A. F. Fercher and J. D. Briers, "Flow visualization by means of single-exposure speckle photography," *Optics Communications*, vol. 37, pp. 326–330, 1981.

[159] J. Senarathna, A. Rege, N. Li, and N. V. Thakor, "Laser Speckle Contrast Imaging: Theory, Instrumentation and Applications," *IEEE Reviews in Biomedical Engineering*, vol. 6, pp. 99–110, 2013.

[160] D. Marcuse, "Gaussian approximation of the fundamental modes of graded-index fibers," *JOSA*, vol. 68, pp. 103–109, 1978.

[161] C. J. Sheppard, "Scanning confocal microscopy," *Encyclopedia of Optical Engineering*, pp. 2525–2544, 2003.

[162] R. Chen, L. Yao, K. Liu, T. Cao, H. Li, and P. Li, "Improvement of Decorrelation-Based OCT Angiography by an Adaptive Spatial-Temporal Kernel in Monitoring Stimulus-Evoked Hemodynamic Responses," *IEEE Transactions on Medical Imaging*, vol. 39, 2020.

[163] M. G. O. Gräfe, O. Nadiarnykh, and J. F. D. Boer, "Optical coherence tomography velocimetry based on decorrelation estimation of phasor pair ratios (DEPPAIR)," *Biomedical Optics Express*, vol. 10, 2019.

[164] B. J. Vakoc, S. H. Yun, J. F. d. Boer, G. J. Tearney, and B. E. Bouma, "Phase-resolved optical frequency domain imaging," *Optics Express*, vol. 13, pp. 5483–5493, 2005.

[165] M. Guizar-Sicairos, S. T. Thurman, and J. R. Fienup, "Efficient subpixel image registration algorithms," *Optics Letters*, vol. 33, p. 156, 2008.

[166] H. S. Stone, M. T. Orchard, E.-C. Chang, and S. A. Martucci, "A fast direct Fourier-based algorithm for subpixel registration of images," *IEEE Trans. Geoscience and Remote Sensing*, vol. 39, pp. 2235–2243, 2001.

[167] B. Reddy and B. Chatterji, "An FFT-based technique for translation, rotation, and scale-invariant image registration," *IEEE Transactions on Image Processing*, vol. 5, pp. 1266–1271, 1996.

[168] H. Bruus, "Acoustofluidics 1: Governing equations in microfluidics," *Lab on a Chip*, vol. 11, pp. 3742–3751, 2011.

[169] B. Chu, *Laser Light Scattering 2e: Basic Principles and Practice*. Academic Press, 2012.

[170] X. Liu, Y. Huang, and J. U. Kang, "Distortion-free freehand-scanning OCT implemented with real-time scanning speed variance correction," *Optics Express*, vol. 20, pp. 16 567–16 583, 2012.

[171] A. Ahmad, S. G. Adie, E. J. Chaney, U. Sharma, and S. A. Boppart, "Cross-correlation-based image acquisition technique for manually-scanned optical coherence tomography," *Optics Express*, vol. 17, p. 8125, 2009.

[172] M. F. Kraus, B. Potsaid, M. A. Mayer, R. Bock, B. Baumann, J. J. Liu, J. Hornegger, and J. G. Fujimoto, "Motion correction in optical coherence tomography volumes on a per A-scan basis using orthogonal scan patterns," *Biomedical Optics Express*, vol. 3, pp. 1182–1199, 2012.

[173] B. Braaf, K. V. Vienola, C. K. Sheehy, Q. Yang, K. A. Vermeer, P. Tiruveedhula, D. W. Arathorn, A. Roorda, and J. F. de Boer, "Real-time eye motion correction in phase-resolved OCT angiography with tracking SLO," *Biomedical Optics Express*, vol. 4, pp. 51–65, 2012.

APPENDIX A CONTRIBUTIONS

Here are listed the published contributions during the philosophiae doctor (PhD). Oral and poster presentations are not listed.

A.1 Patent

Raphaël Maltais-Tariant, Caroline Boudoux. "Velocity measurement by decorrelation ratio of structured optical signals", patent # WO2024007087A1.

A.2 Peer-reviewed publications

A.2.1 First author

- **Raphaël Maltais-Tariant**, *et al.* "Accurate flow speed measurement through correlation ratios using a mode-selective photonic lantern in optical coherence tomography", *Biomedical Optics Express*, vol. 16, p. 3395-3414, 2025.
- Khaliun Erdenedalai, **Raphaël Maltais-Tariant**, *et al.* "MCOCT: an experimentally and numerically validated, open-source Monte Carlo simulator for optical coherence tomography", *Optica Publishing Group*, vol. 15, p. 624-640, 2024.
- **Raphaël Maltais-Tariant**, *et al.* "Speckle contrast reduction through the use of a modally-specific photonic lantern for optical coherence tomography", *Biomedical Optics Express*, vol. 14, p. 6250-6259, 2023.
- **Raphaël Maltais-Tariant**, *et al.* "Real-time co-localized OCT surveillance of laser therapy using motion corrected speckle decorrelation", *Biomedical Optics Express*, vol. 11, p. 2925-2950, 2020.

A.2.2 Second author

- Simon Brais-Brunet, **Raphaël Maltais-Tariant**, *et al.* "Multifocal optical coherence tomography of the mouse eye to image the vitreoretinal vasculature in full depth", *Journal of Biomedical Optics*, vol. 30, p. 116002-116002, 2025.

- Rodrigo Itzamná Becerra-Deana, **Raphaël Maltais-Tariant**, *et al.* "Three-mode photonic lanterns: comprehensive analysis from theory to experiments", *Optics Continuum*, vol. 4, p. 1198-1211, 2025.
- Yaser Rasouli, **Raphaël Maltais-Tariant**, *et al.* "Performance of biological ion exchange resin and gravity-driven ceramic membrane hybrid process for surface water treatment", *Separation and Purification Technology*, vol. 332, p. 125769, 2024.
- Yaser Rasouli, **Raphaël Maltais-Tariant**, *et al.* "Impact of cleaning on membrane performance during surface water treatment: a hybrid process with biological ion exchange and gravity-driven membranes", *Membranes*, vol. 14, p. 33, 2024.
- Yaser Rasouli, **Raphaël Maltais-Tariant**, *et al.* "Synthesis, characterization, and application of gravity-driven ceramic microfiltration membranes for surface water treatment", *Journal of Water Process Engineering*, vol. 51, p. 103430, 2023.

A.2.3 Yet to be published contributions

- Simon Brais-Brunet, **Raphaël Maltais-Tariant**, *et al.* "In vitro measurement of microscopic flow using a photonic lantern in optical coherence tomography", *Biomedical Optics Express*, Work in progress.
- Rodrigo Itzamná Becerra-Deana, Simon Desrochers, **Raphaël Maltais-Tariant**, *et al.* "Simultaneous plane illumination and detection in confocal microscopy using a mode-selective photonic lantern", *Optics Letters*, Work in progress.
- Rodrigo Itzamná Becerra-Deana, Joseph Lamarre, **Raphaël Maltais-Tariant**, *et al.* "Optical Profile Response to Polarization and Wavelengths Across Photonic Lantern Architectures", *To be determined*, Work in progress.
- Sarah Albos, Rodrigo Itzamná Becerra-Deana, **Raphaël Maltais-Tariant**, *et al.* "Few-Mode Confocal Microscopy with a Mode-Selective Photonic Lantern", *Applied Optics*, Work in progress.

A.3 Presentation

A.3.1 Orals

- **Raphaël Maltais-Tariant**, *et al.* "An open-source platform for optical coherence tomography Monte Carlo simulation", *SPIE Photonics West*, Optical Interactions with Tissue and Cells XXXII, 2021.

- **Raphaël Maltais-Tariant**, *et al.* "Exact measurement of transverse flow velocity and direction using Few-Mode Optical Coherence Tomography", *Gordon Research Seminar*, Optics and Photonics in Medicine and Biology, 2022.
- **Raphaël Maltais-Tariant**, *et al.* "Exact measurement of transverse flow velocity using few-mode optical coherence tomography", *SPIE Photonics West*, Optical Coherence Tomography and Coherence Domain Optical Methods in Biomedicine XXVII, 2023.
- **Raphaël Maltais-Tariant**, *et al.* "Speckle Contrast Reduction through the use of a Modally-Specific Photonic Lantern in Few-Modes Optical Coherence Tomography", *Optica Publishing Group*, Bio-Optics: Design and Application, 2023.

A.3.2 Posters

- **Raphaël Maltais-Tariant**, *et al.* "Exact measurement of transverse flow velocity and direction using Few-Mode Optical Coherence Tomography", *Gordon Research Seminar*, Optics and Photonics in Medicine and Biology, 2022.
- **Raphaël Maltais-Tariant**, *et al.* "Exact measurement of transverse flow velocity and direction using Few-Mode Optical Coherence Tomography", *Gordon Research Conferences*, Optics and Photonics in Medicine and Biology, 2022.